A novel technique for interface reconstruction in transparent media

Vinayak Krishnan

Technische Universiteit Delft

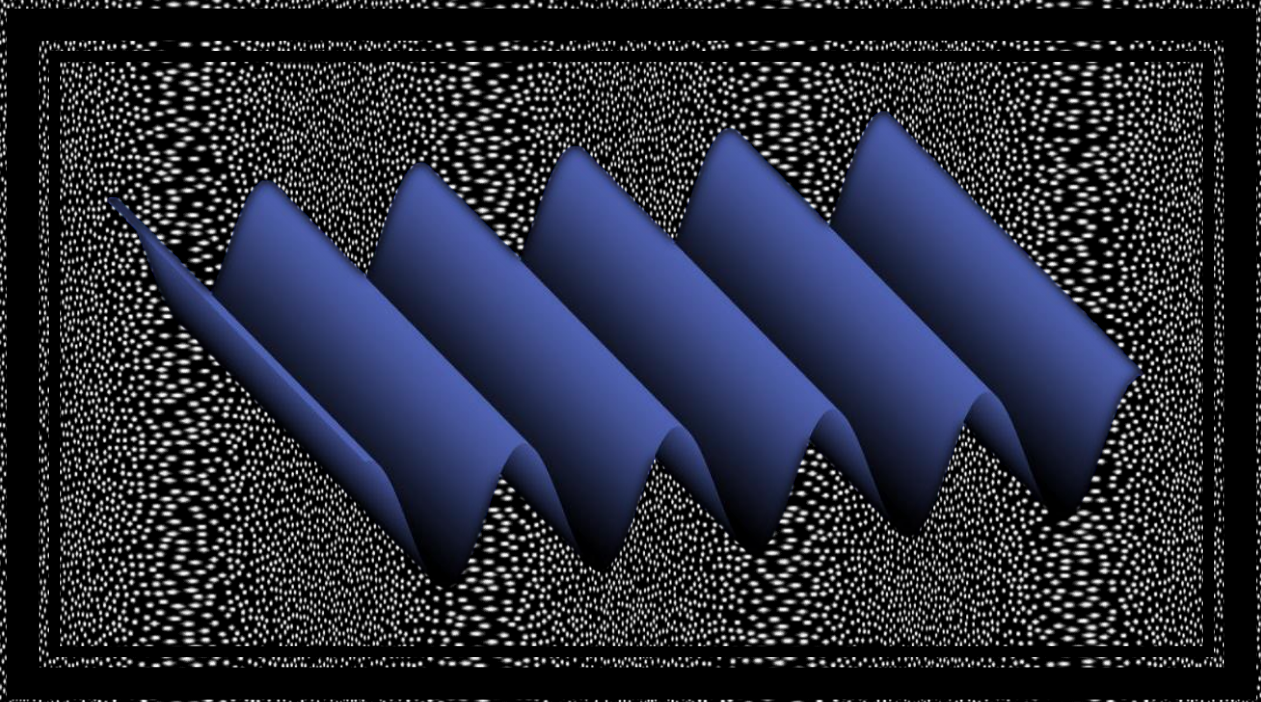

TU Delft Delft University of Technology

Challenge the future

A novel technique for interface reconstruction in transparent media

by

Vinayak Krishnan

in partial fulfillment of the requirements for the degree of

Master of Science

in Mechanical Engineering

at the Delft University of Technology,

to be defended publicly on Monday, November 26, 2018 at 2:00 PM.

Student number: 4517083
P&E report number: 2928

Thesis committee:

Prof. dr. ir. J. Westerweel,	TU Delft, Supervisor
ir. F. T. Charruault,	TU Delft, Daily Supervisor
dr. ir. P. Wellens,	TU Delft

Preface

My Master thesis has been the last phase of my enriching experience at TU Delft. This has been the most challenging and hence the most transformative experience I have ever had. I tried several things out of my comfort zone and failed numerous times, but finally I made it, and this thesis is a proof of it.

I remember the first time I had approached my professor, Jerry Westerweel, for guidance in selecting a thesis topic. I had little background in fluid mechanics and was confused, but he directed me well into selecting this topic. He has a very strong intuitive sense of fluid mechanics and his foresight was very important for me throughout my thesis. In-spite of being super busy, he always made time for arranging regular meetings. Moreover, he was always patient, friendly and very encouraging. I express my gratitude to him for all this.

My daily supervisor, Florian Charruault, has played a very important role in helping me make this work, a 'thesis'. I am grateful to him for that. He was always available whenever I needed any kind of help and tried his best to help me. No matter how much I might have doubted myself or did not achieve something as planned, he always encouraged me and was understanding to any situation. I also thank him for being the main reviewer of my report.

I would like to extend my thanks to the following people: Jasper, for his really expert craftsmanship work and advice to help me build my experimental setup; Edwin Overmars, for helping me with the use of the cameras and setting up of the experiments; Eduardo, for being understanding and sharing the cameras which also he was using parallelly; Aleksandra Gorbatenko, for helping me with the water wave experiments; Prasad, Pranav, Sudarshan and Vigney, for proofreading my report; Caroline, for ensuring all the formal aspects of my thesis were processed smoothly; Peter Wellens, for agreeing to be a part of my graduation committee; Daniel Tam, for his incredible lectures on fluid mechanics, which increased my curiosity and led me to choose this specialization for my Masters; Evert Vixseboxse, for hearing patiently to all my problems and giving psychological and academic advice during my thesis; Department colleagues, professors, fellow students and friends who made this journey really memorable.

At times I felt overwhelmed by the tasks at hand, felt very low or just needed someone to spend quality time with. Constant support from my close friends and family were instrumental for me to keep going during these times. My parents and my sister have always ensured that I get all support I needed to do what I love to do, and so did they during my Masters. A word of thanks is not enough to acknowledge this deed.

"Start before you are ready." -Marie Forleo

"Motivation is what gets you started. Habit is what keeps you going." -Jim Ruyn

"Your story may not have such a happy beginning but that does not make you who you are, it is the rest of it- who you choose to be." — Soothsayer from Kung Fu Panda 2

Vinayak Krishnan
Delft, November 2018

ज्ञानं परमं ध्येयम्

gnyanam paramam dhyeyam - Knowledge is the supreme goal

Nomenclature

Abbreviations

$1D$	One dimension
$2D$	Two dimensions
$3D$	Three dimensions
AC	Alternating current
CAD	Computer aided design
CCD	Charge-coupled device
FOV	Field of view
fps	Frames per second
$FS-SS$	Free surface synthetic Schlieren
$I.D.$	Distance between image plane and lens
IW	Interrogation window
$L.H.S.$	Left hand side
LED	Light-emitting diode
$LIDAR$	Light detection and ranging
LIF	Laser induced fluorescence
$meanX0$	Mean profile which is the mean of all sections parallel to section X0
$meanY0$	Mean profile which is the mean of all sections parallel to section Y0
MRI	Magnetic resonance imaging
$O.D.$	Distance between reference plane and lens
OrX	A unidirectional wave oriented along x axis direction
OrY	A unidirectional wave oriented along y axis direction
PIV	Particle image velocimetry
$SONAR$	Sound navigation and ranging
$Stereo-FS-SS$	Stereo free surface synthetic Schlieren
$Stereo-PIV-SS$	Stereo PIV synthetic Schlieren
UPE	Ultrasound pulsed echography

$X0$	Section taken along the plane x=0
$Y0$	Section taken along the plane y=0

List of symbols

α_1	Right camera angle defined for the Stereo PIV synthetic Schlieren method
α_2	Left camera angle defined for the Stereo PIV synthetic Schlieren method
β_L	Left camera angle defined for the Stereo Free surface synthetic Schlieren method
β_R	Right camera angle defined for the Stereo Free surface synthetic Schlieren method
$\delta\vec{r}$	Displacement of the dot pattern for the Free surface synthetic Schlieren method
$\delta\vec{r}_L$	Displacement of the dot pattern for the left camera respectively for the Stereo free surface synthetic Schlieren method
$\delta\vec{r}_R$	Displacement of the dot pattern for the right camera for the Stereo free surface synthetic Schlieren method
γ	Angle of view of the camera defined for the Stereo Free surface synthetic Schlieren method
μ	Dynamic viscosity of the fluid medium
∇h	Surface gradient of the interface to be measured
ρ	Density of the fluid medium
θ	Interface slope
a	y projection of the light rays
A_{wet}	Surface area of the ship wetted by the fluid medium
b	x projection of the light rays
C_{fD}	Frictional drag coefficient
D	Half length of the Field of view
dx	x projection of the pseudo vector for the Stereo PIV synthetic Schlieren technique
dy	y projection of the pseudo vector for the Stereo PIV synthetic Schlieren technique
dz	z projection of the pseudo vector for the Stereo PIV synthetic Schlieren technique
f	Lens focal length
$f\#$	f-stop number of the camera
F_D	Frictional drag force due to the fluid medium
h	Interface height
h_a	Thickness of air layer between tank and reference plane
h_g	Thickness of glass tank

h_p	Mean interface height
h_{pm}	Modified mean interface height used in the free surface synthetic Schlieren method
i_i	Incidence angle of a light ray refracted at the interface
i_r	Refraction angle of a light ray refracted at the interface
L	Pattern camera distance
L_λ	Width of the wave interface which is function of the wavelength
L_a	Air cavity length
L_c	Characteristic length of the ship
M	Slope of the light ray
n_1	Refractive index of the surrounding medium, mostly air
n_2	Refractive index of the media whose free surface is under study, mostly water
n_g	Refractive index of glass used for the glass tank
px	Position in the field of view, can be in either x or y direction
Q	Air flow rate required to maintain the air cavity
R	Radius of curvature
Re	Reynolds number of the flow
T	Time instant of image capture
V_0	Fluid medium velocity
x	Distance of light ray intersection from the point being observed by the cameras

Abstract

A novel technique for measuring capillary/gravity waves travelling on air/water interfaces is investigated. The main motivation is to measure the free surface deformations of an air cavity used for air lubrication of ship hulls. Due to limitations in the available techniques, two novel methods are proposed, out of which the Stereo Particle Image Velocimetry synthetic Schlieren (Stereo-PIV-SS) technique is found to be more promising. This technique uses the input of random dot pattern images captured with and without an interface by two cameras mounted in a Stereo configuration. These images are processed to generate ”pseudo” particle motion vectors using a Stereo-PIV code. An analytical study is conducted to find a simple linear relation between the pseudo vectors and interface height. Two sets of experiments are conducted to test this technique. One with defined transparent solid Plexiglas and glass profiles and another on small amplitude and slope water waves. For the experiments on water waves, the Free Surface Synthetic Schlieren (FS-SS) technique is used as validation data. In addition to experiments, a synthetic image reconstruction study is conducted to test the quality of the images generated by an in-house code.

The investigation reveals that the Stereo-PIV-SS technique is capable of capturing the flat interface height with sub millimeter precision for all interface heights tested in the range of 5 to 60 mm. Nevertheless, the technique can capture a wave profile with sub millimeter precision only for a limited range of wave parameters. The exact limits can only be defined by understanding more about the interplay of various wave parameters, which include the wave orientation, influencing the reconstruction. However, this technique can capture the profiles of waves having wavelength of the order of 1 cm and amplitude of the order of 1 mm, without requiring information about the mean interface height. Moreover, it is low cost, easy to use and apply since it requires only a standard PIV setting. The first attempt to study this new technique has been promising and it can be applied to specified wave regimes. The method can be developed further by understanding how to remove the effect of wave orientation on the reconstruction and including other wave parameters in the interface height correlation.

List of Figures

Contents

Chapter 1

Introduction

The behaviour of the interface between two immiscible fluids is an age-old problem in fluid mechanics, and is still being studied to understand the various physical phenomena occurring at the interface. There are various mass, momentum, energy and chemical transfers occurring across the interface, that make their behaviour very complex. Especially the waves at a fluid interface are very intricate and dynamic. Because of this, it had always been a challenge to study them for theoreticians, computational experts and experimentalist's alike. Even eminent physicist Richard Feynman acknowledged that and said while talking about waves at the air/water interface, "[water waves] that are easily seen by everyone and which are usually used as an example of waves in elementary courses [...] are the worst possible example [...]; they have all the complications that waves can have [1]." Fluid interfaces are very common and most of the times are seen as a gas/liquid interface, also called a fluid free surface or just free surface. The most common free surface is the air/water interface, which is observed in open water bodies like rivers, oceans etc. Free surfaces are also present in closed liquid tanks and partially liquid filled pipes and channels. Basically, they are present wherever there is an interface between an immiscible gas/liquid pair. Hence, they are studied extensively in many fields, especially multiphase fluid mechanics.

Background

The maritime transport industry is the biggest transport industry accounting for more than 10 billion tons [2] of total goods transported as of 2017. Over 80 % of the world trade is carried out by the shipping industry [2]. Hence, it is a huge energy consumer utilizing almost 10 % [3] of the total world's oil production. Moreover the maritime transport industry accounts for almost 1 billion tons of CO_2 emitted annually which is responsible for 2.5 % of total green house gas emissions by fuel combustion [2]. This is why a constant is effort put in this industry to make the transport as efficient and clean as possible.

Ship propulsion power is used to overcome the various forms of drag forces encountered by a ship and a major contributor to this drag is the friction drag between the ship hull and water. Almost 60 % of the propulsion power is required to overcome this frictional drag [3]. To reduce it, various concepts have been introduced like using special coatings to reduce skin friction and also introducing a new medium of lower viscosity and density as compared to water, between the water and hull. The latter technique can be applied by introducing an air layer between the ship hull and water. This is known as ship drag reduction by air lubrication. A similar concept can be observed in the game of air hockey, where there is an air layer between the puck and the table which allows the puck to glide smoothly with much lower friction. To get an estimate of the drag reduction induced by air lubrication, consider the basic form of the frictional drag force in Eq. 1.1 for any fluid medium in contact with the ship hull. F_D is the frictional drag force on the ship due to the fluid medium surface, ρ is

the density of the fluid medium, A_{wet} is the area of the ship wetted by the fluid medium, C_{fD} is the frictional drag coefficient, V_0 is the fluid medium velocity, μ is the dynamic viscosity of the fluid medium, L_c is the characteristic ship length and Re is the Reynolds number given by $\frac{\rho * V_0 * L_c}{\mu}$.

$$F_D = \frac{1}{2} * \rho * A_{wet} * C_{fD} * V_0^2 \tag{1.1}$$

$$C_{fD} = 0.0592 * Re^{-\frac{1}{5}} \tag{1.2}$$

Using the value of C_{fD} from Eq. 1.2 given in [4], the final form of the friction drag force is as follows:

$$F_D = 0.0296 * A_{wet} * \rho^{\frac{4}{5}} * V_0^{\frac{9}{5}} * \mu^{\frac{1}{5}} * L_c^{-\frac{1}{5}} \tag{1.3}$$

As per the Eq. 1.3, the frictional drag force is mainly dependent on the density, and also to a certain degree on the viscosity of the fluid medium. Hence, changing the fluid around the hull from water to air (water is almost 50 times more viscous and 830 times more dense that air at 20°C), the frictional drag on the ship should reduce. This should help in saving fuel costs. According to studies, it is expected that this technique can help in reducing the fuel consumption of the ship by almost 5 to 20 % [3]. In the thesis study at TU Delft by Oleksandr Zverkhovskyi (2014), the drag reduction achieved in the experiments was 8 to 12 % of the overall drag [5]. Hence, this technique is certainly promising if properly implemented.

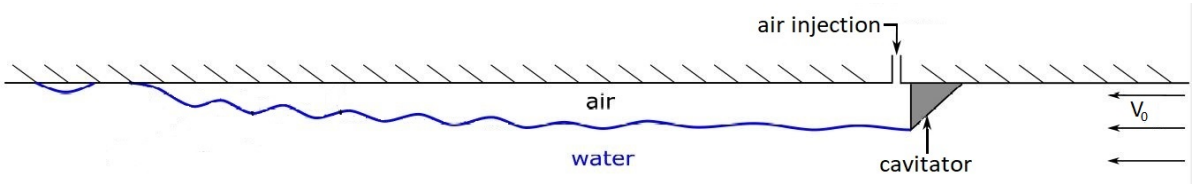

Figure 1.1: Air cavity created beneath a flat plate using a cavitator. Air is injected downstream of the cavitator into a stream of water flowing from right to left at speed V_0. The cavitator creates a pressure difference that helps in air cavity formation. Waves travel along the cavity interface and increase in amplitude when moving towards the cavity closure.

This concept may seem simple, but the proper implementation and understanding of the fluid behavior is a major challenge. The air layer, also called air cavity is maintained below the ship by using an air compressor. The compressor keeps on pumping air to maintain the cavity and replaces air that leaks away from the cavity. Therefore, the efficiency of the system relies heavily on the amount of air being injected to compensate for the air leakages, which makes understanding air cavity behavior very important. Since both liquid and air are in motion and the ship hull is also moving relative to the liquid, there are some interesting fluid phenomena observed at the interface. Fig. 1.1 shows an air cavity developing behind a cavitator in turbulent flow at velocity V_0 (the flow is from right to left). The amplitude of interface waves increase close to the cavity tail or closure. They are intricate 3D waves generated at the interface. A sample picture of the interface is shown in Fig. 1.2.

As already mentioned, the interface can become highly unstable and air can escape from the air cavity closure. Two air leakage mechanisms have been identified at the cavity closure: re-entrant jet and wave pinch off mechanism [3], shown in Fig. 1.3 with labels a and b respectively. The re-entrant jet (Fig. 1.3(a)) is a common mechanism of periodic cavitation shedding in partial cavity studies [6]. In this mechanism, air is shed periodically due to a liquid jet re-entering the cavity through the cavity closure, as shown in Fig. 1.3(a). While for the wave pinch off mechanism, air is lost in pockets due to waves having the same or more amplitude than the cavity thickness and touching the upper plate or hull when reaching the cavity closure (see Fig. 1.3(a)). The air flow rate (Q) required to maintain an air cavity versus the cavity length L_a is shown in Fig. 1.4. It can be seen from the figure that initially

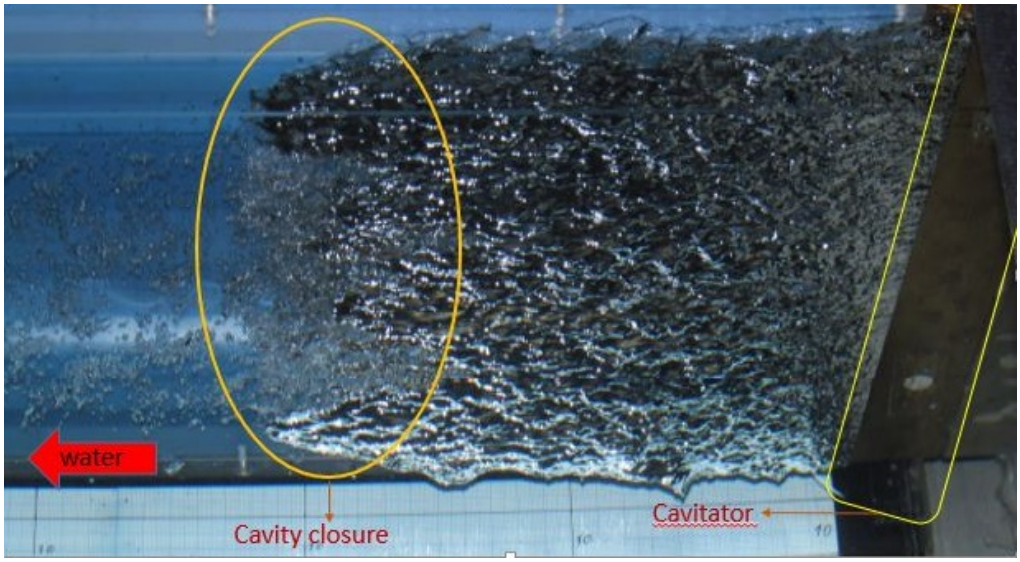

Figure 1.2: Image of an actual air cavity generated below a transparent flat plate using a cavitator [5]. The air cavity is generated inside a cavitation tunnel test section with a transparent flat plate covering the top. Air is injected through a port downstream of the cavitator into the stream of water which flows from right to left. Small 3D wave structures are formed on the air water interface and some air is released from the cavity closure.

a high air flow rate (Q) is required to form the cavity, but later Q reaches a minimum for a stable cavity length. With increasing L_a value, a sharp increase in the air flux requirement is observed as the air cavity becomes unstable. This high air flux is required to feed air lost from the cavity due to the air loss mechanisms. The impact of each air loss mechanism depends on the air cavity closure behaviour as almost all of the air is lost from the closure. The behaviour of the air cavity closure for different flow condiitons is not well understood. Therefore, the wavelength and height of the waves need to be captured accurately in 3D and instantaneously to get a better understanding of the air cavity closure losses. The air cavity closure interface was also proposed to be studied by [3]. Such a study has not yet been published and is of importance in order to make this drag reduction technique successful.

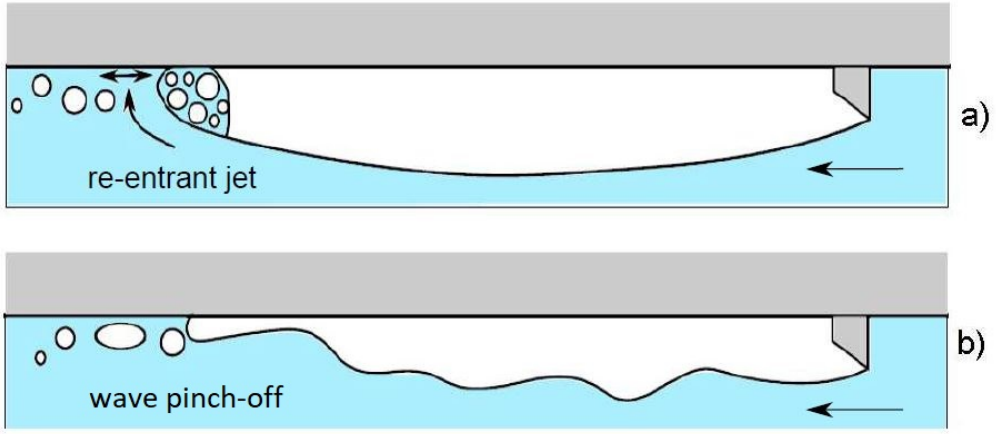

Figure 1.3: Mechanisms for air loss from the cavity closure [5]. Two figures are displayed. Both show an air cavity formed below a test plate/hull as air is injected adjacent to the cavitator. The flow of water is from right to left and there is air loss from the cavity closure. Fig. (a) displays the re-entrant jet air loss mechanism and Fig. (b) displays the wave pinch-off mechanism.

The air cavity interface is dynamic and has intricate wave patterns with steep slopes. Moreover, the structures are highly transient and unstable from the formation itself. This makes it a challenge to capture them accurately. Hence, it is necessary to find a technique suited to accurately study this interface. Apart from the application to air cavity interface recon-

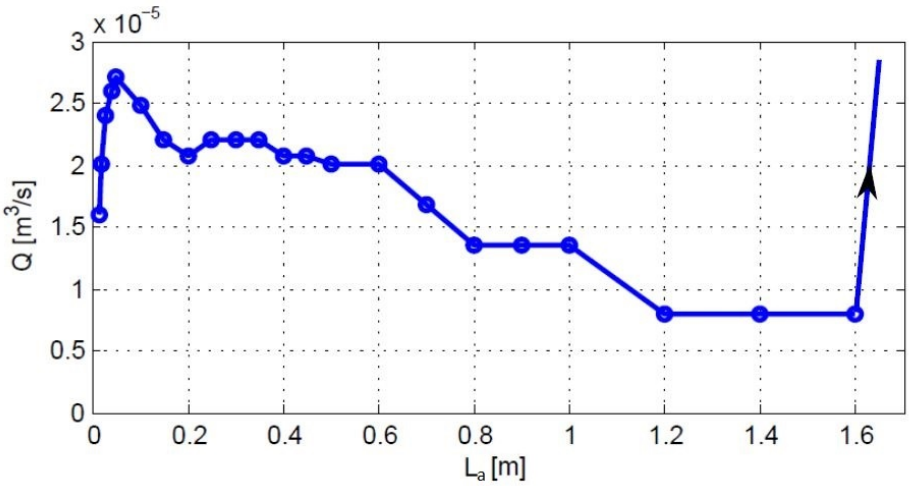

Figure 1.4: Local air flux (Q) required to maintain the air cavity versus air cavity length (L_a) is plotted [5]. Initially a high Q is required for air cavity formation and with time this requirement diminishes as the cavity becomes stable. After a certain L the cavity becomes again unstable and there is a spike seen in Q.

struction, free surface measurement can find application in many other areas where there is a need to measure the interface between two immiscible media. Some examples include the measurement of ship wakes, wave behaviour/sloshing in liquid tanks, falling liquid films, wind generated waves, object/droplet impact on a liquid free surface etc. Moreover, the free surface profiles generated accurately are of interest for validating computational algorithms and also theories to describe such interface wave behaviour. Constant improvements are made everyday in the area of free surface experimental measurement to develop more accurate, fast and easier to apply techniques. This brings us to the problem statement that is the soul of this thesis.

“To develop a novel experimental technique for measuring the fluid interface of an air cavity”

Chapter 2

Research Goals Formulation and Methodology

The problem statement formulated in Chapter 1 pointed at the need to find an experimental free surface measurement technique specifically applicable to reconstruct an air cavity interface. The research field of fluid free surface measurement is very big and also the constraints for an air cavity interface measurement are very specific. Hence, a comprehensive literature review is conducted, and the important findings are mentioned in this chapter. Based on the literature review the research goals are formulated, and the methodology to achieve these goals are listed.

2.1 Literature review on available fluid free surface measurement techniques

There have been various attempts to measure the free surface profile for specific applications over the past years. To get a basic idea and foundation for the various techniques that are already successfully implemented, a literature review is conducted.

2.1.1 Basic Classification

The techniques can be classified into two major groups: intrusive and non-intrusive. The use of intrusive techniques is not very common for fluid free surface measurement, mainly because they disturb the interface profile and most of these techniques can only measure in 1D. Nonetheless, some techniques have been successfully implemented. These techniques typically involve insertion of a probe into the flow field. Some examples include use of conductivity probes [7] or resistance wire gauges [8] where the voltage measurements from the probes are related to the interface height. Fibre optical sensors have been successfully applied to liquid level measurements [9], which also demonstrates a way to discriminate the refractive index of a liquid. For this technique, the liquid level is correlated to a shift in the sensor spectral response.

Optical techniques are the most common types of non-intrusive free surface measurement. Apart from optical techniques, there have also been attempts to use ultrasound pulsed echography (UPE) as applied in [10], to measure the 2D water-vapor interface shape around a hydrofoil. For this technique, echo signals produced by reflection from the interface are recorded and related to the interface height, which is similar in principle to sound navigation and ranging (SONAR) [11]. Moreover, there is a large area of multiphase flow measurement applied to measure bubble/particle sizes and velocities in flows. For example, magnetic res-

onance imaging (MRI) which uses strong magnetic fields, magnetic field gradients and radio waves [12], X-ray imaging [13] which uses the principle of X-ray beam attenuation when passing through a material and electrical capacitance tomography [14] where the spatial dielectric permittivity distribution is related to spatial concentration of the medium. Adapting some of these techniques could possibly help in free surface measurement. However, none of these techniques are as adept currently as the optical techniques to measure free surface profiles in 3D. In the domain of optical techniques, most of the techniques applied use visible light. Apart from this, fluorescent based imaging techniques that capture the illumination intensity of fluorescent dyes in a fluid illuminated by a light source have been successfully implemented. Here the light intensity is related to the interface height. For example, laser induced fluorescence (LIF) [15] and a fluorescence based imaging technique [16] using ultraviolet light have been successfully applied to capture the wave behaviour of falling liquid films. LIDAR (light detection and ranging), generally used for large scale measurement for example in geology and autonomous vehicles, has also been applied to measure wave flumes [17]. For this technique, the concept is to detect the reflected laser beam from the target surface and use the time delay due to reflection and wavelengths to measure the surface profile.

To constrain the review to well developed techniques applicable to a transparent liquid like water, the techniques using visible light are only further investigated.

2.1.2 Optical techniques using visible light for water free surface measurement

A brief classification of the techniques to measure small water waves using visible light is mentioned in [18]. The basic types are reflection and refraction based techniques. Each of these techniques are described as follows:

1. Reflection: The idea here is to capture the light pattern reflected from a fluid surface. The deformations in the reflected images are analyzed and related to the interface height/slope. One of the first attempts to study the water wave topography using reflections was by [19]. The author studied sun glitter patterns on the sea surface to derive sea surface statistics. One common example of a successfully applied reflection reconstruction technique, is fringe projection profilometry [20]. In this technique, a fringe pattern is projected onto an interface and the pattern image is processed to generate the reconstruction. This technique has been successfully applied to water surface reconstruction in [21] and [22]. Other approaches using light reflection without any pattern projection have also been applied, like in the case of a reflection slope detector mentioned in [23].

2. Refraction: The concept of these techniques is to record the corresponding change in the pattern shape placed below an interface with changes in the interface shape and converting it into interface height. This change in pattern shape is due to refraction at the interface following Snell's law. These are the most commonly applied domain of techniques for water waves. They are preferred over reflection because only a small part of the light is reflected from a water surface, which calls for a very high intensity light source. Moreover, reflection based techniques are more sensitive to higher slopes and the maximum slope that can be measured with reflection is lower than that for refraction [23]. Therefore, refraction based techniques are more favourable for water free surface measurement. A comprehensive literature review of important refraction based techniques are presented as follows:

    - Surface gradient detector: The measurement of free surface slope using refraction based techniques has a long history, and one of the first attempt to measure the 1D surface slope was by [24]. Here, the concept was to relate the brightness of the light entering the camera to the local interface slope. A technique to measure

the 2D free surface gradient was first proposed by [23], see Fig. 2.1. This concept involves using a color coded light source from which light passes through a fresnel lens. This lens directs the light rays from a unique position to a unique direction. If each position on the light source has been provided a unique color, it can be said that the light direction or slope has been encoded with its color. These light rays pass through the interface to a camera located far away from the interface. The distance of the cameras from the mean interface height is large enough to approximate that only vertical light rays reach the camera. This approximation is termed as paraxial approximation. Hence, the slopes of the rays reaching the interface are directly related to the interface slope, given that all light rays travel vertically afterwards. Moreover, since the slope of the rays reaching the interface are encoded by its color, the interface slope can be found from the color pattern seen in the images. These surface gradients can be later integrated to find the surface elevations of the interface. It is to be noted that the slopes computed are independent of surface elevation. Also a calibration procedure needs to be carried out by moving a known interface shape to representative positions in the flow field. This technique is applicable for refraction as well as reflection. The same technique has also been applied successfully by [25].

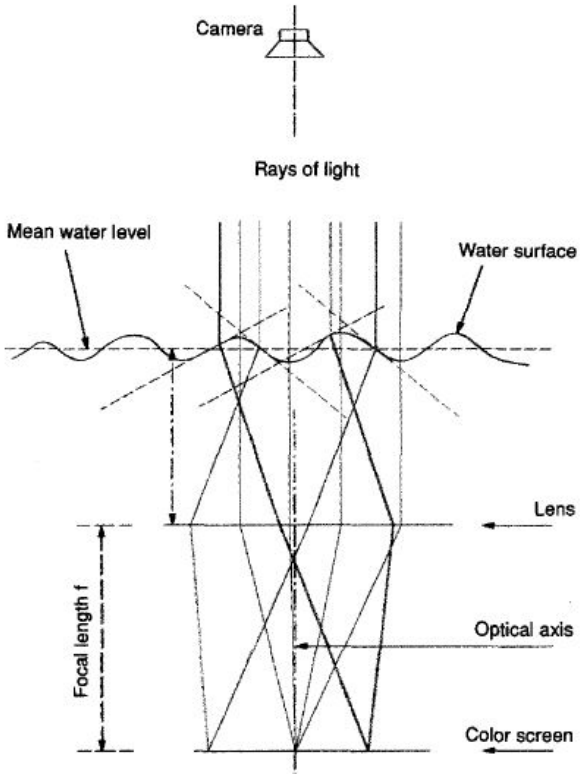

Figure 2.1: Experiment schematic for the Surface gradient detector setup [23]. Colored light rays originate from the color screen and passes through a Fresnel lens which encode the position on the screen to a particular ray direction. The rays pass through an interface to a camera located far above, and hence can be approximated to be vertical after the interface. Thus the interface slope and color of rays can be related, which helps in finding the free surface profile.

- Free Surface Synthetic Schlieren (FS-SS): This concept involves first measuring the displacement generated due to refraction in the images of a random dot pattern placed below an interface. This displacement is later related to the parameter to be measured, for instance surface gradient or density. The technique is also known as, Background oriented schlieren [26] or Synthetic schlieren [27], and has been successfully applied for measurements in flows with density gradients. This idea to use the dot pattern displacement, to measure the wave interface height was first proposed by [28]. It was implemented successfully by [29] with the name, Free

surface synthetic Schlieren. The basic ray diagram for the FS-SS method with the concept is shown in Fig. 2.2. Due to refraction at the wavy interface, there is a displacement of MM" with respect to an image taken without an interface. Similarly, there is also a displacement MM' for the flat mean interface with respect to an image taken without an interface. The difference between the two displacements MM" and MM' is called $\delta\vec{r}$ and it can be directly related to the surface gradient. Later the surface gradient can be integrated to find the surface height profile. The simple linear relation derived in [29] to relate the dot pattern displacement ($\delta\vec{r}$) to the surface gradient (∇h) is shown in Eq. 2.1. This relation is applicable for low interface slopes, low amplitudes and low paraxial angles. Here, h_p is the mean interface height, L is the pattern-camera distance and α is the term $(1 - \frac{n_1}{n_2})$, where n_1 and n_2 are the refractive indices of the two media.

$$\nabla h = -\frac{\delta\vec{r}}{h^*} \quad where \quad \frac{1}{h^*} = \frac{1}{\alpha * h_p} - \frac{1}{L} \tag{2.1}$$

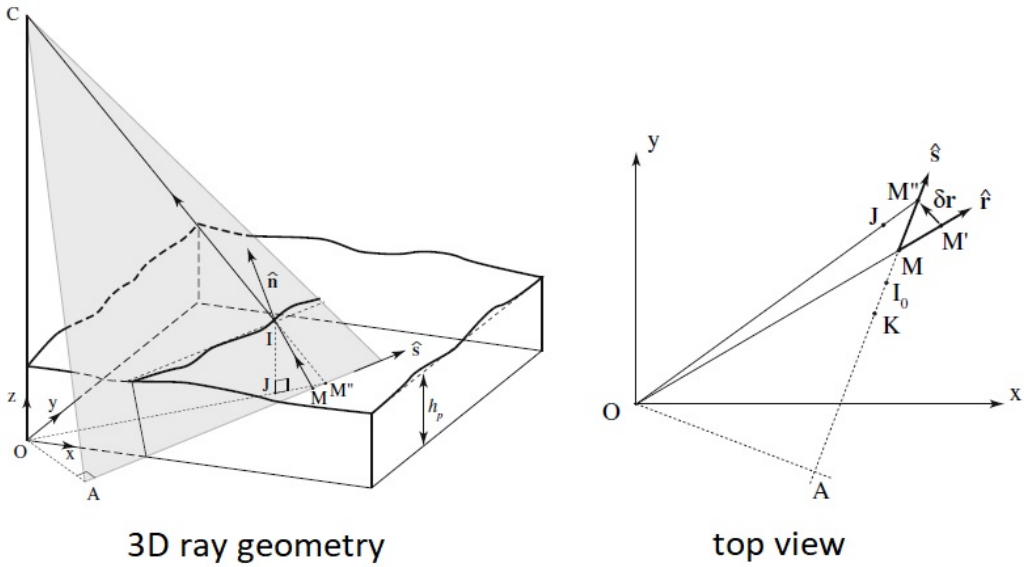

Figure 2.2: 3D ray diagram for a wavy interface with top view for the FS-SS technique [29]. The 3D ray geometry shows rays originating from a point M getting refracted at point I on the interface and reaching the camera C. The mean interface height is h_p. The top view shows the displacement $\delta\vec{r}$ which is the difference in displacement of the point viewed through the wavy interface (MM") with respect the flat interface (MM').

- Stereo Refraction: This technique falls into the class of using a stereo camera configuration to measure free surface profiles. A detailed literature review of the various stereo techniques for free surface measurement is presented in [30]. A successful implementation of the stereo configuration to measure a free surface using refraction was first proposed by [31] and published in [32] with the name, Dynamic refraction stereo. The technique was developed further and successfully applied to measure water wake profiles behind ships by [30], see Fig. 2.3(b). The technique involves using a laser sheet to illuminate the flow seeded with particles and imaging the sheet with two stereo cameras above the interface and one camera below the interface to record a reference image. From this data, the apparent displacements for the two cameras are found for a common point viewed at the interface. The apparent displacements are computed using a classical PIV algorithm, in a manner similar to FS-SS [29], but in this case for two cameras. In Fig. 2.3(b), the common point viewed on the interface is shown as P. An interface height value for point P is assumed, and values of the two normals, one for each camera, are found using

computations. The iterations are continued by changing the interface height until the normal's for the two cameras are equal, which means the height assumed is correct. In this way the interface height profile is found.

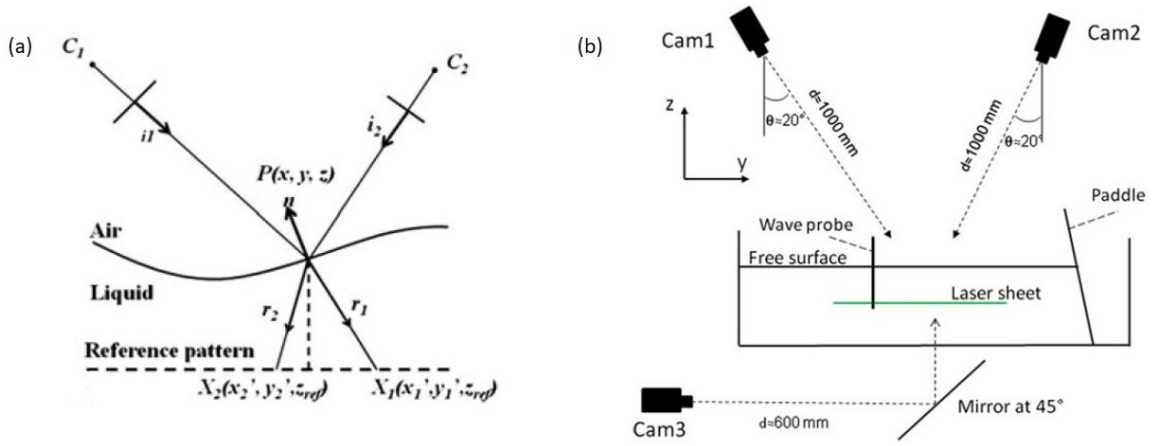

Figure 2.3: Fig. (a) is a 3D ray diagram for the stereo refraction concept [30]. The rays originate from two different points on the laser sheet plane, X_1 and X_2, and pass through the air-liquid interface point P to the two cameras C_1 and C_2. The incident rays are i_1 and i_2, refracted rays are r_1 and r_2 and the normal n which is unique for a fixed point. Fig (b) shows the experimental setup for the stereo refraction concept [30]. A laser sheet illuminates the seeded flow which is captured by two cameras in a stereo configuration, Cam1 and Cam2, above the interface, and one camera Cam3 below the interface. The paddle is used to generate the waves and a wave probe is used for interface height comparison.

2.1.3 Constraints for a technique to be applicable to study an air cavity in the current cavitation tunnel setup

The air cavity studies are planned to be conducted in a cavitation tunnel setup (schematic shown in Fig. 2.4). The cavitation tunnel consists of a closed loop system where water is circulated around the tunnel using an impeller. The air cavity is generated inside the test section shown as number 4 in the schematic. The test section consists of Plexiglas plates around it for optical access. The top cover of the test section consists of a test plate, which can be considered as a primitive model for a ship hull, around which air is supplied in front of a cavitator for air cavity formation. Details of this experimental setup can be found in [5]. An air cavity is a very specific application for free surface measurement and there are also many limits placed by the cavitation tunnel experimental setup. Hence, there are some constraints the new technique proposed must adhere to, for proper implementation. The constraints are as follows:

- It is not possible to capture the image of the mean interface for an air cavity at rest, which is the reference image for the FS-SS technique. Therefore, the reference mean interface height is unknown. This is because an air cavity free surface is always unstable and keeps on fluctuating from the creation of the air cavity itself.
- Since the aim is to measure intricate wave phenomena at the air cavity interface, at least a sub-millimeter precision in the experimental results for both height and wavelength of the interface waves is required.
- The test section for the air cavity is closed for physical access from all sides. This will be an obstruction to apply surface measurement techniques which use insertions of probes or any other equipment into the cavity interface.
- The test section has a cross section of 300 x 300 m^2 at the entrance, with a maximum velocity of 7 m/s in the test section [5]. This means that large quantities of dye and

particles are required if techniques using seeding or pigmentation are employed. Hence, such techniques are avoided because filtering such a large quantity of water is not practical.

- The waves generated at the air cavity free surface are 3D in nature. Hence a 3D reconstruction technique is required.
- The air cavity flow field is highly unsteady. Hence, a technique able to capture such transient behavior accurately is required.
- Free surface measurement in 3D is a complicated field with many of the techniques having tedious experimental procedures and processing. Hence, it will be attempted to keep the technique simple to use and apply.

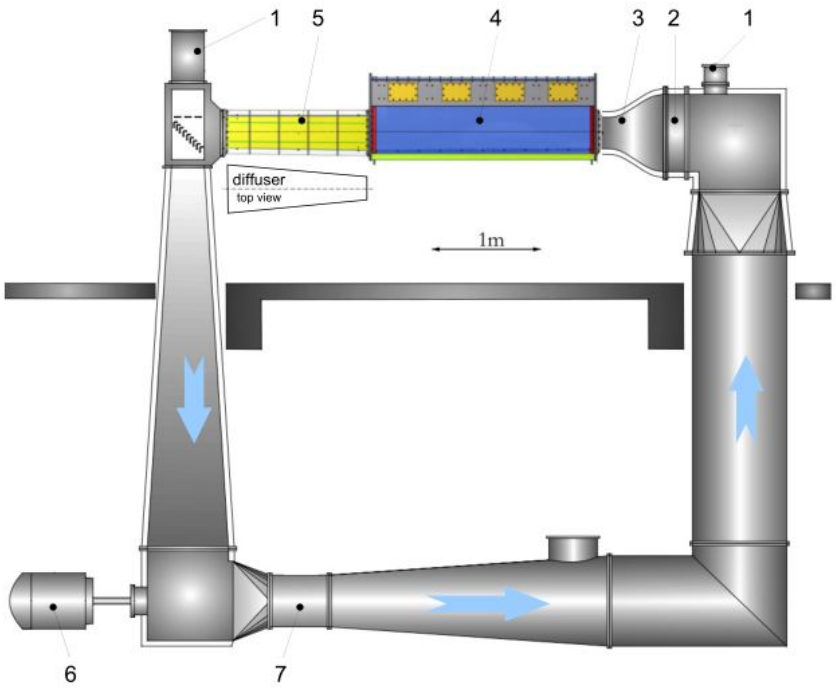

Figure 2.4: Schematic of the cavitation tunnel setup to be used for air cavity studies [5]. The components of the tunnel as marked in the figure are, (1) De-aeration chamber, (2) Honeycomb, (3) contraction part, (4) Test section for air cavity, (5) Diffuser, (6) Electric motor, (7) Location of impeller

2.1.4 Requirement of a new technique

The numerous constraints mentioned in Sec. 2.1.3, limit the applicability of the discussed techniques to an air cavity in the current setup. Out of the visible optical techniques, refraction is more viable for a transparent liquid like water. In the refraction domain, multiple techniques were discussed in the Sec. 2.1.2. The Surface gradient detector and the Stereo refraction techniques require tedious calibration as part of the experimental procedure. Moreover, a 3D calibration target needs to be moved inside the field of view for both the techniques, which is not feasible in the current case as the inside of the test section is not accessible. The FS-SS method looks promising, with very simple procedures and processing, but as already mentioned in Sec. 2.1.3, no reference image of a flat interface can be captured for an air cavity. Therefore, FS-SS is not directly applicable to an air cavity. Moreover, techniques using seeding and pigments are to be avoided as per the constraints mentioned in Sec. 2.1.3. Considering all these limitations and obstacles in the currently available techniques, a new technique suited for measuring the air cavity free surface needs

to be developed. Two novel ideas are proposed in the next section to find an appropriate technique.

2.2 New technique hypothesis

Two novel ideas based on refraction and stereo vision are proposed. Detailed descriptions of the techniques are provided in Chapter 3. A brief description is as follows:

2.2.1 Stereo Free Surface Synthetic Schlieren (Stereo-FS-SS)

As the name already suggests, the idea is to use two cameras and try to adapt the FS-SS technique proposed in [29]. The Eq. 2.1 can be written for two cameras, and it is hypothesized that we can get the surface gradient by solving the equations for the two cameras. Integrating this local surface gradient, the local interface height can be found.

2.2.2 Stereo PIV Synthetic Schlieren (Stereo-PIV-SS)

The idea behind this technique is to combine concepts from Stereo PIV and FS-SS. Considering the displacement of dots due to refraction at the interface as a virtual motion of particles, pseudo vectors for the particle motion can be found out. It is hypothesized that these pseudo vectors have a strong correlation with the interface height and can help in finding the free surface profile.

2.3 Available tools

2.3.1 Ray tracing code

An in-house ray tracing algorithm was used to generate synthetic experimental data which was used for preliminary testing of the proposed techniques. It is also proposed to help in testing various conditions not possible to test with a real experimental setup. This code generates synthetic images as an output of a patterned image seen through a user defined interface. This code had not yet been tested for free surface measurement applications, and hence has to be first validated before use.

2.3.2 Stereo PIV code

This code is based on the concepts of Stereo PIV from [33] and [34]. The code takes two sets of calibration images and two sets of particle/dot pattern images as input to generate a 3D reconstructed velocity vector field. All parts of the code are developed in-house.

2.4 Research Questions

The proposed techniques form the basis of this research work. Based on this, the research questions formulated are as follows:

1. Is it possible to adapt the FS-SS method by using 2 cameras to find the interface height without a mean interface reference image? What are the constraints and limitations for this method?

2. Can the pseudo Stereo PIV vectors generated from Synthetic Schlieren images be related to the interface height? What are the constraints and limitations for this method?

2.5 Methodology

To answer the research questions, the following steps are followed, which also forms the content for the later chapters in the report. A diagrammatic representation of the methodology is shown in Fig. 2.5.

- First a theoretical background of the proposed techniques is presented in Chapter 3. Based on this theory, further steps to study the techniques are decided.
- After this, an analytical study is conducted to analyze the proposed methods by 2D geometric ray tracing. The analytics and CAD models are studied to find a relation for the interface height. It is also aimed to give a basic idea for the behaviour of the various parameters of the technique. This is discussed in Chapter 4.
- After this, a study experiment with Plexiglas and glass interfaces is conducted with simple interface shapes to generate reconstruction data for checking the techniques. The relation found from the analytics is also tested with these study experiments. This study provides a good idea about the sensitivity and limits of the technique and is discussed in detail in Chapter 5.
- The findings from all the studies are applied to conduct free surface measurements on actual water waves using the proposed technique. The results are analyzed and the accuracy and limits of the technique are determined. This is discussed in Chapter 5.
- Later, the ray tracing code is used to generate synthetic images for some defined interface shapes and the output is post processed to generate the reconstruction. The reconstruction generated with synthetic data is compared to that with experiments to check whether the synthetic data can replicate the experimental observations. This is discussed in Appendix B.

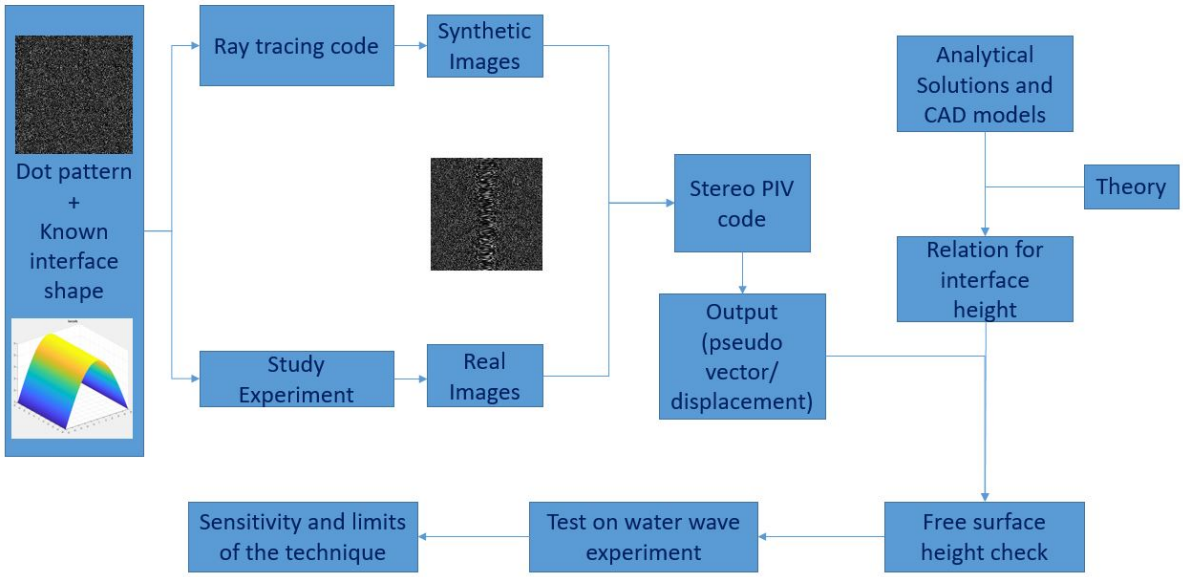

Figure 2.5: Methodology flowchart for achieving the research goals formulated. An analytical study combined with theory helps in finding a relation for the interface height which is applied in the study experiments for validation and tuning. Finally the findings are applied on actual water wave experiments to find the sensitivity and limits of the technique.

Chapter 3

Proposed Free Surface Measurement Techniques

After a comprehensive literature review and listing of constraints, two free surface measurement techniques were proposed in Chapter 2. This chapter explains the concepts behind the proposed techniques in detail.

3.1 Foundation

The two techniques proposed use a stereo camera configuration to capture synthetic Schlieren images. Moreover, both techniques, especially Stereo-PIV-SS, use concepts from particle image velocimetry (PIV). To lay a foundation for the techniques, the main concepts involved are presented as follows.

3.1.1 Synthetic Schlieren imaging

The synthetic Schlieren technique, also introduced in Chapter 2, uses the apparent deformation of a random dot pattern placed behind/below the flow field, to measure the density variations or, as required in our case, the interface profile. The change in the pattern shape when viewed through the interface is due to the refraction at the interface that follows Snell's law. A simple example to get an idea would be the deformation of the river bed pebbles seen from above. The small waves on the river surface seem to deform the pebbles when viewed from above, and this is due to light refraction at the interface. To give a visual representation of synthetic Schlieren imaging used to measure interface profiles, three images are shown in Fig. 3.1. Fig. 3.1(a) is an image of a random dot pattern taken with an undisturbed mean interface. A zoomed in view shows how the random dot pattern actually looks like. Fig. 3.1(b) is an image of the interface that is to be measured. Fig. 3.1(c) is an image of a random dot pattern placed below the interface shown in Fig. 3.1(b). Fig. 3.1(c) shows how the pattern gets stretched when viewed through the wavy interface. This displacement of the dots with respect to the reference image Fig. 3.1(c) can be computed using a standard correlation based PIV algorithm. Finally, this displacement can be related to the interface profile as shown in Eq. 2.1.

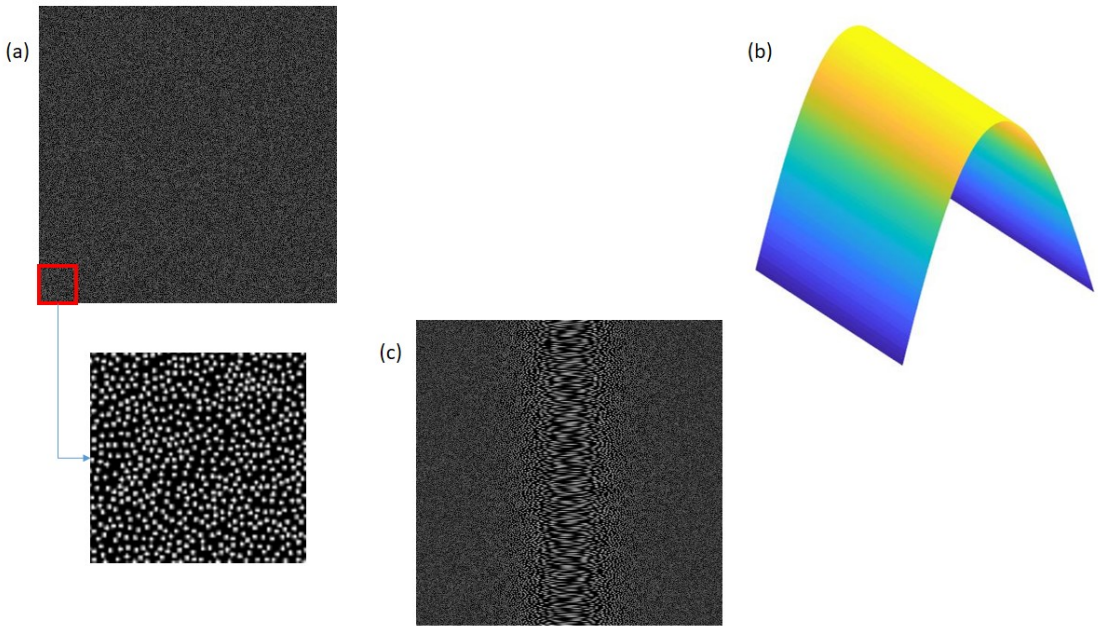

Figure 3.1: A qualitative representation of an apparent deformation of a random dot pattern when imaged through a wavy interface shape. Three images are shown: (a) A random dot pattern imaged with an undisturbed mean interface and a zoomed view shown of the dot pattern, (b) A wave interface, (c) The random dot pattern imaged through the wavy interface. All images are generated with the in-house ray tracing code mentioned in Chapter 2.

3.1.2 Stereo vision and Stereo Particle image velocimetry (PIV)

Stereo vision

To understand Stereo PIV, first it is important to understand stereo vision. A single camera can capture the image of an object only in two dimensions. To get the depth or the 3^{rd} dimension, one smart idea is to use the images of the object captured from two different views. The disparity in the two images can help in getting the third dimension of the object. This method is called triangulation in the field of computer vision, which is the basic concept on which various 3D reconstruction algorithms are based upon. Even human beings are able to perceive their surroundings in 3D because of stereo vision with the two eyes. The human brain is like a computer that processes the two images from the two eyes to create a 3D vision that gives a sense of depth. This generation of depth perception by the brain is called stereopsis. To give an example, one could try viewing the two sets of images shown in the Appendix A, cross-eyed. Due to stereopsis, the brain fuses the two images from different viewpoints to generate a 3D view. This phenomenon is also applied in 3D movies to give a sense of 3D vision to the viewer.

Stereo PIV

The concept of stereo vision has also been successfully applied to a common fluid flow visualization technique named PIV, to reconstruct the third component of the velocity field [35]. PIV is an experimental technique to find the velocity vectors in the flow domain. It involves the use of a light source like a laser sheet which illuminates particles seeded in the flow to generate images at different instants of fluid motion. Later the images are post processed to get the particles displacements and when divided by time between the images captured gives the local velocity vector. More details about the PIV technique are mentioned in [34]. The Stereo PIV technique is used for velocity vector visualization in a 3D space. A schematic of a translation Stereo PIV configuration is shown in Fig. 3.2. For a translation configuration the

camera axis for both the cameras are parallel to each other and they are orthogonal to the object plane. In any case, the basic concept depicted in the Fig. 3.2 stays the same for all camera configurations for Stereo PIV. The schematic shows a particle displacement of Δx and Δz from the object plane location A to a position B. The positions A and B of the particle are at two different time instants. The Camera 1 sees a displacement of $\Delta x_1'$ and the Camera 2 sees a displacement of $\Delta x_2'$ on the object plane, which corresponds to ΔX_1 and ΔX_2 on the image plane respectively. These displacements on the image plane, ΔX_1 and ΔX_2, can be used to find the actual displacements, Δx and Δz, of the particle using the important steps of calibration and post processing, which are discussed in the next paragraph. More theory on Stereo PIV can be found in [35] and [34].

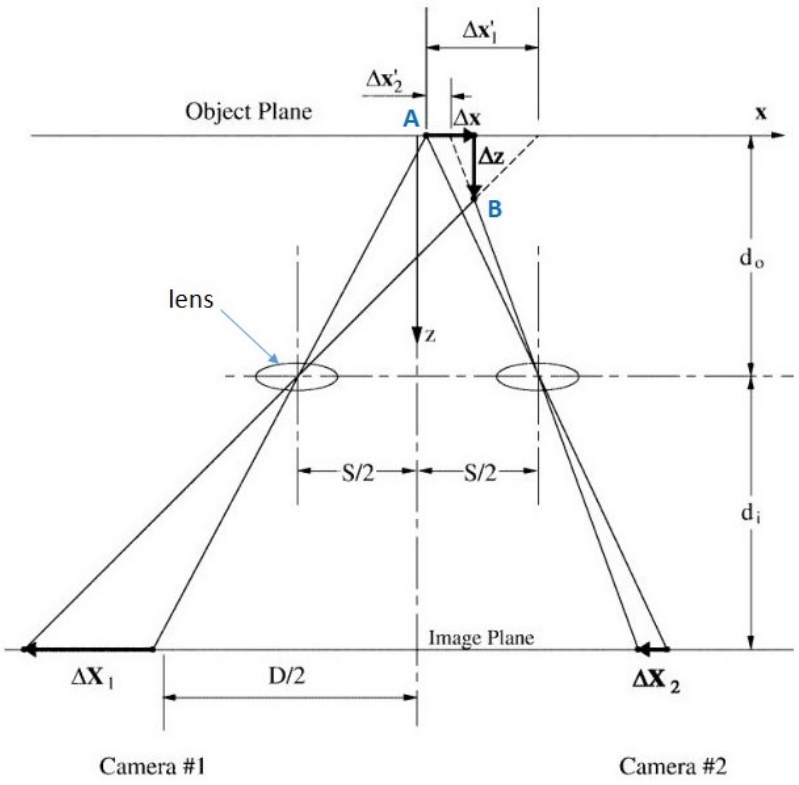

Figure 3.2: Schematic of a stereo camera in a translation configuration [35]. Two cameras, Camera 1 and Camera 2, record the images of the particle motion at two different time instants which correspond to locations A and B. The actual displacements for the particle are Δx and Δz. The displacements seen by Camera 1 and Camera 2 are $\Delta x_1'$ and $\Delta x_2'$ respectively, which correspond to image plane displacements of ΔX_1 and ΔX_2 respectively.

Stereo PIV Calibration and Post processing

A detailed procedure for Stereo PIV calibration, which also takes into account any distortions present in measurements is given in [33]. The experimental calibration procedure involves taking images of a calibration target, which is a regular pattern of markers with known spacing between the markers and size of the markers. The images of this calibration target are captured at two known locations in the field of view, one at the reference plane and one at a plane shifted perpendicular to the reference plane. These two images along with calibration target marker spacing and shift in the calibration target, helps in finding the mapping function ($X = f(x)$) that relates the object plane (x) and the image plane (X) coordinates. After the calibration step, the next step is post processing the particle images to get the actual particle displacements. The flowchart for this process is outlined in Fig. 3.3, which is

referred from [33]. In the Fig. 3.3 the numbers 1 and 2 are assigned to the two different camera orientations. In Step A the raw dot pattern images are processed using a standard PIV displacement field computation algorithm to get the particle displacements in the image plane. The displacements are computed for each interrogation window for a grid defined in the image plane. For details about PIV displacement field computation, refer [34]. In step B, the displacements found in the step A are interpolated onto a grid X_g in the image plane, which is the grid formed by mapping the object plane user defined grid x_g. This step avoids the non-linear inverse problem for solving the object points in terms of image coordinates. Step C is the Calibration procedure that helps in finding the mapping function. Combining these systems for both the cameras, the augmented system as shown in Fig. 3.3 is found. Finally taking the inverse $(\nabla F)_A^+$, the system to convert the image plane displacements in 2D to the real world coordinates in 3D is found out. Dividing these displacements with the time period between image capture gives the 3D velocity vectors for the flow field. For more details on calibration and post processing, refer [33] and [34].

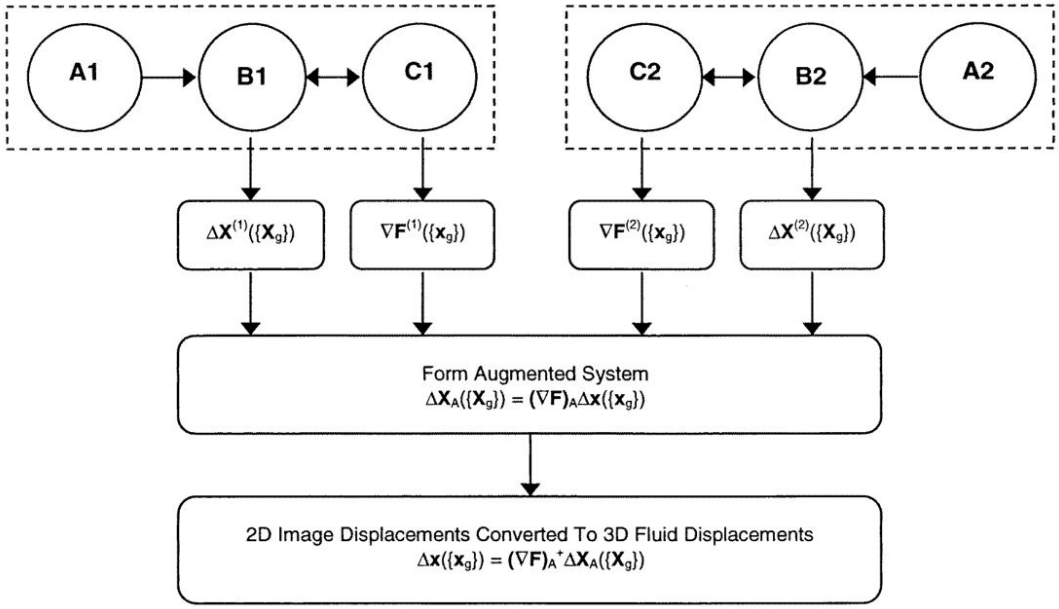

Figure 3.3: Flow chart for Stereo PIV post processing [33]. The numbers 1 and 2 denote the two cameras. A is the displacement field computation step. B is the step where the displacement fields are interpolated onto the mapping (X_g) of the user defined grid x_g. Step C is the calibration step. After these steps, the augmented system is formed and applying the inverse $(\nabla F)_A^+$, the displacement of the particles in the object field (Δx) are found from the image plane displacements (ΔX_A).

3.2 Proposed techniques

3.2.1 Stereo free surface synthetic Schlieren

This technique is an attempt to adapt the FS-SS method to measure the interface profile without using an undisturbed mean interface reference image. Moreover, the use of two cameras in a stereo configuration is proposed. Hence, the equations for the FS-SS method given in [29] needs to be adapted to the current configuration. See Fig. 2.2 and Eq. 3.1 which has been derived in [29].

$$\nabla h = \frac{OM^{"}}{L} - \frac{MM^{"}}{\alpha * h_p} \tag{3.1}$$

Here, an angle γ is introduced, which can be defined as, $\tan\gamma = \frac{OM^{"}}{L}$. This is the angle of

view of the camera. $MM^{"} = \delta\vec{r}$, since a flat interface reference image is not used. Hence, the Eq. 3.1 can be written for both the cameras, where R represents the right camera and L represents the left camera,

$$\nabla h = -\frac{\delta\vec{r_L}}{\alpha * h_p} + \tan\gamma_L \quad \& \quad \nabla h = \frac{\delta\vec{r_R}}{\alpha * h_p} - \tan\gamma_R \tag{3.2}$$

See Fig. 2.2, the right camera can be considered to be located symmetrically opposite to the left camera along the x axis and the sign convention shown in the figure shall govern. The signs for the right camera Eq. 3.2 are reversed as all vectors are in the opposite direction as compared to the left camera. Solving the set of equations in Eq. 3.2, the following expression for the surface gradient (∇h) is found.

$$\nabla h = \frac{\tan\gamma_L * \delta\vec{r_R} - \tan\gamma_R * \delta\vec{r_L}}{\delta\vec{r_L} + \delta\vec{r_R}} \tag{3.3}$$

This is the general expression for the Stereo-FS-SS method. In this equation the values of γ_L and γ_R are not yet defined. Both these angles vary with position. Consider a simple 2D case where the optical axis of both the cameras and all the light rays lie on the same plane. The camera pattern distance is considered to be high as compared to the field of view. Hence, the paraxial approximation is applicable. This means all the rays are parallel to the optical axis of the camera and the same slope as the camera angle. A ray diagram for this case is shown in Fig. 3.4. The ray diagram shows the displacements $\delta\vec{r_R}$ and $\delta\vec{r_L}$ of the object plane dot pattern due to the refraction at the common interface point E at height h for a sloped interface at an angle θ. The displacements are with respect to an image taken without an interface. For this case, the angles γ_L and γ_R are equal to β_L and β_R respectively as per the paraxial approximation. Considering this assumption, the surface gradient could be derived for this orientation from Eq. 3.3.

Even though the idea for the proposed Stereo-FS-SS technique is interesting, there are some open questions that need to be still answered.

- The behavior of Eq. 3.3 for other orientations apart from the one presented in Fig. 3.4 is not defined yet. For other orientations, either the paraxial angles need to be considered or there is a necessity to include a camera angle also in the y direction. If the angles γ_L and γ_R are excluded with the paraxial approximation, then both the equations in Eq. 3.2 become the same and cannot be solved for ∇h.

- For the FS-SS method, the paraxial angle was considered in the derivations, refer Fig. 2.2. The paraxial angle is the angle of approach of the rays to the interface in the vertical camera configuration in FS-SS. However, in the final equations for FS-SS there is no influence of the paraxial angle. But this is not the case with the Stereo-FS-SS technique. As explained in the earlier bullet point, it is not yet clear whether to include the effect of the paraxial angles and how to define the angles γ_L and γ_R.

- The FS-SS method generates the reconstructed profile around the mean interface. Hence, it is necessary to add the mean interface height (h_p) to the reconstructed interface profile found after integration of ∇h to generate the final interface height of the free surface. For the Stereo-FS-SS method, it is not clear as to how to find the final interface height, since there is no h_p defined for addition to the reconstructed profile.

The above observations indicate that the analytics need a more deeper understanding of the optics involved. Hence, further work on this technique is kept outside the scope of this thesis.

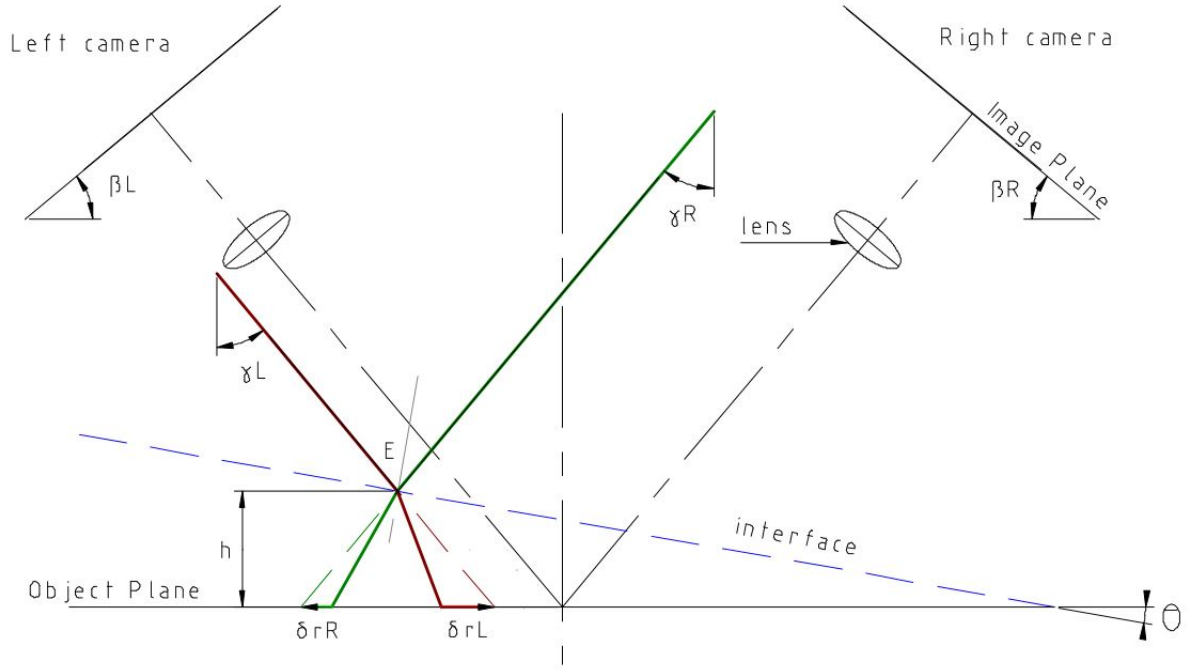

Figure 3.4: Ray diagram for the Stereo-FS-SS method. Two cameras in a Stereo configuration with camera angle of β_L and β_R view a common interface point E at height h from the object plane. All rays from the same camera have the same slope since the paraxial approximation is applicable. Here β_L=γ_L and β_R=γ_R. The refraction at the sloped interface of angle θ generates a displacement of the pattern by $\delta\vec{r_R}$ and $\delta\vec{r_L}$ for the right and the left cameras respectively. These displacements can be finally related to the surface gradient ∇h.

3.2.2 Stereo PIV synthetic Schlieren

This is a refraction based technique and builds on the concepts of Stereo PIV and synthetic Schlieren. Imagine the dots in the random dot pattern used for the synthetic Schlieren technique to be particles. These dots or 'particles' seem to move when placed below an interface, see Fig. 3.1. This movement of dots when seen from two cameras in a Stereo configuration is similar to the particle motion images taken in a typical Stereo PIV experiment, described in Sec. 3.1.2. In Stereo PIV, the flow is seeded with particles which follow the fluid motion and these image plane displacements of particles help in determining the real world particle motion vectors in 3D. But in synthetic Schlieren the dots do not move physically and only appear to move due to a refraction effect at the interface. Hence, this apparent displacement of the dot pattern in a synthetic Schlieren experiment with a Stereo configuration can help in generating virtual particle motion pseudo vectors in the x, y and z directions, which are named here as dx, dy and dz respectively. This concept is shown in the 2D ray diagram in Fig. 3.5. The diagram shows two cameras in a Stereo configuration with the rays originating from a point Q on the object plane and getting refracted at the interface of height h. When these rays are extended without refraction at the interface, they join to form the end point of the pseudo vector. Another set of rays, which are marked in dashed style, are for the images taken of the same point Q without any interface. Δx_L and Δx_R represent the displacement of the pattern for an image taken with an interface with respect to an image taken without an interface for the left and right cameras respectively. The pseudo vector is marked in black with origin at point Q. The projections in the x and z directions are dx and dz respectively. It is hypothesized that the pseudo vector projections (dx, dy and dz in 3D) are strongly related to the interface height. Moreover, there is a possible dependency of the interface height on the orientation of the interface waves. Hence a detailed study to test the validity of this hypothesis is discussed in Chapter 4 and a further detailed experimental study is discussed in Chapter 5.

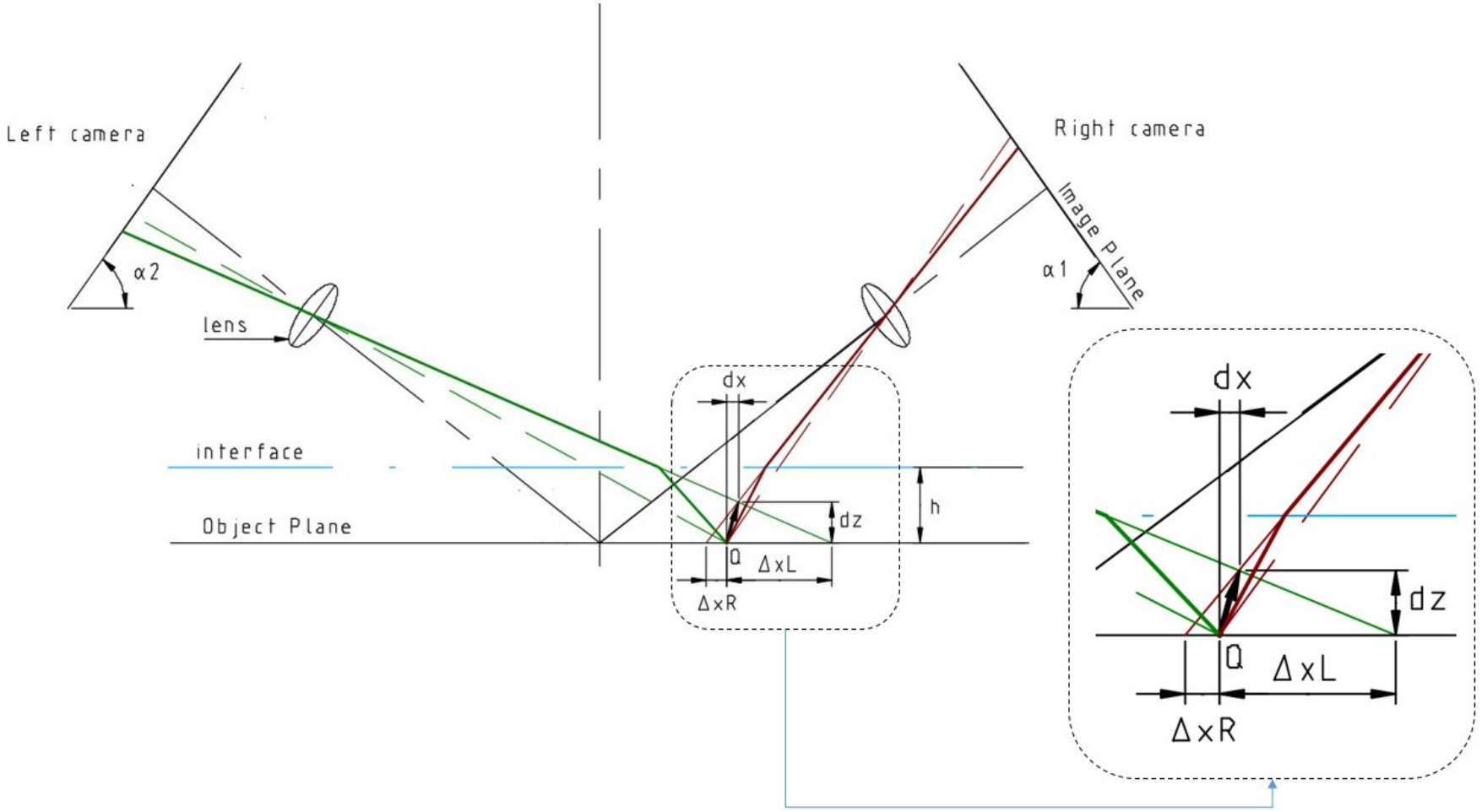

Figure 3.5: Ray diagram for the Stereo-PIV-SS method. Two cameras in a Stereo configuration with camera angles of α_1 and α_2 view a common point Q on the object plane. The rays from Q get refracted at the interface as per Snell's law. The non refracted rays (thinner line) from the two cameras meet to form the end point of the pseudo vector. The pseudo vector is marked in black with origin at point Q. The pseudo vector projections are dx and dz. The dotted line from the two cameras are for the images taken without an interface. Δx_L and Δx_R are the displacements in the dot pattern for the two cameras.

Chapter 4

Analytical Solutions and CAD Models

Chapter 3 provided an introduction to the proposed free surface measurement techniques and it was decided to proceed further with a detailed study of the Stereo-PIV-SS technique. An analytical study is conducted in this chapter to provide a theoretical foundation for the technique and also to understand the behavior of the various parameters involved. The analytics involve solving equations based on 2D geometric ray tracing. Moreover, a CAD modelling task is performed to get a validation of the analytical solutions generated and to get a visual understanding of the technique. Besides laying a basic foundation for the technique, it is also expected that the analytical solutions can help in finding a simplified relation between the interface height and pseudo vectors. Hence, the analytical solutions of the Stereo-PIV-SS technique are studied in detail in this chapter.

4.1 Overview

The analytical study is based on the pin hole camera model. In this model, there are no lenses used to focus the light, and all the light passes through a very tiny (point-like) aperture. The light ray refraction at the interface is governed by the Snell's law. This law defines the relation between the incident ray direction and refracted ray direction, given the refractive indices of the two media. Two approximations are used to simplify the equations, namely the paraxial and the small angle approximations. The paraxial approximation states that all the light rays coming from the camera are parallel. This approximation can be applied in this case as the camera pattern distance is very large. In the experiments mentioned in Chapter 5, the maximum paraxial angle for a vertical camera configuration is 0.0442 ($\approx \frac{2*D}{\sqrt{2}*L}$ [29]) in radians and 2.53^0 in degrees. Since the maximum paraxial angle in radians $\ll 1$, the paraxial approximation is applicable for this case. The small angle approximation states that for all angles less than 10^0, $\sin\theta = \theta$, $\tan\theta = \theta$ and $\cos\theta = 1$, where θ is any random angle. The accuracy for using these approximations is discussed later in this chapter. For legends in all plots presented in the forthcoming sections, par. denotes the results computed using paraxial approximation and par.sm. denotes the results computed using both paraxial and small angle approximations.

The Stereo-PIV-SS technique is applied to two simple cases, one with a flat and another with a sloped interface. For both cases, a symmetric stereo camera configuration is used with the same angles for the left and right cameras ($\alpha_1 = \alpha_2$). First the exact equations for the ray tracing are derived and later the paraxial and small angle approximations are applied to derive more simplified forms of the equations. In each case, the geometry problem is broken down into first finding the coordinates of the ray intersection with a given interface, and later

using them to find the co-ordinates of the pseudo vector, introduced in Chapter 3, Sec.3.2.2. This gives us the values of dz and dx, also introduced in Chapter 3, Sec.3.2.2. By solving further, relations are found between the interface height and the pseudo vectors. All the equations derived were solved in MATLAB R2017a. Moreover, each result was checked with the CAD model prepared in LibreCAD. This is a good validation for the equations derived and the code developed. Hence, all equations presented in the Sec. 4.2 and Sec. 4.3 have been validated first with a CAD model.

4.2 Flat Interface: Derivations and Results

Fig. 4.1 displays the rays travelling from points A and B on the object plane. There are two sets of rays from each point, one for the left and another for the right camera. All rays have been color coded: dark yellow and green for rays travelling to the left camera from the points A and B respectively and dark magenta and red for rays travelling to the right camera from the points A and B respectively. The two sets of rays intersect the flat interface at two different heights, namely h_a and h_b. At the interface, the rays get refracted as per Snell's law and pass through a lens (here approximated as a pin hole) to the camera image plane. All important dimensions and parameters are marked in the Fig. 4.1. The subscript 1 is used for parameters of the right camera and the subscript 2 is used for parameters of the left camera.

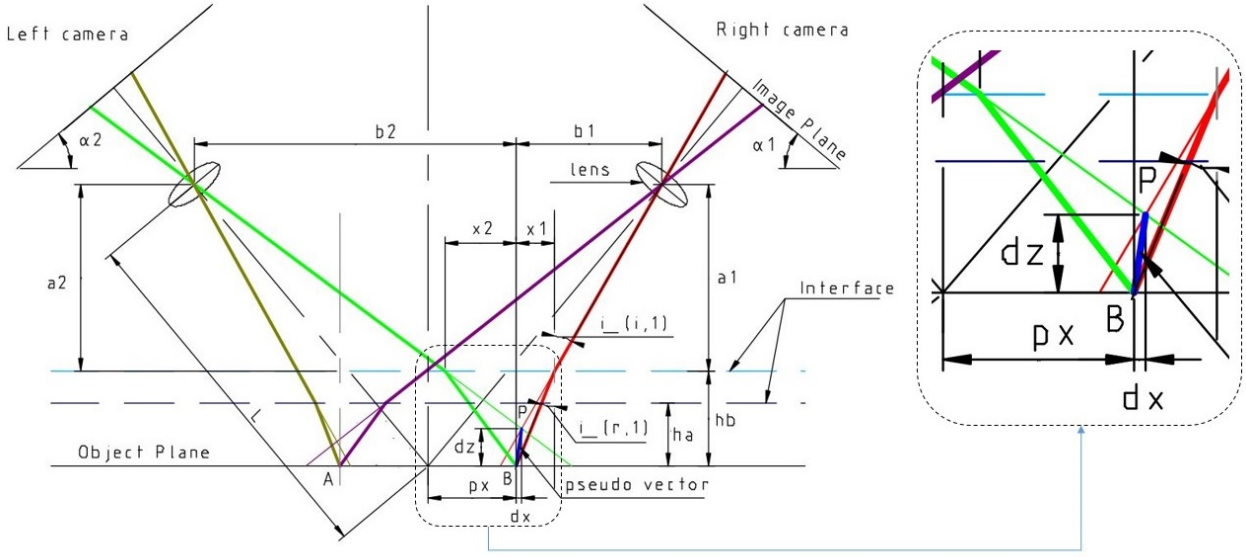

Figure 4.1: CAD model showing ray tracing with application of the Stereo-PIV-SS technique for a flat interface. The diagram shows the rays originating from points A and B reaching the left and right cameras after refraction at two different interface heights (h_a and h_b). The rays from the camera can be extended to find the pseudo vector whose end points for height h_b at location B is marked as P.

4.2.1 Derivation: Flat interface

Exact solutions

The position of the points are known and are at a distance px from the optical axis, as shown in Fig. 4.1. To find the intersection of the light rays on the interface, the following equations are solved. These equations are valid for both the right and the left cameras.

$$tan(i_{i,(1,2)}) = \frac{b_{1,2} - x_{1,2}}{a_{1,2}} \tag{4.1}$$

$$tan(i_{r,(1,2)}) = \frac{x_{1,2}}{h_1} \tag{4.2}$$

Where,

$$\alpha_1 = \alpha_2 = \alpha \; ; \quad b_1 = L * sin(\alpha) - px \; ; \quad b_2 = L * sin(\alpha) + px \; ; \quad a_1 = a_2 = L * cos(\alpha)$$

Applying Snell's law,

$$n_1 * sin(i_i) = n_2 * sin(i_r) \tag{4.3}$$

Where n_1 and n_2 are the refractive indices of the two media separated at the interface. The media below the interface has a refractive index of n_2, with $n_2 > n_1$.

In the Eq. 4.2, Eq. 4.1 and Eq. 4.3, all values except x_1 and x_2 are known for a given camera configuration and interface height. The values of x_1 and x_2 for the right and the left camera respectively are found after iterating and solving the equations. Using these values, the intersection of two imaginary lines from the two cameras assuming no interface being present can be found out. These lines intersect at a point P as shown in Fig. 4.1. The line equations are as follows:

The line equation for the Left camera,

$$x - \frac{y}{M_2} = px - x_2 - \frac{h_b}{M_2} \tag{4.4}$$

where,

$$M_2 = \frac{h_b - L * cos(\alpha)}{L * sin(\alpha) + px - x_2}$$

The line equation for the Right camera,

$$x - \frac{y}{M_1} = px + x_1 - \frac{h_b}{M_1} \tag{4.5}$$

where,

$$M_1 = \frac{L * cos(\alpha) - h_b}{L * sin(\alpha) - px - x_1}$$

Solving Eq. 4.4 and Eq. 4.5 the x and y coordinates of the intersection are found, which are actually the end points of pseudo vector. The y coordinate is named *'dz'*, which is the y projection of the pseudo vector. Subtracting px from the x coordinate, the x projection of the pseudo vector is found. This is named *'dx'*. These projections are shown in Fig. 4.1. The psuedo vector is marked in blue.

Solutions found by applying the paraxial and small angle approximations

For the paraxial case, all the rays going towards the camera are parallel to the camera axis.

Therefore, $i_i = \alpha$ for a flat interface.

Using this value of i_i and applying it to Eq. 4.3, the i_r value is found. Using this i_r and Eq. 4.2, the values for x_1 and x_2 are found, which are the same for both the cameras in this case. This is a simple relation and can be solved without any iterations as opposed to the exact solutions case.

After this, the end point of the pseudo vector is found by solving the same line Eq. 4.4 and Eq. 4.5. The slope values used for solving the line equations are as below.

$$M_1 = tan(\frac{\pi}{2} - \alpha) \;\; and \;\; M_2 = tan(\frac{\pi}{2} + \alpha)$$

The intersection provides the following value for dz,

$$dz = h * \frac{tan(\alpha) - tan(i_r)}{tan(\alpha)} \tag{4.6}$$

This is a simple linear relation between dz and the interface height. The dx value for this case is zero, since both the rays approach the flat interface symmetrically. The small angle approximation is now applied to the Eq. 4.6, to check if it can be further simplified. The i_r value in Eq. 4.6 is found from Eq. 4.3. Using the small angle approximation, Eq. 4.3 can be simplified to,

$$i_r = sin^{-1}(k * \alpha) \;\; ; \; where \; k = \frac{n_1}{n_2}$$

This equation can be further simplified by applying the taylor expansion for $\sin^{-1}(x)$.

$$i_r = k * \alpha + \frac{1}{2} * \frac{(k * \alpha)^3}{3} + ...H.O.T.$$

Here, the maximum value of α is 0.1745 rad (10^0). The maximum value of the refractive index ratio k is 1.5 for a glass water interface, and is generally lower than 1. So the maximum value of α*k is 0.2617. Hence, all the higher order terms apart from the linear term can be neglected.

Therefore the i_2 value simplifies to,

$$i_r = k * \alpha \tag{4.7}$$

Using Eq. 4.7, Eq. 4.6 and the small angle approximation, it can be deduced that,

$$dz = (1 - k) * h \tag{4.8}$$

The Eq. 4.8 shows that it is possible to compute dz by a simple linear relation between the refractive index ratio and interface height for a flat interface. Moreover, this relation for dz is independent of the camera angle. This relation is valid for small angles and for a high camera pattern distance. An idea to use either Eq. 4.6 (for better accuracy) or Eq. 4.8 to find the interface height of a flat interface like a level indicator could be further investigated, but is outside the scope of this thesis.

4.2.2 Results: Flat interface

The equations derived in Sec. 4.2.1 are used to make the plots of dz and dx versus the position on the object plane and the height of the interface. This gives a good idea of the behaviour of the pseudo vectors for a flat interface. The position in the graphs is defined on the object plane with a value of px=0 assigned for the optical axis. The ray tracing diagram for the flat interface is shown in Fig. 4.1. The input parameters for the computations are taken as per the experimental setup described in Chapter 5. Hence, all parameter behaviours are studied considering the limiting values as per the experiments. The input parameters used for the flat interface computations, with air as medium 1 and Plexiglas as medium2, are as follows:

$$h = 20 \; mm; \;\; L = 1600 \; mm; \;\; \alpha = 10^0; \;\; k = \frac{n_1}{n_2} = \frac{1}{1.49}; \;\; Field \; of \; view = 100 \; mm;$$

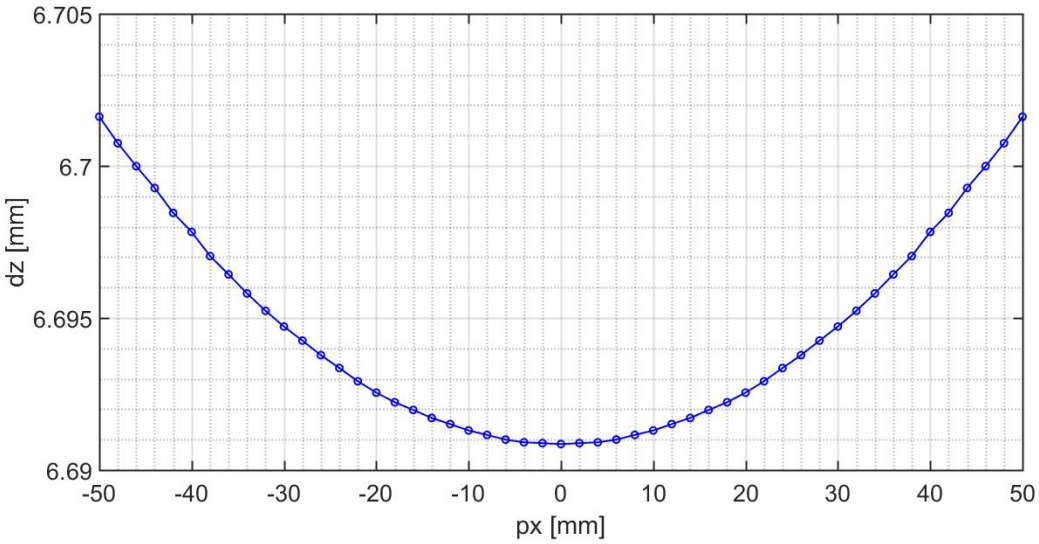

Figure 4.2: Graph of dz vs position on the object plane for a flat interface, solved using exact equations. The behavior is parabolic in nature about the optical axis.

Fig. 4.2 and Fig. 4.3 show the exact solution plot for dz and dx vs the position on the object plane respectively. Fig. 4.2 shows a parabolic behaviour of dz centered about the optical axis. Fig. 4.3 shows a rather linear behaviour of dx with a sign change of dx about the optical axis. The small magnitude indicates a very minor impact of dx, at least for the experimental setup parameters used. Fig. 4.4 shows the plot of dz vs position along with approximations. It can be seen from this figure that dz becomes constant when the paraxial approximation is applied and the result is very close to the exact solution. After applying the small angle approximation as well, it is found that the solution is constant and still close to the exact solution. Hence, both the approximations can be successfully applied for relating interface height and dz for a flat interface.

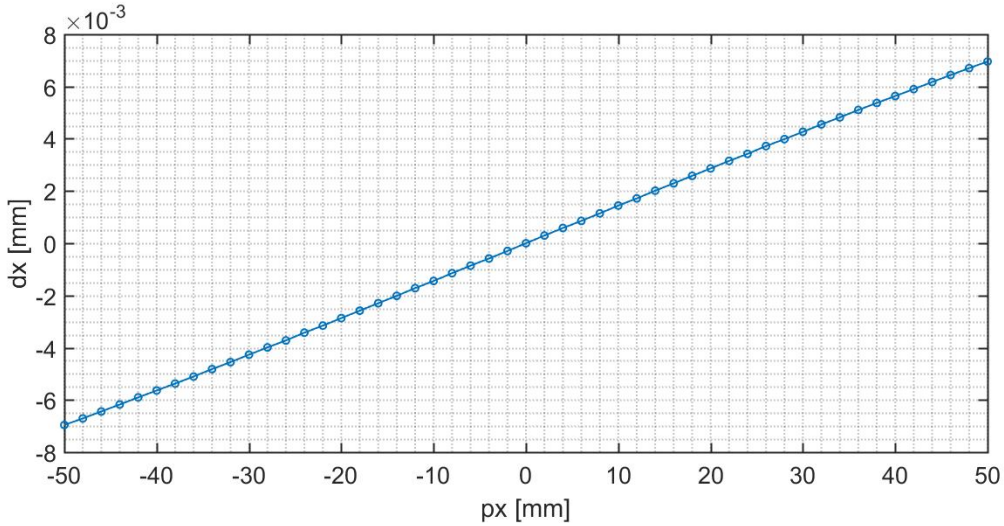

Figure 4.3: Graph of dx vs position on the object plane for a flat interface, solved using exact equations. The behaviour is linear and dx changes sign about the optical axis.

The Fig. 4.5 indicates that there exists a nearly linear relation between the height and dz. It is seen that the impact of dx on the height is insignificant. Hence, dz is the main parameter controlling the interface height for this case. The Fig. 4.5 also shows that the solution found with paraxial and combination of paraxial and small angle approximations match well with

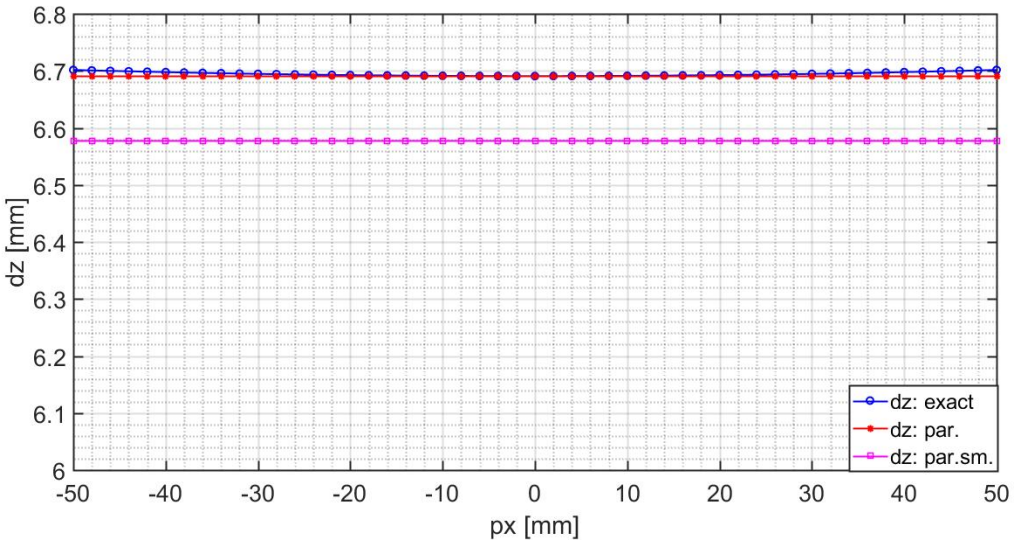

Figure 4.4: Graph of dz vs position on the object plane for a flat interface, solved using exact equations and approximations. All three plots give a good approximation for dz.

the exact solutions. This linear behavior is what was captured in the derived approximated Eq. 4.6 and Eq. 4.8. These are the base equations for the relation between interface height and dz. The Eq. 4.6 is the correlation used in the Chapter 5, since it has a higher accuracy and the camera angle is known.

4.3 Sloped Interface: Derivations and Results

In this section, the behaviour of the pseudo vectors for the sloped interface is studied analytically. The sloped interface study should provide a good idea of the behaviour of the pseudo vectors with the interface slope, which is an important parameter for the actual interface waves. The diagram of the sloped interface ray tracing is shown in Fig. 4.6. This is very similar to the diagram for a flat interface in Fig. 4.1, except that the interface is now sloped. All the concepts and the parameters defined for the flat interface remain valid for this case, except now a new angle θ is introduced into the equations. All important parameters are marked in Fig. 4.6. Subscripts 1 and 2 refer to the right and left camera respectively. The rays have been color coded: red and dark yellow for rays travelling to the left camera from the points C and D respectively and green and dark green for rays travelling to the right camera from the points C and D respectively.

4.3.1 Derivations: Sloped interface

Exact solutions

Like for a flat interface, the derivation begins with finding the unknowns x_1 and x_2 for the intersection of the rays with the interface, refer Fig. 4.6. They can be found by iterating and solving the following equations.

For the Right camera,

$$tan(\frac{\pi}{2} - i_{i,1} - \theta) = \frac{a_1}{b_1 - x_1} \tag{4.9}$$

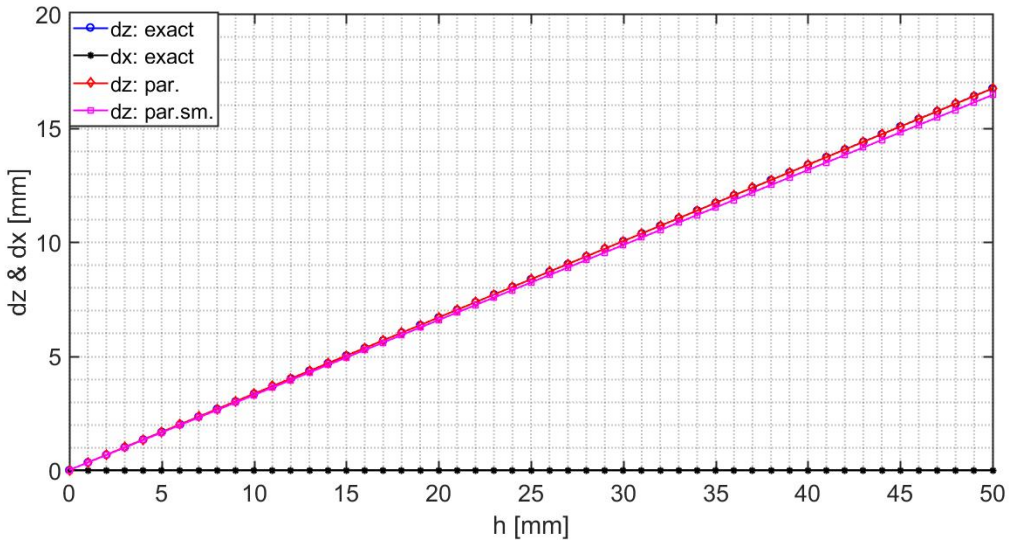

Figure 4.5: Graph of dz and dx vs interface height for a flat interface, solved using exact equations and approximations. The graphs shows a linear variation of dz with increasing height. The approximations match well with the exact solutions.

$$tan(i_{r,1} + \theta) = \frac{x_1}{(D - px - x_1) * tan(\theta)} \tag{4.10}$$

For the Left camera,

$$tan(\frac{\pi}{2} - i_{i,2} + \theta) = \frac{a_2}{b_2 - x_2} \tag{4.11}$$

$$tan(i_{r,2} - \theta) = \frac{x_2}{(D - px + x_2) * tan(\theta)} \tag{4.12}$$

Where,

$$a_1 = L * cos(\alpha) - (D - px + x_1) * tan(\theta)\ ; \quad b_1 = L * sin(\alpha) - px$$
$$a_2 = L * cos(\alpha) - (D - px + x_2) * tan(\theta)\ ; \quad b_2 = L * sin(\alpha) + px$$

Solving together Eq. 4.9, Eq. 4.10 and Eq. 4.3 iteratively, the value of x_1 is found. Solving together Eq. 4.11, Eq. 4.12 and Eq. 4.3 iteratively, the value of x_2 is found. To proceed to find dz and dx, the intersection of the imaginary lines from the two cameras, assuming no interface needs to be found out. They intersect at a point Q as shown in Fig. 4.6. The line equations are as follows:

The line equation for the Left camera,

$$x - \frac{y}{M_2} = px - x_2 - \frac{(D - px + x_2) * tan(\theta)}{M_2} \tag{4.13}$$

where,

$$M_2 = \frac{-L * cos(\alpha) + (D - px + x_2) * tan(\theta)}{L * sin(\alpha) + px - x_2}$$

The line equation for the Right camera,

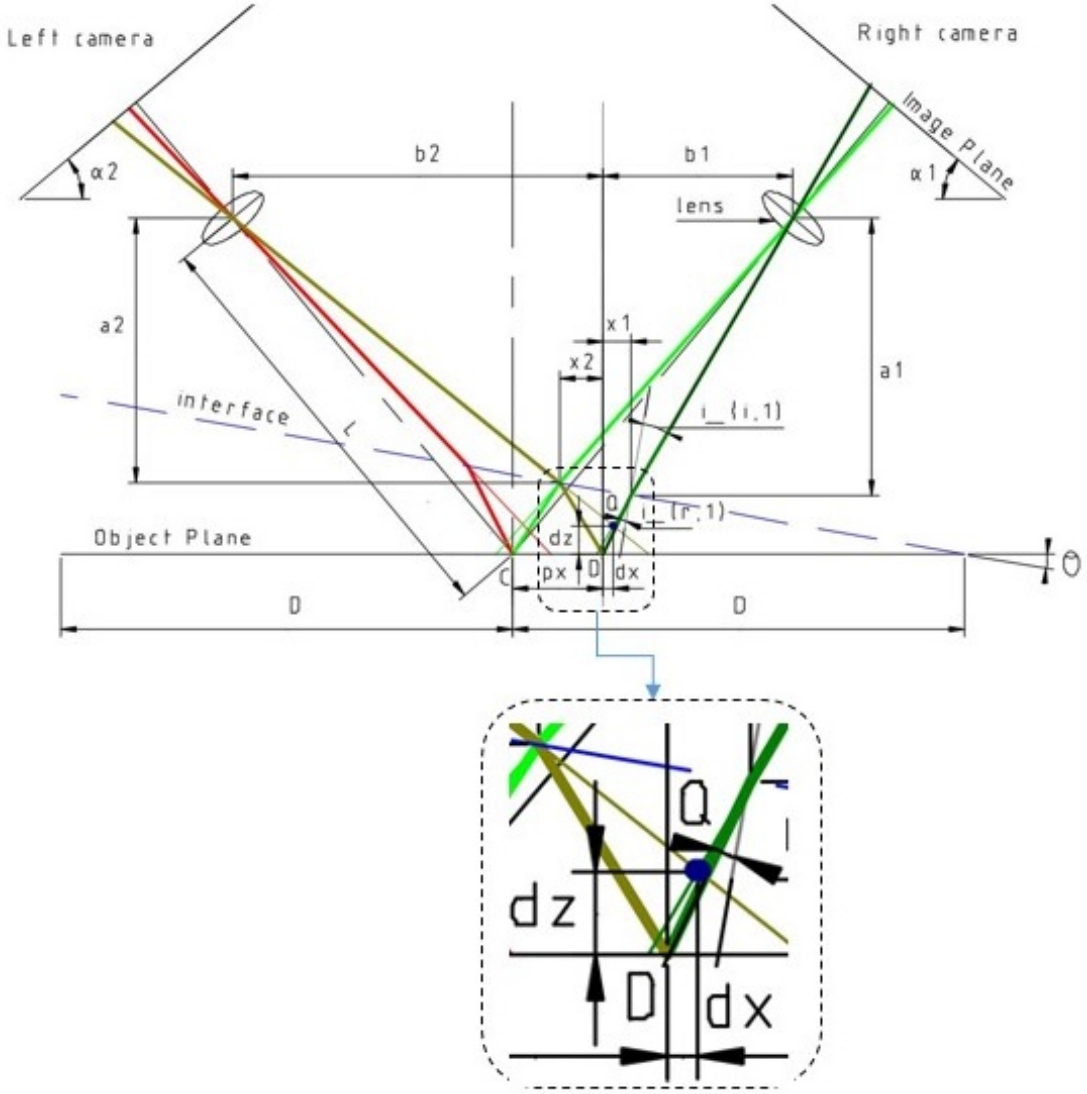

Figure 4.6: CAD model showing ray tracing with application of the Stereo-PIV-SS technique for a sloped interface. The diagram shows the rays originating from points C and D reaching the left and right cameras after refraction at the sloped interface. The rays from the camera can be extended to find the pseudo vector whose end points for location D is marked as Q.

$$x - \frac{y}{M_1} = px + x_1 - \frac{(D - px - x_1) * tan(\theta)}{M_1} \tag{4.14}$$

where,

$$M_1 = \frac{L * cos(\alpha) - (D - px - x_1) * tan(\theta)}{L * sin(\alpha) - px - x_1}$$

Solving together Eq. 4.13 and Eq. 4.14, the end point (Q) of the pseudo vector is found out. The y co-ordinate is the dz projection of the pseudo vector. Position px subtracted from the x co-ordinate gives the dx projection of the pseudo vector. Projections are also shown in Fig. 4.6.

Solution found by applying the paraxial approximation

The incidence angles $i_{i,1}$ and $i_{i,2}$ for a particular θ and α have the same value for any position or slope when applying the paraxial approximation. Hence, no iterations are required to find x_1 and x_2. This makes the calculations less tedious and much more quicker.

$$Here, \quad i_{i,1} = \alpha - \theta \quad and \quad i_{i,2} = \alpha + \theta \tag{4.15}$$

Using these incidence angles and solving together with Eq. 4.9, Eq. 4.10, Eq. 4.11, Eq. 4.12 and Eq. 4.3, x_1 and x_2 are found. Now to find the dz and dx projections, the line equations Eq. 4.13 and Eq. 4.14 need to be solved using the slope values as follows.

$$M_1 = tan(\frac{\pi}{2} - \alpha) \quad and \quad M_2 = tan(\frac{\pi}{2} + \alpha)$$

Solving the line equations, the dz and dx are found and are as follows,

$$dz = \frac{1}{2} * [2 * (D - px) * tan(\theta) + (x_2 - x_1) * tan(\theta) - cot(\alpha) * (x_1 + x_2)] \tag{4.16}$$

$$dx = tan(\alpha) * tan(\theta) * \frac{(x_1 + x_2)}{2} + \frac{(x_1 - x_2)}{2} \tag{4.17}$$

Solution found by applying the small angle approximation

To simplify the solution even further, the small angle approximation is applied. For the sloped interface the approximations shall be very specific. Apart from the regular approximation of angles α and θ to be less than 10^0, two additional approximations need to be applied to get a simplification. These are:

$$k * (\alpha + \theta) < 10 * \frac{\pi}{180} \tag{4.18}$$

$$k * (\alpha - \theta) + \theta < 10 * \frac{\pi}{180} \tag{4.19}$$

The incidence angles $i_{i,1}$ and $i_{i,2}$ are known as per the Eq. 4.15. Applying Snell' law (Eq. 4.3) and the small angle approximation, the refracted angles are found. They are as follows:

$$i_{r,1} = k * (\alpha - \theta) \tag{4.20}$$

$$i_{r,2} = k * (\alpha + \theta) \tag{4.21}$$

To find the intersection for the Left camera ray with the interface Eq. 4.12 and Eq. 4.21 are solved. Applying the small angle approximation and the approximation in Eq. 4.18:

$$x_2 = \frac{(D - px) * \theta * (k * (\alpha + \theta) - \theta)}{1 - \theta * (k * (\alpha + \theta) - \theta)}$$

Neglecting higher order terms,

$$1 - \theta * (k * (\alpha + \theta) - \theta) \approx 1$$

Hence, the approximated value of x_2 is,

$$x_2 = (D - px) * \theta * (k * \alpha + \theta * (k - 1)) \tag{4.22}$$

In a similar way as above, the x_1 value for the Right camera is found. Solving together Eq. 4.10 and Eq. 4.20 by applying small angle approximation and the approximation in Eq. 4.19, the approximated value of x_1 is found as follows:

$$x_1 = (D - px) * \theta * (k * \alpha + \theta * (1 - k)) \tag{4.23}$$

Finally, applying these x_1 (Eq. 4.22) and x_2 (Eq. 4.23) values in Eq. 4.16 and neglecting higher order terms, the following expression for dz is found,

$$dz = (D - px) * \theta * (1 - k) \tag{4.24}$$

This expression is very similar to the flat interface result found in Eq. 4.8. Hence, even for a sloped interface a simple linear relation is found between interface height and dz, although with many more approximations.

Solving together Eq. 4.22, Eq. 4.23, Eq. 4.17 and neglecting higher order terms, the following expression for dx is found,

$$dx = (D - px) * \theta^2 * (1 - k) \tag{4.25}$$

The above approximations for dx and dz are found by applying the paraxial, small angle and approximations as mentioned in Eq. 4.18 and Eq. 4.19. Therefore, knowing the refractive index ratio and playing with the angles θ and α to match the approximations, it is expected the these relations can provide a good approximation for the interface height.

4.3.2 Results: Sloped interface

The equations derived in Sec. 4.3.1 are used to make the plots of dz and dx versus the position on the object plane and the slope of the interface. The position in the graphs is defined on the object plane with a value of px=0 assigned for the optical axis. The ray tracing diagram for the sloped interface is shown in Fig. 4.6. For the sloped interface also, the experimental setup described in Chapter 5 is taken as a reference for the input data. The input parameters used for the sloped interface computations are as follows:

$$\theta = 8^0; \quad L = 1600\ mm; \quad \alpha = 10^0; \quad k = \frac{n_1}{n_2} = \frac{1}{1.49}; \quad D = 50\ mm;$$

Fig. 4.7 displays the behaviour of the exact and approximate solutions of dz and dx vs the position on the object plane. It is observed that both dz and dx increase with the interface height and follow the shape of the interface. Almost linear behaviour is observed between the dx & dz and px. Linear behaviour for dz was also indicated in the approximate equations in Eq. 4.24. The paraxial approximations for dx and dz very closely match the exact solutions. The small angle approximations for this case also give an accurate estimate for dz and dx when compared to the exact solutions. Moreover, an additional flat interface paraxial approximation equation, Eq. 4.6, has been plotted in Fig. 4.7, using the interface height which is known from the slope and position. For this equation, the interface is assumed as a flat interface and the incidence angle (i_i) is equal to the camera angle (α). Even this approximation yields a good solution for dz as compared to the exact solutions. Therefore, the simple relation in Eq. 4.6 obtained for a flat interface, can be applied even to a sloped interface with reasonable accuracy. Thus, Eq. 4.6 is the basis of the correlation to be applied for converting dz to interface height in Chapter 5.

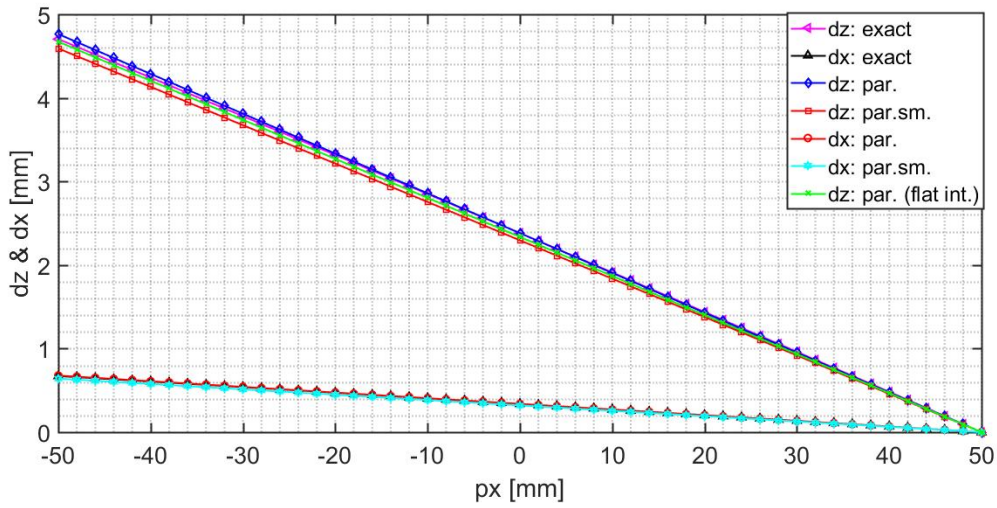

Figure 4.7: Graph of dz & dx component of the pseudo vector vs position on the object plane for a sloped interface, solved using exact equations and approximations. Behaviour is almost linear for both dz & dx and the approximations match well with the exact solutions.

Fig. 4.8 displays the behaviour of dz and dx with respect to θ. The exact solutions show a gradually increasing nonlinear curve for both dz and dx. Like a flat interface, dz is more in magnitude as compared to dx for a particular height (here slope). But with increasing θ, especially more than 10^0, the magnitude of dx also becomes significant. So if the interface height of waves with slopes higher than about 10^0 need to be measured, then even dx needs to be considered in the correlation along with dz. For the paraxial approximation solution, both dz and dx very closely match the exact solution. Applying the small angle approximation gives a linear behaviour for dz. Both dx and dz for this case match with the exact solutions for θ values less than 10^0, but for higher θ they start deviating. A similar behaviour is seen when plotting the flat interface paraxial approximation, where the linear relation for a flat interface as mentioned in 4.6 can be successfully applied to find dz from the exact height for a sloped interface. For this case also the dz and dx values start start deviating from the exact solutions for θ greater than 10^0. It is also possible to find the interface height of a sloped interface from dz using the flat interface correlation, Eq. 4.6. The error between the height computed from dz (exact solution) using correlation 4.6 and the exact height for a sloped interface is plotted in Fig. 4.9. A nonlinear increase in the error with increasing interface angle is observed. The error is within sub millimeter range for θ less than 17^0. Hence, the correlation 4.6 can be applied to find the interface height, h, from dz for low interface slopes. This is an important finding and is applied in the Chapter 5.

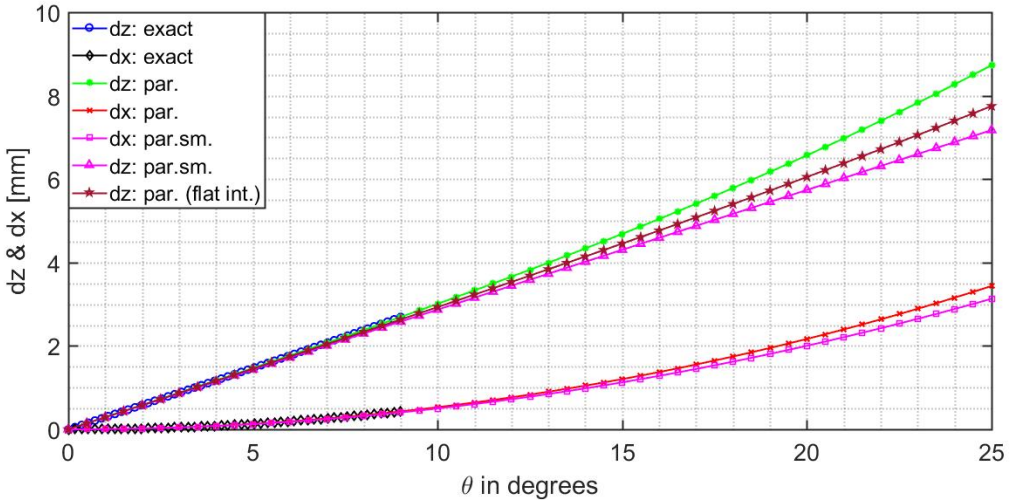

Figure 4.8: Graph of dz & dx component of the pseudo vector vs θ for a sloped interface, solved using exact equations and approximations. Behaviour is nonlinear for paraxial and exact solutions which match well. The small angle approximation develops significant error after $\theta = 10^0$

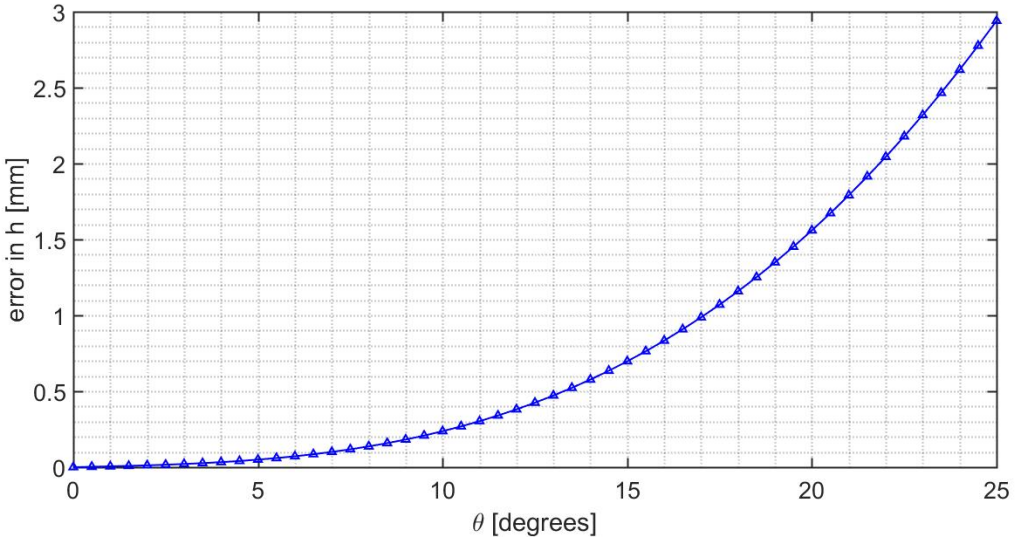

Figure 4.9: Error between the exact interface height and the height computed from dz (exact solution) using correlation 4.6 for a sloped interface is plotted versus the interface slope, θ. A nonlinear increase in the error with increasing θ is observed.

Chapter 5

Experiments

After laying a foundation for the techniques in Chapter 3, finding important relations for the interface height in Chapter 4 and also testing the technique with synthetic data in Appendix B, the next step is to better understand the applicability of the technique to reality. Hence, a comprehensive set of experiments were carried out for the Stereo-PIV-SS technique to better understand the real physical phenomena. Moreover, the experiments are a valid reference to compare the analytics and the ray tracing code output to reality. The first set of experiments were conducted with transparent solid Plexiglas and Glass profiles to fine tune the setup, test correlations and observe the reconstruction behavior for various parameters. The next set of experiments were conducted to test the method on actual water waves in a ripple generation setup. After studying the results, the applicability and limits of the proposed experimental techniques are discussed.

5.1 Setup details

A schematic of the experimental setup is shown in Fig. 5.1. The figure also shows the sign convention and sections X0 and Y0 taken for the reconstruction. The important camera equipment details are mentioned in Sec. 5.1.1. All other equipment are detailed in Sec. 5.1.2. See Appendix C for images of the setup and equipment.

5.1.1 Camera Configuration

See Fig. 5.1. Two cameras are used in a Stereo configuration at angles α_1 and α_2 for the Stereo-PIV-SS technique. A vertical camera configuration is adopted for the FS-SS technique. The field of view (FOV) for the cameras is selected as 100 x 100 mm^2, considering the air cavity closure dimensions to be studied in the cavitation tunnel setup. The camera configuration consists of the following equipment:

- *Camera Support*: The cameras are supported on a tall support frame at a height of 1850 mm from the ground. The camera to reference plane distance (H) is 1600 mm and is kept high enough for the paraxial approximation as described in Chapter 4 to be valid. A high lateral spacing between the stereo cameras of up to 1600 mm is achievable using this setup, which allows for the use of high camera angles. A camera holder is used for tilting the cameras to the required angle.
- *Cameras*: All the three CCD cameras have the same specifications and are of brand name LaVision Imager pro X. The camera resolution is 2048 x 2048 pixel^2. To confirm whether the resolution is sufficient, consider an interrogation window (IW) size of 28 x 28 pixel^2 with an overlap of 50 % which corresponds to a resolution of 0.7658 mm for a

vertical camera configuration (see Sec. 5.2.1). Consider a resolution of 16 displacement vectors required per interface wavelength which means a minimum wavelength of about 10 mm can be smoothly captured with this camera resolution. This is within the range of the waves to be captured in the water wave experiment and hence the resolution selected is sufficient. The cameras have a frame rate of 13.52 fps, which is suitable to capture a time series of the wave phenomena for the water wave experiments. The aperture for both cameras was set small enough, with an $f\#$ of 11, so that the depth of focus is sufficient to capture the whole FOV with proper focus. This also helped to avoid any use of a Schiempflug configuration [34].

- *Camera Lens*: To select the lens focal length (f), the thin lens equation is solved, see Eq. 5.1. In this equation, $O.D.$ is the distance between the reference plane and the lens, which is approximately 1600 mm and $I.D.$ is the distance between the image plane and the lens which is approximately 225 mm for the setup. Solving the thin lens equation, the focal length is found to be 197.26 mm. Hence, a camera focal length of 200 mm was selected.

$$\frac{1}{O.D.} + \frac{1}{I.D.} = \frac{1}{f} \tag{5.1}$$

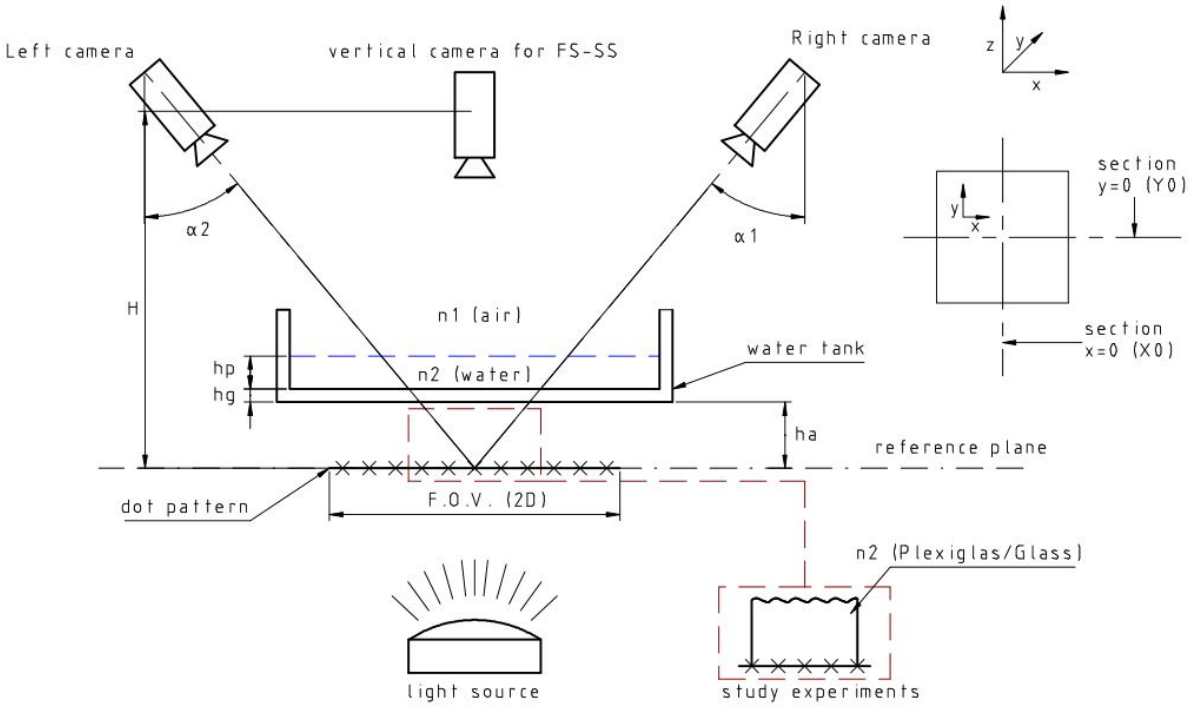

Figure 5.1: Schematic for the Experimental setup. Two cameras are placed in a stereo configuration for the Stereo-PIV-SS technique and one camera is placed vertically for the FS-SS technique. For the study experiments, the Plexiglas and glass profiles are placed directly on top of the dot pattern and for the water wave experiments, the water tank is place at a distance h_a from the dot pattern. A light source is placed below the random dot pattern for sufficient illumination. The sign convention is shown and also the sections to be analyzed are shown on the xy plane.

5.1.2 Table equipment

All the remaining equipment for the setup were placed on a table of height 745 mm. The calibration grid and the random dot pattern were printed on a glass plate at the company De Resolutie Rijswijk B.V. The important table equipment are as follows:

- *Calibration target*: The calibration target consists of 23 x 23 black dots forming a grid with each dot of 1 mm diameter and 5 mm spacing between any two adjacent dots. The calibration grid is printed on a 120 x 120 x 20 mm^3 transparent glass plate. The grid consists of dots printed in black ink on the glass.

- *Random dot pattern*: The random dot pattern has been selected after doing free surface reconstruction testing with multiple dot pattern designs. The random dot pattern selected for the experiments has a specification of, dot density: 40 %, dot diameter: 0.2 mm and a minimum dot spacing in percentage of dot diameter: 3 %. The size of each dot is about 4 pixels for a vertical camera configuration, which should help in avoiding any peak locking effect. The random dot pattern is printed on a 120 x 120 x 20 mm^3 transparent glass plate. These are transparent dots with a black background printed around. The dot pattern was generated using an in-house code.

- *Other equipment*: A light source (LED panel) is placed below the dot pattern as shown in Fig. 5.1 to have enough illumination intensity in the captured images. A calibration target shift plate was used to achieve a shift in the calibration target required for the calibration procedure of the Stereo-PIV-SS technique, see Sec. 3.1.2. The plate is 1.87 mm thick and made of glass.

5.2 Study experiments

Detailed study experiments were conducted as a first step to test the free surface measurement techniques. A schematic of the setup for the study experiments is shown in Fig. 5.1. These set of experiments helped in fine-tuning the experimental and post processing procedures and studying important parameters. Moreover, they helped in studying the quality of reconstruction for the techniques and testing the important correlations found from analytical solutions. The experiments were conducted on solid Plexiglas and glass lens profiles having a defined interface shape. The Plexiglas profiles have been machined for high precision at DEMO, Delft. Even though the Plexiglas profiles have been machined for high precision and also the lens profiles are expected to be very accurate, a tolerance error in machining of the order of 0.01 mm is expected to be a part of the error in reconstructed height. The OrX and OrY naming is used to define the different orientations of placing a profile varying only in one direction. For example, for the Plexiglas wave profile used in the study experiments, the cosine wave placed along the x axis is oriented in the OrX direction and along the y axis in the OrY direction. The x and y axes are defined as per the coordinate system mentioned in Fig. 5.1. The sections, X0 and Y0, are also defined in Fig. 5.1. The naming meanX0 and meanY0 are used to define the mean profile which is the mean of all sections parallel to sections X0 and Y0 respectively for a unidirectional wave interface. Wherever required, the sections and the mean profiles are shifted to the origin along the axes to account for the error in placing the Plexiglas profile at the origin during the experiments. The object plane position (px) for all the plots in the forthcoming sections is defined on a 0 to 100 mm scale for the FS-SS technique and on a -50 to 50 mm scale for the Stereo-PIV-SS technique. The images of the Plexiglas and lens profiles are in Appendix C. The details of the solid profiles used for the experiments are as follows:

- *Plexiglass profiles*: Two Plexiglas profiles were used for the experiments, one a flat interface profile which is a cuboid of height 20 mm and cross section of 100 x 100 mm^2. The other is a wave interface profile of mean height 20 mm and cross section of 100 x 100 mm^2. A cosine wave profile is machined in one direction about the mean height. It has an amplitude of 0.5 mm and wavelength of 20 mm. A similar set of profiles were also used in [29].

- *Lens profiles*: Two glass lens profiles were used for the experiments. One is a spherical convex lens of 300 mm focal length and another is a spherical concave lens of 300 mm

focal length with curvature only in one direction. The exact shape of the profiles are described in the plots of Sec. 5.2.2, Fig. 5.9 and Fig. 5.11.

5.2.1 FS-SS method

The FS-SS technique [29] is a proven technique capable of measuring small amplitude and small slope deformations in transparent media. This technique has been successfully applied to measure small amplitude waves generated due to droplets bouncing on a vibrating bath, also termed as a walker, in [36] and [37]. The technique has been also applied to measure small deformations in PDMS micro channels in [38]. Moreover, the technique has also been applied to measure the surface deformations of wind waves on a viscous liquid in [39] and measuring the water droplet impact on a water surface in [29]. Therefore, it will serve as a reliable comparison for the Stereo-PIV-SS technique to be tested on small amplitude and slope water waves in Sec. 5.3. An introduction to the concept and important equations were presented in Chapter 2. To fine tune the procedure for this technique and check the quality of results with the current setup, some experiments on Plexiglas wave interfaces were performed.

Experimental Procedure

The FS-SS technique setup consists of a camera looking at the FOV vertically, as shown in Fig. 5.1. Firstly, an image of the calibration target placed at the reference plane is captured to get the mm-pixel relation. After this step, two synthetic Schlieren images with a random dot pattern are captured. First one with a flat mean interface and another one with the wave interface that is to be measured.

Post processing

The post processing is performed using an in-house code with the camera images as an input. Firstly, the displacement field is computed using a cross correlation based PIV algorithm. For details about PIV displacement field computation see [34]. The two Synthetic Schlieren images are processed to find the displacement field ($\delta\vec{r}$). The IW size for computing the displacement field is selected so that it should be less than $\frac{1}{8}^{th}$ the size of the smallest wavelength with an overlap of 50%. The IW size should also allow a particle density of at least 10 dots per IW. Lower particle density IW sizes limit the number of vectors generated which ultimately hinder a smooth reconstruction. Rectangular IW's are selected for the Plexiglas wave profile since the wave and hence the deformations are only in one direction. For this case, a smaller IW size is selected along the wave direction for a smoother reconstruction. For all other profiles, square IW's are used. A median filter is used for filtering any spurious vectors from the displacement field. The cross correlation function was checked for random image pairs and a distinct correlation peak was observed within each window, which signified a good quality displacement field computation.

After finding the displacement field from the images, the displacement field is subtracted by its mean value, as also suggested in [29]. This helps in getting rid of any erroneous gradient in the reconstruction if the camera angle is not exactly zero or if there are any disturbances due to slight camera vibrations [29]. These refined displacements in both the x and y directions are converted into object plane co-ordinates by multiplying it with the mm-pixel correlation calculated from the calibration. These displacements along the x and y directions are used in Eq. 2.1 to get the surface gradients in both the directions. A refractive index of 1.49 is used for the Plexiglas profiles. These gradients are integrated to find the free surface profile about the mean interface height. More details on the integration step can be found in [29]. Adding the mean flat interface height to this surface profile gives the final reconstructed profile of the free surface.

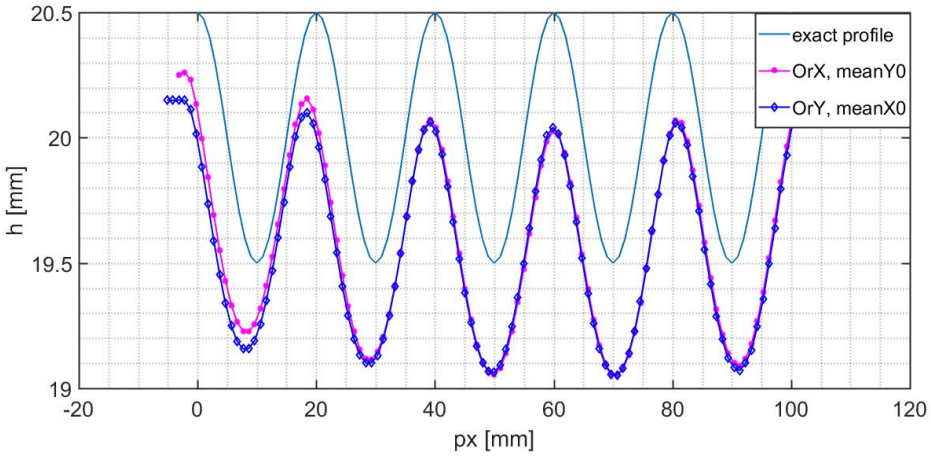

Figure 5.2: Mean profiles of the Plexiglas wave profile oriented in two directions, OrX and OrY, reconstructed using the FS-SS technique plotted versus the position on the object plane, px. The mean profiles, meanX0 and meanY0, are compared to the exact profile. The graph shows a good accuracy in the amplitude and wavelength captured by the FS-SS technique.

Results and Discussions

The reference image is taken with the Plexiglas flat interface profile and the next image is captured with the wave interface Plexiglas profile. An IW size of 36 pixels is used in the wave direction to compute the displacement field. This multiplied by the mm pixel relation of 0.0532 mm/pixel found from calibration images provided a final resolution of 0.9576 mm in the wave direction. Larger IW sizes can be selected for the direction orthogonal to the waves, since there is no deformation in that direction.

The mean profile height is plotted versus the position on the object plane, as shown in Fig. 5.2. The mean profiles, meanX0 and meanY0, for both orientations, OrX and OrY, along with the exact profile are plotted. The graphs indicate a smooth reconstruction with the amplitudes and wavelengths almost exactly matching with the exact profile shape. Moreover, the profiles of the interface for both the orientations match very closely. A mean relative error of 2 % in the absolute height is observed. This accuracy is considered to be a good enough as it is within sub millimeter precision. Moreover, the absolute height accuracy for FS-SS is not mentioned in [29]. The relative error in the amplitude value is approximately 3 % which is very close to the limiting accuracy of this technique and in the micro millimeter range. The relative error in the wavelength is about 3.38 % which is in the sub millimeter range and hence it is acceptable. This could possibly be improved with the remapping correction as mentioned in [29], but this accuracy is deemed sufficient for the current research.

Additionally, this study showed a high dependence of the IW size selected on the reconstructed absolute height and the amplitude of the waves. Hence, an optimum IW size of 36 x 50 pixel^2 was selected for the OrY wave and an IW size of 50 x 36 pixel^2 was selected for the OrX wave. This IW size by wavelength ratio (36/20 pixels/mm) is also used for the water wave experiments.

The impact of inducing an error in the reference flat interface height and image selected on the reconstructed profile is shown in Fig. 5.3. The exact height of the reference flat interface is supposed to be 20 mm. There are two possible sources of error related to the reference flat interface, one due to an incorrect input of the flat interface height value (h_p) in Eq. 2.1 and another from improper height selection for the reference image. The first subplot (a), is for an error in the height input into the equations but with a proper reference image at the exact flat interface height. Because of the incorrect height input, there is an obvious difference in the absolute height, but also the error in the amplitude goes on increasing with the error in flat interface height input. The relative error in flat interface height is marked in the legend and the corresponding relative error in the amplitudes are 8 % (10 %), 30 % (25 %) and 94 % (50

%). The second subplot (b) demonstrates the impact of selecting an incorrect reference image, in this case a no interface reference image. The graph shows a magnification effect on the profile and this induces an error on the profile shape recorded. The most probable source of error is shown in subplot (c), which is a combination of the errors in cases of subplots (a) and (b). For this case, an image of a reference flat interface of height 5.4 mm was used and also the height of 5.4 mm was used as input value. Subplot (c) shows a clear error in amplitude and also a magnification effect when compared to the exact profile shape.

The analysis with the plots in Fig. 5.3 shows that if the exact image and the exact height of the reference flat interface interface are not used for the FS-SS technique, the method generates inaccurate results. An air cavity is always unstable, hence the mean interface image cannot be captured accurately. Therefore, the FS-SS technique cannot be used for an air cavity.

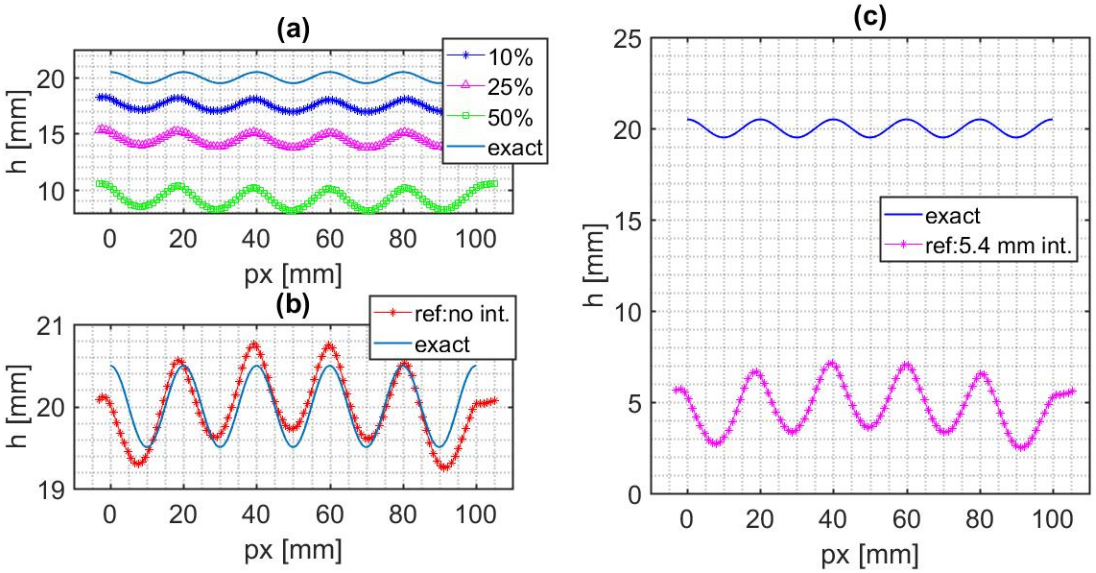

Figure 5.3: Figure shows subplots for errors in the reference flat interface height and image selected for the FS-SS technique. Mean profile meanY0 of the Plexiglas wave profile oriented in the OrX direction is plotted versus the position on the object plane, px. Subplot (a) is for an error in the reference flat interface height mentioned in the equations, subplot (b) is for an error in the selection of the flat interface reference image and subplot (c) is for a combination of errors in (a) and (b). The errors for each case are significant and proves the FS-SS technique cannot be applied without having the exact reference flat interface height and image.

5.2.2 Stereo-PIV-SS

The concept behind this technique is introduced in Chapter 3. Analytical solutions found in Chapter 4 helped in finding the correlation between interface height and pseudo vector, dz. To further extend the understanding for this technique, a detailed experimental study was performed using Plexiglas and glass interfaces. The procedure followed for finding the reconstructed interface height using the Stereo-PIV-SS technique is as follows:

Experimental Procedure

For each trigger, an image is captured by both cameras simultaneously and stored as one single stereo image data. Two sets of such images captured with a Stereo camera configuration are required for the experiments and are as follows:

Calibration: The calibration step involves the capture of two stereo images at two known locations in the field of view. One calibration stereo image is captured at the reference plane.

Another is captured at a plane shifted from the reference plane by a known height using the calibration plate.

Synthetic Schlieren images: In this set also two stereo images are captured. One is captured without any interface with the cameras directly looking at the random dot pattern. Another image is captured by placing the interface to be measured, above the reference plane.

Post processing

The post processing is performed using an in-house Stereo-PIV code based on [34]. The code works as follows:

Calibration: The code takes the input of the calibration stereo images set and the user selects the (0,0), (0,1) and (1,0) co-ordinates in all the images. Using this input from the user, the calibration marker spacing and the calibration target shift, the code generates mapping functions to relate the object field to the image field. Refer the calibration procedure for Stereo PIV mentioned in Chapter 3.

Reconstruction: After the calibration step, the code takes the input of the Synthetic Schlieren image set. It computes the displacement in pixels from these images. The details of the displacement field computation step is the same as mentioned in the post processing step in Sec. 5.2.1. This displacement field is interpolated onto a mapping of the user defined grid in the object plane. After this, the displacements are used in the augmented system of equations as described in Chapter 3, Sec. 3.1.2. Solving these augmented set of equations gives the three components of the pseudo vectors, dx, dy, and dz. dz is multiplied by the correlation factor derived in Chapter 4 Eq. 4.6 and plotted versus a user defined grid to generate the final reconstruction. The camera angles as per the setup and the refractive index of the medium is used for computing the correlation factor. Standard refractive index of 1.49 is used for Plexiglas, 1.52 is used for the flat glass interfaces (10 mm and 1.87 mm) tested and 1.5 is assumed for the glass lens interfaces.

Exact interface profiles for comparison: The exact profile shape for the Plexiglas flat and wave interfaces are well defined. For the glass lens interface no drawing of the profile was available. To find the exact profile, first it is assumed that the lens is a spherical lens. Moreover, for both the lens one side is flat and the other side has a curvature. Applying the formula for a standard thin lens with curvature only on one side,

$$\frac{1}{f} \approx (n-1) * \frac{1}{R} \tag{5.2}$$

Assuming a refractive index of 1.5 for the glass lens, which is a very realistic value for a typical crown or CR-39 glass lens, it is found that the radius of curvature (R) is exactly half of the focal length (f) and has a value of 150 mm for both the lens studied (Eq. 5.2). The exact profile of the lens can be found from R and some dimensions measured from the lens.

Results and discussions

Flat interface:

The first set of experiments for this technique were conducted on flat interface profiles. This should be a good starting point for the study of this technique and should serve as a good comparison to the analytical solutions found in Chapter 4 for a flat interface. A high IW size has been used for the displacement filed computations, ranging from 80 to 100 pixels square interrogation windows. This is because there is no curvature in the interface and a smooth flat interface profile can be generated with large IW sizes without compromising on accuracy.

The first set of results with a flat interface are for varying camera angles for the Plexiglas flat profile of 20 mm height. Fig. 5.4 contains two subplots, one for the meanY0 profile and another for the meanX0 profile plotted for different camera angles versus px. The subplots

also contain the exact profile for comparison. The meanY0 profile is the section in the same plane as the one analyzed for the flat interface analytical solutions in the Chapter 4. Although there is no definite shape observed, it can be noted that the method can very accurately predict the interface height for different camera angles. Moreover, the meanX0 profile is plotted on a larger scale to show that the error is much smaller in magnitude as compared to the absolute interface height. The maximum relative error in the reconstructed profile along the px axis considering both the mean profiles is 1.5 %. The relative error for the three camera angles when comparing the mean interface height for the complete 3D reconstruction is 0.073 % for 23.5^0, 0.353 % for 10^0 and 0.097 % for 5^0, which is sufficiently accurate in the micrometer range.

Fig. 5.5 shows the meanY0 profiles plotted versus px for varying interface height. A good match with the exact profiles is seen from the graph. The error in the mean interface height when compared to the exact height for each flat interface reconstruction is 0.2447 mm for the 1.88 mm interface, 0.1623 mm for the 10 mm interface and 0.0138 mm for the 20 mm interface. The error for the 1.88 mm and the 10 mm glass interfaces are relatively higher than the Plexiglas interface because these are not high precision machined interfaces like the Plexiglas interface. Moreover, there could be a possible sub millimeter error in the manual measurement of the interface height which is used as the exact height for comparison. Also, the refraction index of the glass media for these interfaces is not exactly known for the conversion factor computation, and assumed to be of a standard value of 1.52. In any case, a sub millimeter precision in the measured interface height is achieved. Hence, it can be concluded that the Stereo-PIV-SS technique can capture the interface height of a flat interface with sub millimeter accuracy.

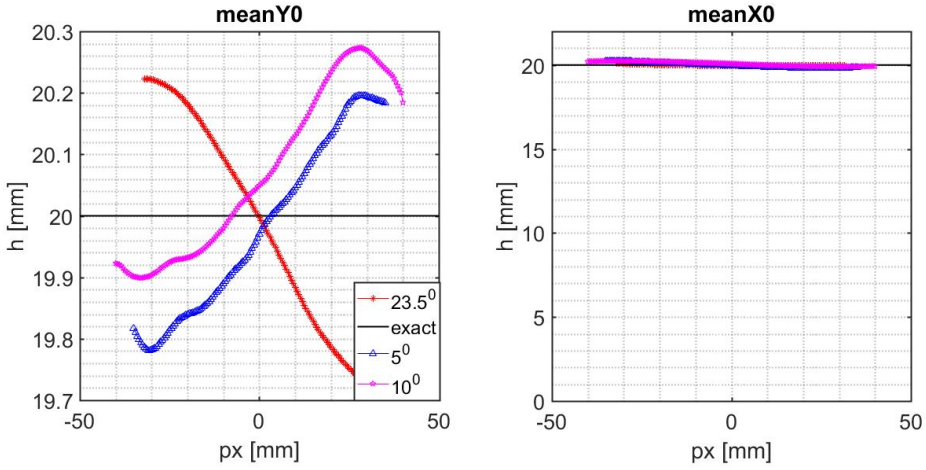

Figure 5.4: Mean profiles, meanY0 and meanX0, of the Plexiglas flat interface profile reconstructed using the Stereo-PIV-SS technique is plotted with respect to the position on the object plane. The graph shows a good accuracy of the absolute height captured by the technique for the different camera angles studied. The same legend is to be followed for both the subplots.

Plexiglas wave interface:

The next interface studied is the Plexiglas wave interface to check the reconstruction quality for a wavy profile. Fig. 5.6 shows the section X0 plotted versus px for varying camera angles and with the wave orientation OrY. It was found that the mean profiles almost exactly match with the section profiles for all angles and orientations, an example is shown in Fig. 5.6 for camera angle 23.5^0. The error in the amplitude is approximately 0.08 mm for each of the angles which corresponds to 8 % relative error. The error in the wavelength is 0.5 mm for all the angles which corresponds to a 2.5 % relative error. There is some variation in the absolute height along the px axis, as also seen for the flat interface reconstructions, which is maximum 0.38 mm in magnitude considering all angles and all positions. This translates to about 1.9 % relative error as compared to the exact interface height. All the errors are within acceptable limits and hence the reconstruction method with the conversion factor proposed

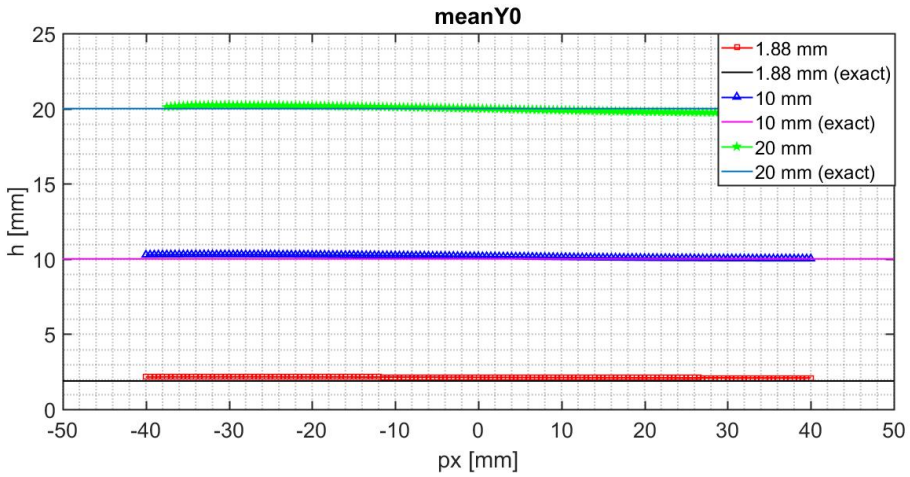

Figure 5.5: The mean profile meanY0 for the Plexiglas flat interface profile reconstructed using the Stereo-PIV-SS technique is plotted with respect to the position on the object plane. The profiles for different interface heights are plotted. A good accuracy in the mean profile when compared to the exact height is observed.

can predict the interface height accurately for wave orientation OrY.

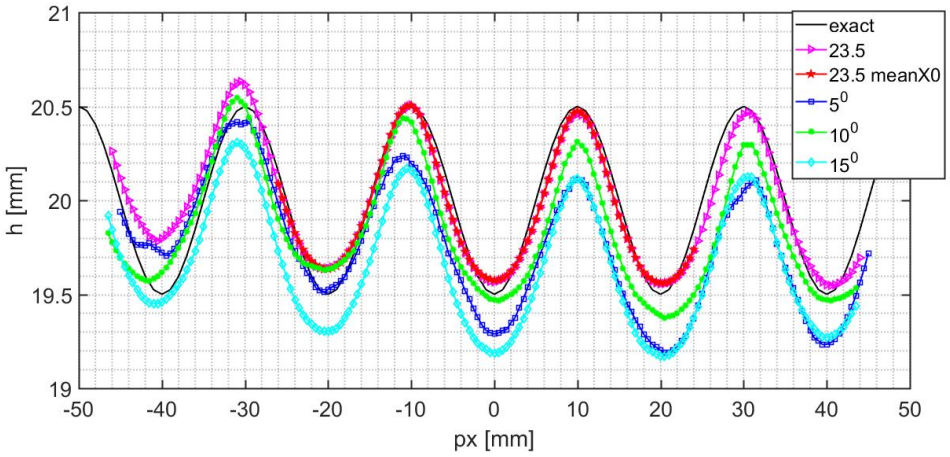

Figure 5.6: Section X0 for the Plexiglas wave interface reconstructed using the Stereo-PIV-SS technique plotted with respect to the position on the object plane for varying camera angles. The wave interface is oriented in the OrY direction. A good accuracy in the section profile when compared to the exact profile is observed.

Fig. 5.7 shows the section Y0 versus px plot for the wave interface placed in the OrX orientation. The wavelength is well captured with a 2.5 % relative error, and has the same accuracy as seen for the orientation OrY. The mean flat interface height is captured with sub millimeter precision when comparing to the mean of the interface computed by this technique. The mean interface height computed for each angle and the errors are: 0.286 mm for 5^0, 0.12 mm for 10^0, 0.101 mm for 15^0 and 0.15 mm for 15^0.

The main observation is that the reconstructed profile is much larger in magnitude when compared to the exact profile and the amplitudes are reversed for all angles. This was not observed for the OrY orientation. Hence, the reconstruction using Stereo-PIV-SS is orientation dependent. This behaviour can be explained as follows. For the OrY orientation, the interface slope is along a plane orthogonal to the plane which contains the optical axis of both the cameras (see Fig. 5.1). Hence, considering the paraxial approximation, the interface incidence angle of the light rays entering the cameras are independent of the interface slope. Therefore, the reconstruction behaviour is similar to that of a flat interface. For the orientation OrX, the interface slope is in the same plane as the camera angles. Hence, the

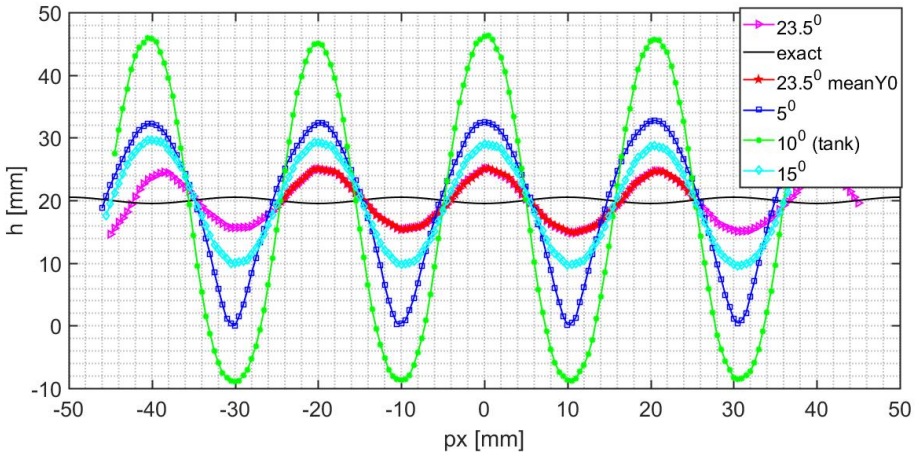

Figure 5.7: Section Y0 for the Plexiglas wave interface reconstructed using the Stereo-PIV-SS technique plotted with respect to the position on the object plane for varying camera angles. The wave interface is oriented in the OrX direction. An amplitude reversal and also much larger amplitude magnitudes than the exact profile is observed. The wavelength is captured accurately by the technique. Also the mean interface height can be found with sub millimeter precision when taking the mean of the interface.

incidence angle at the interface is the camera angle plus the interface slope at that location. This is more clearly shown in Fig. 5.8 where the camera axis plane for the two orientations are shown for a Plexiglas wave interface. For the OrY orientation, the interface behaves like a flat interface and for the OrX orientation the incidence angles are influenced by the wave interface slope. A combination of this changed incidence angle and high mean interface height of the mean interface is expected to have played a role in this reconstruction behaviour. Hence, the conversion to the interface height only considering dz is impacted highly by the interface slope in the camera angle direction and also the mean interface height of the interface. Thus, the conversion factor found in Chapter 4 is not directly applicable for this orientation. The conditions for observing an amplitude reversal is explained in 5.4 using analytics.

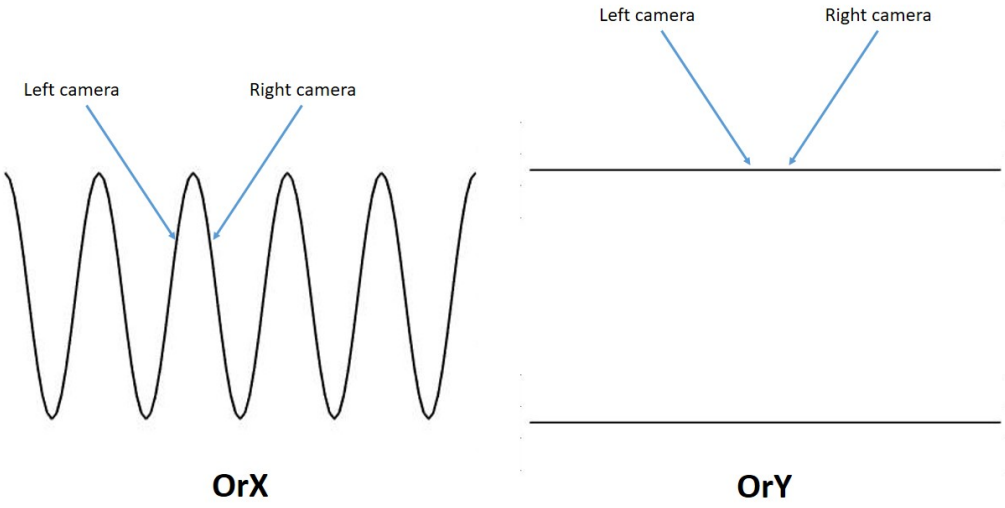

Figure 5.8: The camera axis plane is shown for two different wave orientations, OrX and OrY for the Plexiglas wave profile. For the OrX orientation it is seen that the light ray incidence encounters a sloped interface as compared to the OrY orientation where the light rays encounter a flat interface. Thus geometrically the OrY orientation behaves as a flat interface and for the OrX orientation a different incidence angle is observed which impacts the reconstruction.

Lens profiles:

In addition to the Plexiglas interfaces, two glass lens interfaces were studied using the Stereo-PIV-SS technique. These profiles have low interface slopes and mean interface height and hence would be an interesting case to check if the reconstruction quality can be improved for all orientations. The pictures of the different lens profiles used are shown in Appendix C and the exact profiles are plotted in each graph for comparison to the reconstruction. For all the graphs plotted, the section profiles are shifted to the reference plane along the height (h) axis to match the flat part to $h = 0$ for an exact comparison of the profiles. Firstly, the sections X0 and Y0 of the unidirectional spherical concave lens of focal length 300 mm is plotted for both orientations versus the position px in Fig. 5.9. The interface is studied with a high camera angle of 23.5^0. The reconstruction with the Plexiglas wave interface pointed at a wave orientation dependency, but the reconstruction with this concave lens profile is independent of the wave orientation. Moreover, it is seen that the sections in both the directions match very accurately with the exact profile shape, except for the sharp edges. The sharp edges shown in the exact profile are actually chiseled in the manufactured profile and not transparent. Hence, they cannot be captured accurately by the reconstruction. Apart from this, it is observed that this method captures the interface shape very well in both the orientations for all the sections. The maximum error in the profile leaving the edges are 0.1789 mm for OrX-Y0, 0.1 mm for OrX-X0, 0.2137 mm for OrY-Y0 and 0.2 mm for OrY-X0. Hence, a sub millimeter precision is achieved.

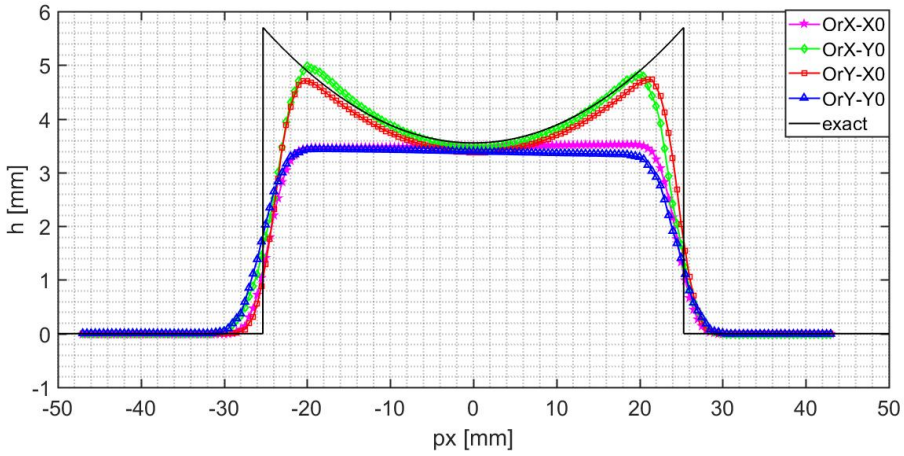

Figure 5.9: The sections, X0 and Y0, for the unidirectional spherical concave lens interface of focal length 300 mm, reconstructed using the Stereo-PIV-SS technique plotted versus px for both orientations. A camera angle of 23.5^0 is used. A good accuracy in the section profiles when compared to the exact profile is observed for both the sections and orientations.

The next Fig. 5.10 shows plots for two different sections, Y0 and X0, for the same concave profile plotted versus the position px. The sections are plotted for three different camera angles. The plots show a very good accuracy for the both the sections for varying camera angles. The maximum error in the profiles leaving the edges are 0.1788 mm (Y0) and 0.08884 mm (X0) for 23.5^0, 0.2372 mm (Y0) and 0.1126 mm (X0) for 15^0 and 0.2858 mm (Y0) and 0.08254 mm (X0) for 5^0. The next lens profile studied is a spherical convex lens profile of focal length 300 mm. The sections, X0 and Y0, for this profile for a camera angle of 15^0 is plotted versus px in Fig. 5.11. Again the method very accurately captures the interface shape and moreover there is no difference in the interface reconstruction for both the sections even though they have different light ray incidence angles. The maximum error in the profiles leaving the edges are 0.113 mm for section X0 and 0.1378 mm for section Y0. Here again a sub millimeter precision is achieved. The two profiles studied have a wavelength of about 50 mm, amplitude of about 2 mm, maximum slope of about 8^0 and mean interface height of about 5 mm. Hence, from the two lens interface reconstruction studies, it can be concluded that the Stereo-PIV-SS technique can find the interface profile with sub millimeter precision for cases with a combination of low interface slopes, high wavelengths, low amplitudes and

mean interface height for any orientation of the interface.

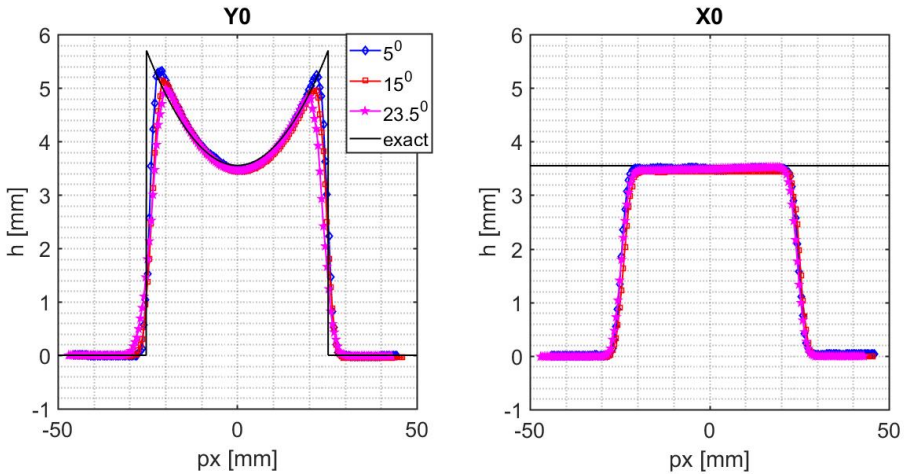

Figure 5.10: The sections, X0 and Y0, for the unidirectional spherical concave lens interface of focal length 300 mm, reconstructed using the Stereo-PIV-SS technique plotted versus px. The sections are plotted in two different subplots for orientation OrX and for varying camera angles. A good accuracy in the section profiles when compared to the exact profile is observed for both the sections and for different angles. The same legend applies for both the subplots.

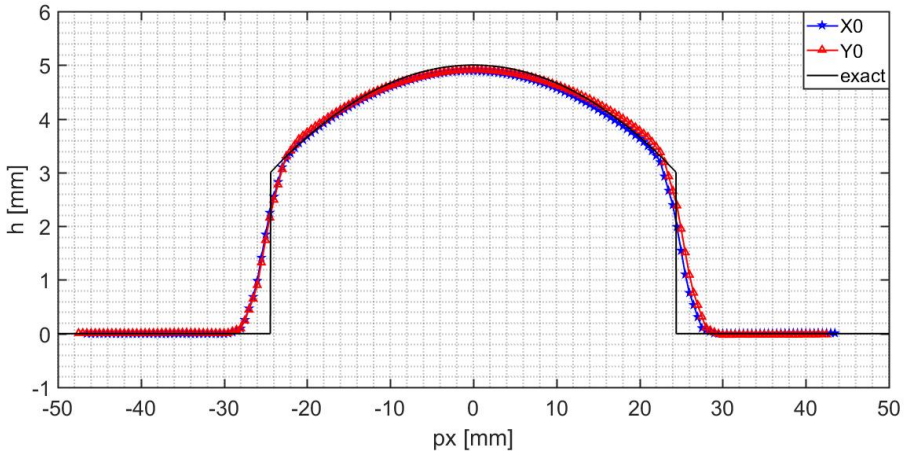

Figure 5.11: The sections, X0 and Y0, for the spherical convex lens interface of focal length 300 mm, reconstructed using the Stereo-PIV-SS technique plotted versus px. A camera angle of 15^0 is used. A good accuracy in the section profiles when compared to the exact profile is observed for both the sections.

The study with the solid interfaces show that there is a sub millimeter precision achieved for all cases except where the orientation plays a role. The minor mismatch with the exact solutions for theses cases are due to the error in machining of the interfaces, error in measurement of the interface profile for comparison, paraxial approximation error and also the fact that other parameters apart from dz are not included in the correlation for interface height.

5.3 Water wave experiments

The study experiments helped in getting a better understanding of the behaviour of the Stereo-PIV-SS technique applied to solid profiles. However, the technique is proposed to

be applied to an air cavity, where there is a water-air fluid interface. Therefore, experiments with water waves have been performed to asses the quality of reconstruction generated using this technique for an air-water interface. Two sets of water wave experiments are performed in a water tank shown in Fig. 5.12. First set is to analyze the wave ripples generated on the water surface due to water droplet impact. For the second set, a two point source wave generation mechanism was constructed to generate good quality waves and interference patterns for measurement. Since the water wave interface behavior is challenging to predict, the FS-SS technique is used to provide validation data for the Stereo-PIV-SS experiments. The FS-SS method was fine tuned for the current setup and also found to be very accurate in the study experiments.

5.3.1 Experimental Setup

The setup is similar to one used for the study experiments, as shown in Fig. 5.1. For the water wave generation setup, a water tank is placed at a distance h_a from the reference plane instead of the solid profiles and a wave generation mechanism is used to generate the water waves. Moreover, a third camera is used for simultaneous measurement with the FS-SS method. A camera angle of 10^0 is used for the Stereo-PIV-SS experiments and is within the range of the angles successfully studied in the study experiments. The water tank is 80 mm high and has an end to end cross section of 250 x 500 mm^2. The water tank is made of glass plates of 5 mm thickness. Sponge wedges are glued onto the inner walls of the tank as shown in the setup picture in Appendix C. These wedges help in avoiding any reflections that could disturb the original flow behaviour. The setup used to generate the waves is described as follows.

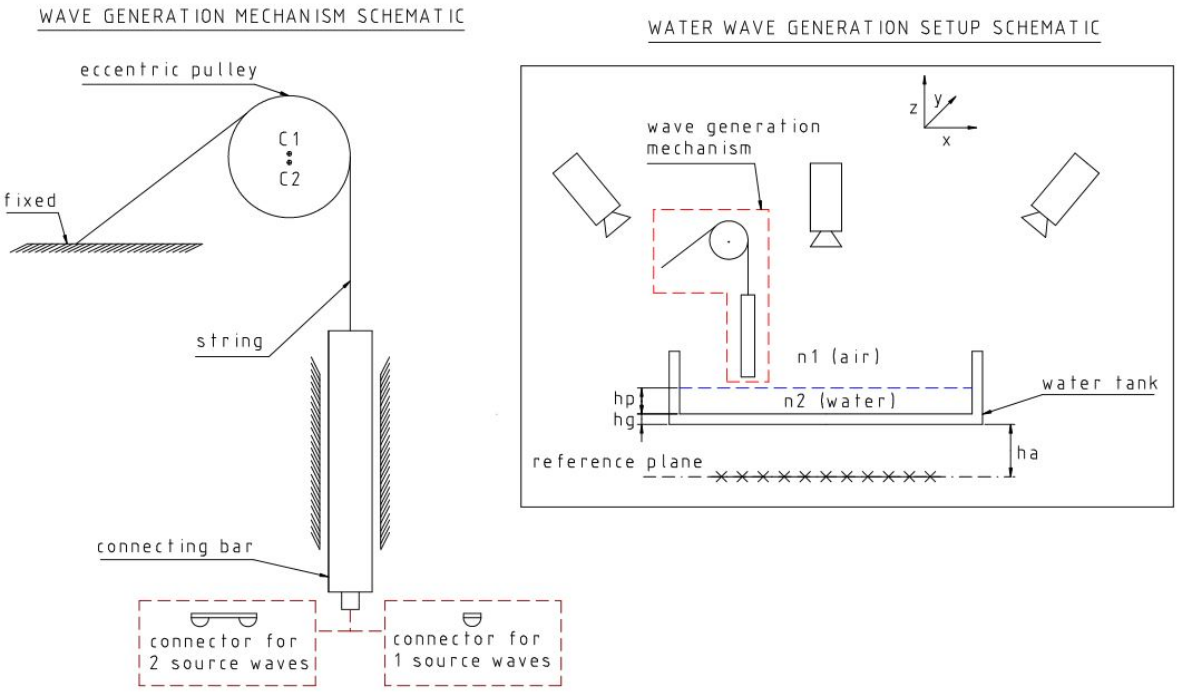

Figure 5.12: The figure to the left shows the schematic of the wave generator mechanism. A string fixed at one end is passed around the eccentric pulley groove and connected to the connecting bar. Due to the eccentricity of the pulley the connecting bar oscillates with every rotation and the connector, one or two source, impacts the water surface to generate the waves. The figure to the right shows the schematic of the water wave generation setup. The wave generation mechanism is placed just about the water tank with the tip of the connector touching the water surface. The other part of the setup is same as shown in Fig. 5.1.

Water wave generation

The first set of waves are generated due to a water droplet impacting the water surface. The syringe shown in Appendix C was used for generating the droplets. The droplets are released by the syringe tip from heights ranging from 25 mm to 50 mm above the water surface for varying water depths. The droplet diameter is approximately 3.5 mm. This was measured in pixels from the droplet images just before impact, and converting it to mm units using the mm-pixel relation. The droplet impact is expected to generate circular wave packets with waves of variable amplitudes and interface slopes. These circular wave patterns generated will help in testing the orientation behaviour of the Stereo-PIV-SS technique.

For the next set of water wave experiments, it was aimed to generate simple but intricate and also controllable waves. Hence, one point source and two point source waves were selected to be generated. The one source waves are a constant series of circular waves generated at the point of impact with the wavelength directly related to the frequency of oscillation. The two source waves are two one source waves separated by a small distance interfering with each other. The interference gives rise to an intricate wave pattern which will help in testing the pattern capture ability of the Stereo-PIV-SS technique. A wave generation mechanism was designed as shown in Fig. 5.12 to generate these waves. A pulley with an eccentric hole drilled on the shaft, here called an eccentric pulley, is fitted onto the shaft of a variable frequency AC motor. A string fixed at one end is passed around the pulley groove and connected to a connecting bar. This bar is constrained to move only in one direction. Due to its eccentric center, the pulley starts behaving like a cam and transfers this eccentricity through the string to the connecting bar which starts oscillating in the z direction. The type of waves generated are controlled by the connector attached to the connecting bar. It is possible to generate one point and two point source waves with this setup by changing the connector as shown in Fig. 5.12. The connector tip touches the water surface and with each rotation impacts the water surface to generate the waves. Two different eccentric holes (C1 and C2) are drilled on the eccentric pulley at 1.3 mm and 0.7 mm from the center at the two ends, as shown in Fig. 5.12. Depending on which hole (C1 or C2) is connected to the motor shaft, the oscillation amplitude can be varied which can help in changing the wave amplitude. Moreover, the motor frequency can be controlled to change the oscillating frequency that directly changes the wave frequency and wavelength. Even though the setup is able to generate both one and two source waves, only the results of two point source waves are discussed in this study. This is because one source waves are similar to the circular waves generated for the water droplet impact experiment and two source waves have an intricate pattern shape that is a better test for the technique. Pictures of the setup are shown in Appendix C.

5.3.2 Experimental Procedure and post processing

The wave phenomena are captured by three different cameras simultaneously at any instant. Two of these cameras in a stereo configuration are used for the Stereo-PIV-SS technique and one camera in a vertical configuration is used for the FS-SS technique. As compared to the study experiments, dynamic interfaces are captured for the water wave experiments with a frame rate of 13.52 fps.

The Stereo-PIV-SS experimental procedure and post processing used for the water wave experiments is exactly the same as used for the study experiments, see Sec. 5.2.2. Only change is in the correlation factor used, which is changed due to a change in the medium, in this case water with a standard refractive index of 1.33. The impact of extra layers of glass and air of thickness h_g and h_a between the water and pattern (see Fig. 5.12) is not expected to change the results as this is taken into account in the calibration.

The experimental procedure for the FS-SS technique is exactly the same as mentioned in the Sec. 5.2.1. The still water image for a particular water depth is taken as the reference image. The second image is taken of the disturbed interface. The post processing step is also very similar to Sec. 5.2.1. The only difference is that a modified mean height, h_{pm}, is used in the

Eq. 2.1 instead of the water depth, h_p. This is done to take into account extra layers of air and glass in between the dot pattern and the water as compared to the study experiments, refer Fig. 5.12. The equation used to compute h_{pm}, which is given in [29], is as follows:

$$h_{pm} = h_p + \frac{n_2}{n_g} * h_g + \frac{n_2}{n_1} * h_a \tag{5.3}$$

Where, h_p is the water depth, n_2 is the refractive index of water taken as a standard value of 1.33, n_g is the refractive index of the tank glass taken as a standard value of 1.52, h_g is the glass thickness which was 5 mm for the setup, n_1 is the refractive index of air which is 1 and h_a is the height of the air layer which was 7.6 mm for the setup. Using this value of h_{pm} in Eq. 2.1 in place of h_p, the surface gradient, ∇h, is found. ∇h is integrated to give the interface profile about the mean interface. Adding the water depth h_p finally gives the absolute interface height profile.

To get an accurate value of the still water depth h_p used in the FS-SS method, the Stereo-PIV-SS method was used for water level measurement. The Stereo-PIV-SS method was found to be very accurate for the study experiments with the flat interface, see Sec. 5.2.2, and hence is expected to give a reliable measurement of the water depth value to be used in FS-SS post processing. Moreover, this will be a further validation for the applicability of Stereo-PIV-SS method for level measurement.

5.3.3 Results

Water droplet impact

The water droplet impact results are first analyzed using the FS-SS method. It was found in the FS-SS study experiments that the IW size selected had an impact on the amplitude and absolute height of the waves. Hence, a $\frac{IWsize}{wavelength}$ ratio of $\frac{36}{20}\ \frac{pixels}{mm}$ was prescribed as per the study experiments. The maximum wavelength observed for the water droplet impact images captured is about 15 mm and hence the ratio suggests an IW size of 27 pixels to be used. Hence, an IW size of 28 x 28 pixel^2 was selected. Moreover, the minimum IW size to generate a smooth reconstruction was also found to be 28 x 28 pixel^2. Fig. 5.13 shows a time series of the water wave profile reconstruction for a water droplet impact experiment. The still water depth for this case is 5.3 mm. The water droplet impact is considered to impact at T=0 s and the time instant after droplet impact is mentioned as the title in each subplot. The subplots show that the FS-SS technique can capture the wave profile very smoothly. Moreover, there is no noticeable effect of reflections seen from the side walls and hence the setup with the wedges selected is accurate enough to capture this wave phenomena.

Proceeding further, the FS-SS results are compared to the Stereo-PIV-SS results for the same conditions. First the section X0 is analyzed. An IW size of 36 x 36 pixel^2 was used for the Stereo-PIV-SS technique. A comparison of the section X0 for different instants after the droplet impact is shown in Fig. 5.14. The title for each subplot shows the time instant after droplet impact at which the images were captured. The subplots indicate a relatively good match in absolute height, amplitude and wavelength for the Stereo-PIV-SS technique when compared to the FS-SS technique. A sub millimeter precision is observed. This is a good accuracy considering the fact that there are sub millimeter errors in both the techniques and also the reference still water interface height used in the FS-SS reconstruction was computed using the Stereo-PIV-SS technique. This result is also a confirmation that the Stereo-PIV-SS technique can capture the flat interface height with high precision. Moreover, it is observed that the accuracy of the reconstruction gets better at later time instants after droplet impact since the waves are more damped with smaller interface slopes at that instant. This ascertains the fact that the Stereo-PIV-SS technique is interface slope sensitive, as was also observed for the sloped interface results in Chapter 4, 4.8. Also it is observed that the technique can capture the wave interface with reasonable accuracy for a section of

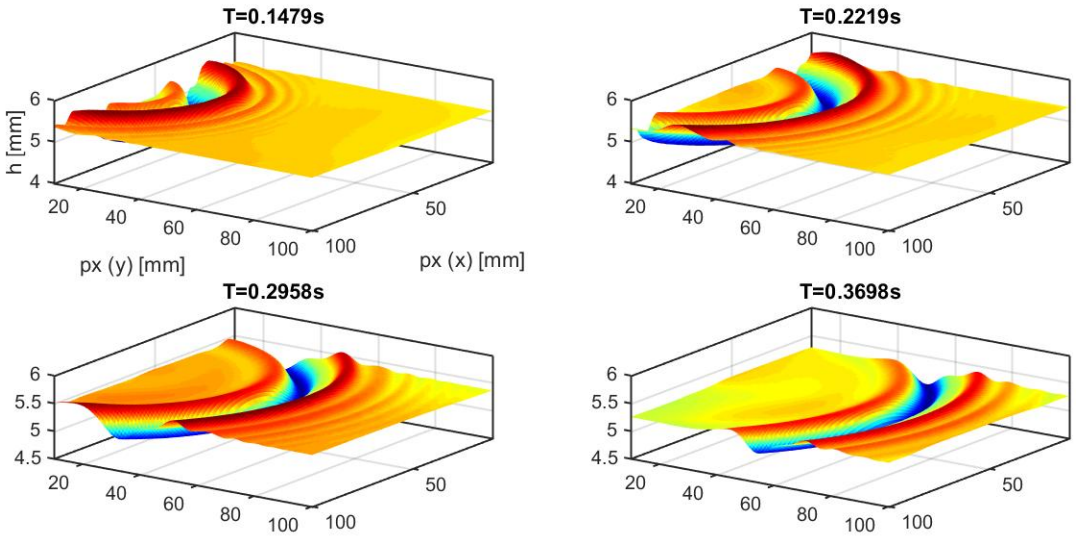

Figure 5.13: Time series plots of the wave interface reconstructed using the FS-SS technique after water droplet impact on a liquid water surface is shown for a water depth of 5.3 mm. The time instant of image capture after the water droplet impact is shown in the title. All subplots are for the interface height plotted in the FOV and have the same parameters and units shown in the first subplot. A smooth reconstructed wave profile is observed from the subplots.

the reconstructed profile taken in a plane orthogonal to the camera direction. This is similar to what was observed for the Plexiglas wave interface placed in the OrY orientation, as shown in Fig. 5.6.

Although the section X0 matched well for both the techniques, there is an orientation dependence seen in the other section planes for the Stereo-PIV-SS technique as also seen in the study experiments. Fig. 5.15 shows three subplots which are for the wave reconstruction using the Stereo-PIV-SS technique for a time instant of 0.2219 s after water droplet impact. The subplot (a) is a 3D plot for the wave interface height plotted in the FOV. The subplot clearly shows an unusually high change in the amplitude along the circumference of the wave. This change is parabolic in nature and changes with the wave section orientation with respect to the cameras. This confirms the fact that the reconstruction is erroneous for all other planes apart from the section X0 plane for this range of interface slopes, wavelengths, amplitudes and water depths. The subplot (b) is a contour map of the same wave. The contour map also shows an amplitude variation along the wave circumference. Additionally, it is seen that all the points connecting a single wave trough or crest do not fall on one circle. A circular wave profile expected in the contour plot, is not observed. The subplot (c) is a plot for the interface height versus the position px for the section Y0 of the same wave. A comparison of the section Y0 is shown for both the FS-SS and the Stereo-PIV-SS method. This figure confirms a much larger and erroneous amplitude seen for the Stereo-PIV-SS method as compared to the more reliable result using the FS-SS method. This behaviour is similar to what was observed for the Plexiglas wave interface placed in the OrX orientation, as shown in Fig. 5.7. Same as observed for the Plexiglas interface in OrX orientation, the mean interface height is captured with sum millimeter precision for the droplet impact experiment. These observations prove that the Stereo-PIV-SS technique is highly orientation dependent and is impacted highly by the interface slope in the camera direction.

The droplet impact results were analyzed for more water depths ranging from 10 mm to 60 mm. A similar behaviour for all the profiles was found for the Stereo-PIV-SS technique until 10 mm water depth and slowly the error in also section X0 started to increase with depth. The reconstruction for all depths 35 mm and above did not give a smooth reconstruction pointing at the fact that there exists a maximum pattern surface distance this technique can smoothly measure. Hence, there exists a limiting condition for the water depth for this

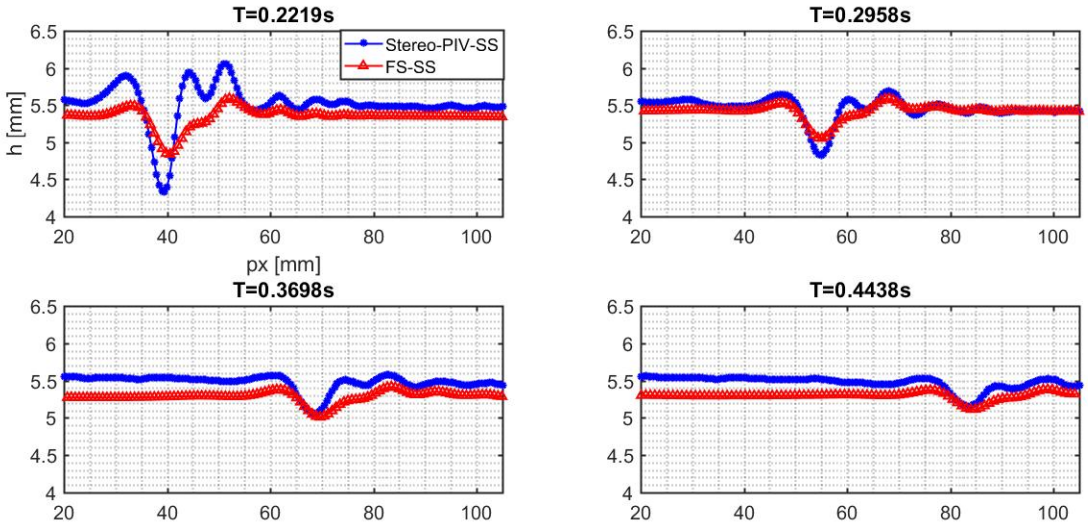

Figure 5.14: The section X0 plots of the wave interface reconstructed after water droplet impact on a water surface is compared for both the FS-SS and Stereo-PIV-SS technique for a water depth of 5.3 mm. The time instant of the reconstruction after the water droplet impact is shown in the title. All subplots are for the same parameters and units shown in the first subplot. The comparison shows a sub millimeter precision for the Stereo-PIV-SS technique with the accuracy getting better for more damped waves.

technique as also seen for the FS-SS technique [29].

Two point source waves

The next set of experiments were conducted for two point source waves using the wave generation mechanism. A pulley eccentricity of 0.7 mm is selected which corresponds to a 1.4 mm oscillation amplitude for generating the waves. Preliminary wave reconstruction using FS-SS were analyzed for different frequencies of wave generation ranging from 10 hz to 40 hz. It was found that a 40 hz frequency provided a wave interference pattern with enough crests and troughs for a good quality pattern formation in the FOV. A water depth of 5.3 mm was selected considering a good accuracy found for section X0 using Stereo-PIV-SS during the water droplet impact experiments. Since the reconstruction using dz for the water droplet impact experiment gave erroneous amplitude values, contour plots are compared for the two point source experiments set to compare how accurately the contour pattern can be captured by this technique. Moreover, dx and dz are also plotted to check their behaviour. A series of contour plots for the reconstruction of a two point source wave pattern for 40 hz frequency and water depth of 5.3 mm is shown in Fig. 5.16. The parameter studied for each contour plot is mentioned in each subplot title. The FS-SS interface height contour plot in the FOV shows a smooth and regular pattern of crests and troughs formed by wave interference. It is also observed that the waves get damped when moving away from the sources due to energy loss. Also no noticeable reflections from the side walls are seen and hence the setup is capable of studying such wave phenomena. The contour plots for dz and dx show that the pattern does not match well with the FS-SS technique and hence is not a good parameter for pattern capture. The dy pseudo vector contour plot can capture the wave pattern behaviour relatively accurately. Only observation is that there is a minor shift in the complete pattern of approximately 1 mm in the x direction and 6 mm in the y direction when comparing the plot to FS-SS in the FOV. In any case, when only comparing the pattern shape, there is only a maximum of 2 mm error for either the x or y coordinate position for the crest and troughs of the pattern. The error value corresponds to only a 2 % relative error when comparing to the FOV size. Thus the dy pseudo vector is a good parameter to capture complex pattern shapes using the Stereo-PIV-SS technique. Hence, further studies with this technique need to take

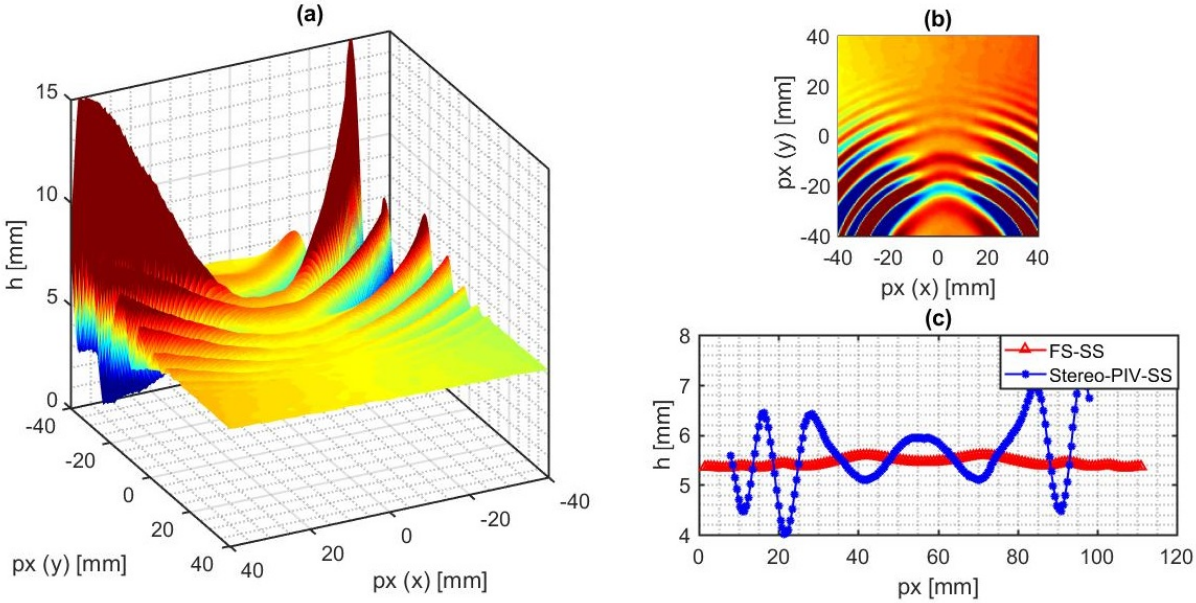

Figure 5.15: Three subplots are shown for a reconstruction of the wave 0.2219 s after water droplet impact on a water surface for a water depth of 5.3 mm. Subplot (a) shows a 3D reconstruction of the interface height in the FOV. A parabolic variation of the height along the circumference is observed. Subplot (b) is a contour plot of the interface and shows a parabolic variation along the circumference and also the waves are not on a circle when following any crests or troughs. In subplot (c) the section Y0 is plotted for the FS-SS and Stereo-PIV-SS technique. Very high and erroneous amplitudes are seen for the Stereo-PIV-SS technique as compared to the reliable FS-SS technique.

into account the influence of dy and also dx along with dz. In addition to this, a parameter for wave orientation also needs to defined as it also has an important influence on the reconstruction. Additionally, the mean interface height is captured accurately by taking the mean of the interface height computed using dz, proving that dz play a vital role in computing the absolute height.

5.4 Explanation for amplitude reversal due to orientation dependence for Stereo-PIV-SS

It was observed for the Stereo-PIV-SS reconstruction with the Plexiglas wave interface oriented in the OrX direction, see Sec. 5.2.2 and Fig. 5.7, that there was an amplitude reversal and erroneous amplitude magnitude as compared to the exact profile. A similar behaviour was observed for the water droplet impact experiment (see Sec. 5.3.3 and Fig. 5.15). But, the same reversal and erroneous amplitude was not observed for the two lens interfaces studied, see Sec. 5.2.2, Fig. 5.9 and Fig. 5.11. The lens profile has a higher wavelength, more gradual slope (θ), and lower mean interface height (h_p) as compared to the Plexiglas profile. This indicates that there is some criteria for an amplitude reversal which is a combination of these parameters. To find this criteria, a simplified analytical problem shall be solved.

To explain amplitude reversal a representation of a crest and trough is needed. For this, the sloped interface analytical solutions found in Chapter 4 shall be extended to also include a mean interface height. A ray tracing diagram to illustrate this is shown in Fig. 5.17, which was drawn in LibreCAD. There are two sub figures shown with cameras viewing the point of intersection of the optical axis with the reference plane, namely R and S. The crest and trough are considered as a triangular interface as only one slope is encountered by the rays for viewing the points R and S. Moreover, only rays from one side of the interface is shown since the other side is symmetric. The width of the interface, L_λ, is a function of the wave length and is same for both the cases. Also both the interfaces have the same magnitude

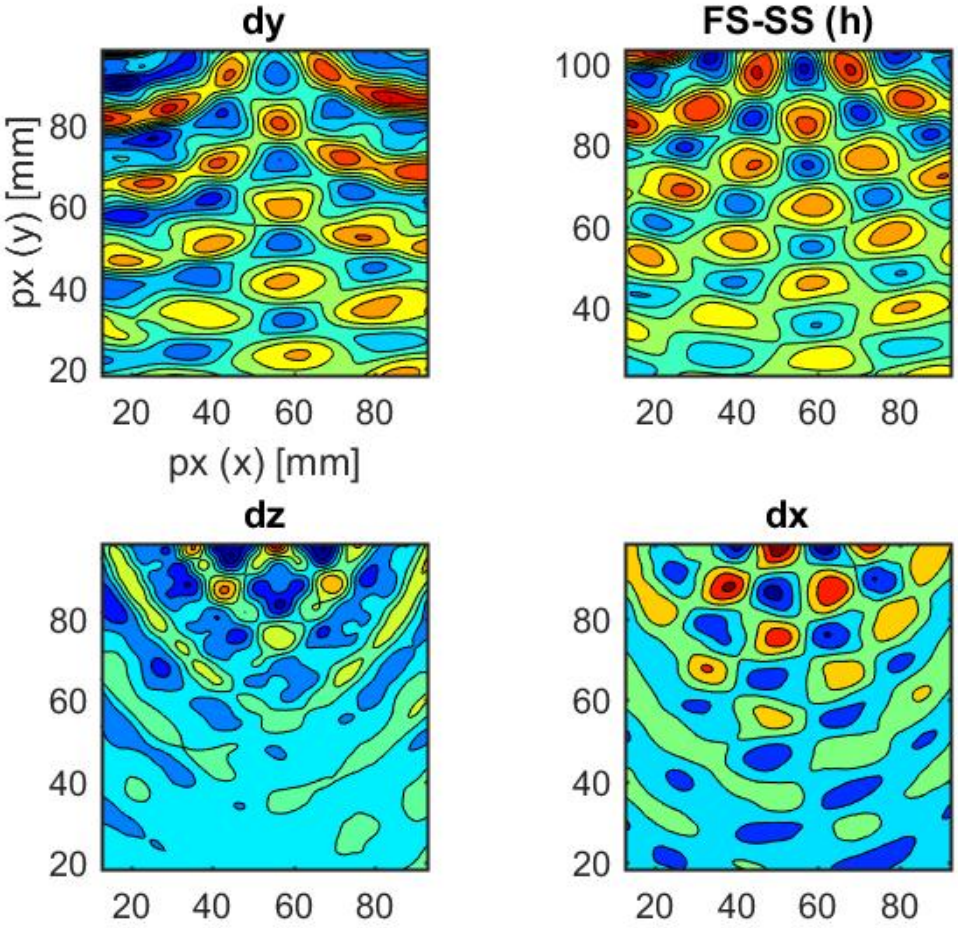

Figure 5.16: Four contour subplots are shown for the reconstruction of the two point source wave generated for a water depth of 5.3 mm and an oscillation frequency of 40 hz. All subplots are plotted in the FOV and have the same units shown in the first subplot. The parameter studied is mentioned as a title for each subplot. The x and y parameters and units shown in the first subplot hold for all subplots. The FS-SS contour plot for the reconstructed interface height predicts well the expected pattern behaviour and is used as a reference for comparison. The dz and dx plots are unable to capture the wave pattern accurately. While dy can accurately capture the pattern shape although there is a minor shift of the complete pattern in the x and y directions compared to FS-SS in the FOV.

interface slope, θ, mean interface height h_p and the same camera angle α. The paraxial approximation is applied and hence all rays coming from the camera are parallel and at an angle α.

In Fig. 5.17(a), the ray travelling from point R refracts at the positive slope interface representing a crest to reach the cameras. The intersection point on the interface is at a distance of x_a from the optical axis. The ray incidence angle is $i_{i,a}$ and the ray refraction angle is $i_{r,a}$. The rays from the camera when extended intersects the optical axis and the y intercept is the dz pseudo vector, here named as dz_a. Fig. 5.17(b) is similar to Fig. 5.17(a), except that the camera is now capturing the point S through a negative slope interface representing a trough. For this case the rays from the camera when extended intersect the optical axis and the y intercept is dz_b. Also the rays intersect the interface at a distance of x_b from the optical axis. Fig. 5.17 is drawn to scale and an amplitude reversal can be seen since dz_b is greater than dz_a. The equations that describe this geometry are as follows:

Here, $i_{i,a} = \alpha - \theta$ and $i_{i,b} = \alpha + \theta$. Applying Snell's law using Eq. 4.3, the angles of refraction,

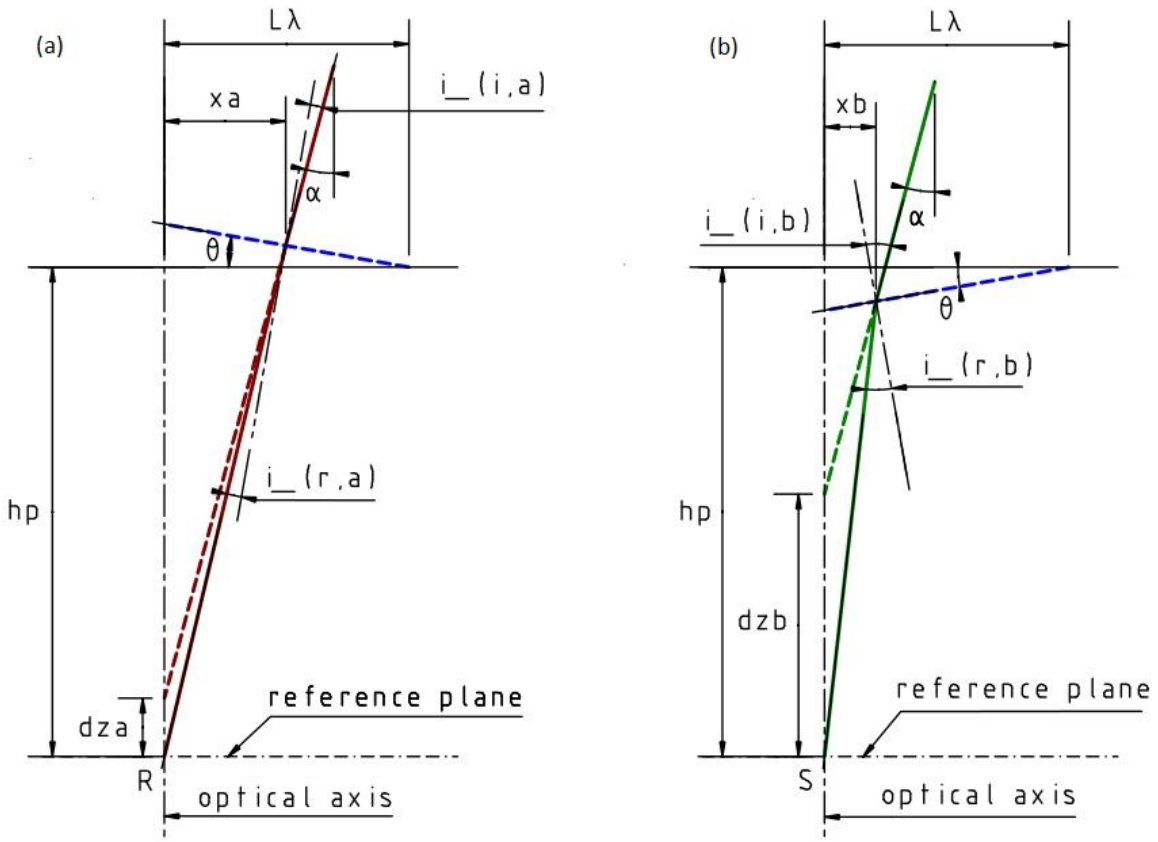

Figure 5.17: The 2D ray tracing diagram for the camera viewing points R and S through an interface having a mean interface height plus a crest or trough is shown figures (a) and (b) respectively. The crest and troughs are represented as triangular interfaces and only one half of the interface is shown as the behaviour is symmetric. Bother interfaces have the same mean interface height, h_p, and camera angle α. The interface in (a) has a positive slope and in (b) has a negative slope, both of magnitude θ. The rays are refracted at the interface with incidence angle of i_i and refraction angle of i_r. The rays from the camera when extended intersect the optical axis and the y intercept is dz_a is for the crest and dz_b for the trough.

$i_{r,a}$ and $i_{r,b}$, are found. Further proceeding to find the intersection of the rays with interface, x_a and x_b,

$$\frac{(L_\lambda - x_a) * \tan\theta + h_p}{x_a} = \cot(i_{r,a} + \theta)$$

Therefore,

$$x_a = \frac{L_\lambda * \tan\theta + h_p}{\cot(i_{r,a} + \theta) + \tan\theta} \tag{5.4}$$

In a similar manner x_b for the negative sloped interface can be determined and is as follows:

$$x_b = \frac{h_p - L_\lambda * \tan\theta}{\cot(i_{r,b} + \theta) + \tan\theta} \tag{5.5}$$

The slope of the rays from the camera for both Fig. 5.8 (a) and (b) is $\tan(\frac{\pi}{2} - \alpha)$. Using known values and the values of x_a and x_b from Eq. 5.4 and Eq. 5.5, the line equation for the camera rays is found. Solving for the y intercept of the line equations, the values of dz_a and dz_b are found which are as follows:

$$dz_a = h_p + (L_\lambda - x_a) * \tan\theta - \tan(\frac{\pi}{2} - \alpha) * x_a \tag{5.6}$$

$$dz_b = h_p - (L_\lambda - x_b) * \tan\theta - \tan(\frac{\pi}{2} - \alpha) * x_b \tag{5.7}$$

Using the values of dz_a and dz_b found in Eq. 5.6 and Eq. 5.7 the condition for amplitude reversal, which is when dz_b becomes greater than dz_a, is found. The variation of dz_a and dz_b with respect to h_p is shown in Fig. 5.18 for L_λ=5 mm, $\alpha = 10^0$ and two different θ, $\theta = 2^0$ and $\theta = 8^0$. The values of parameters and their ranges are chosen for the Plexiglas wave profile. L_λ is chosen as $1/4^{th}$ the wavelength of 20 mm for the Plexiglas wave profile to represent one side of the crest or trough. The camera angle $\alpha = 10^0$ is chosen within range of the study experiments that were conducted and the θ values are chosen to be less than the maximum slope that can be encountered for this profile which is 8.93^0. Fig. 5.18 shows a reversal of dz value after a limiting h_p value for both θ. This is more clearly seen in the zoomed in view. This shows that amplitude reversal occurs above a limiting h_p value. Moreover, there is amplitude reversal as was observed for the case of the Plexiglas profile when h_p=20 mm, and hence the plot is consistent with this experimental observation. Also θ does not have any significant impact on the limiting value of h_p for amplitude reversal.

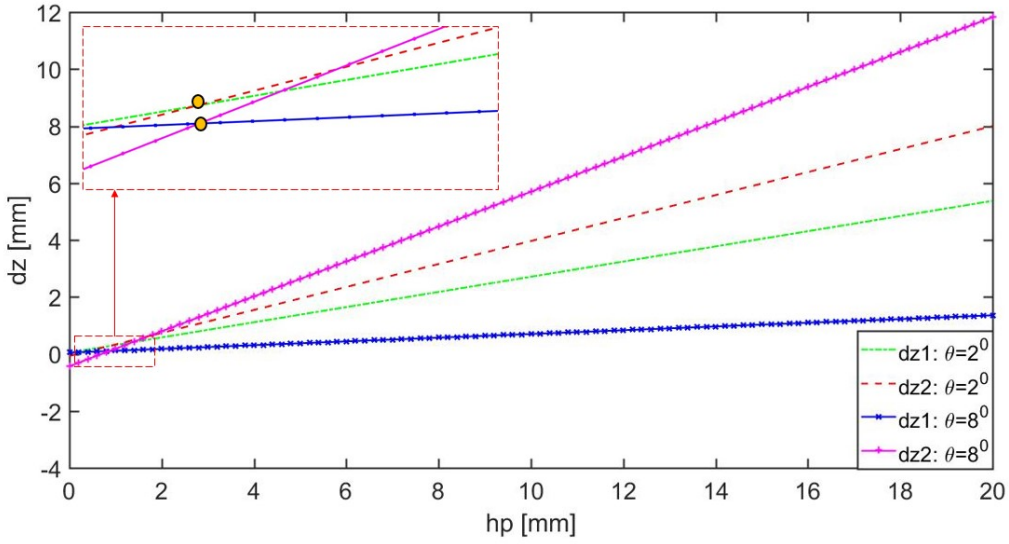

Figure 5.18: dz_a and dz_b pseudo vectors are plotted versus the mean interface height h_p for the interfaces representing the crest and trough respectively. The results are plotted for two interface slopes, $\theta = 2^0$ and $\theta = 8^0$. The values of parameters and their ranges are chosen for the Plexiglas wave profile. The plot shows a limiting value of h_p for amplitude reversal which is not impacted much by a change in θ. There is amplitude reversal seen at h_p=20 mm which was also observed for the Plexiglas wave experiments for wave oriented in the OrX direction.

The variation of dz_a and dz_b with respect to L_λ is shown in Fig. 5.19 for h_p=3.55 mm and for two different α and θ. The values of parameters and their ranges are chosen for the lens profiles studied. Fig. 5.19 shows an amplitude reversal for values below a limiting L_λ. For the lens interface no amplitude reversal was observed as the L_λ=25 mm, which is above this limiting value. Hence, the result is consistent with what was observed in experiments. As also seen in Fig. 5.18, a change in θ does not have any significant impact on the limiting value of L_λ for amplitude reversal. However, for increasing α the limiting value of L_λ is reduced.

These observations prove that the amplitude reversal seen in experimental results was not an artefact. Eq. 5.6 and Eq. 5.7 provide a criteria for finding the conditions for amplitude reversal for a particular setup.

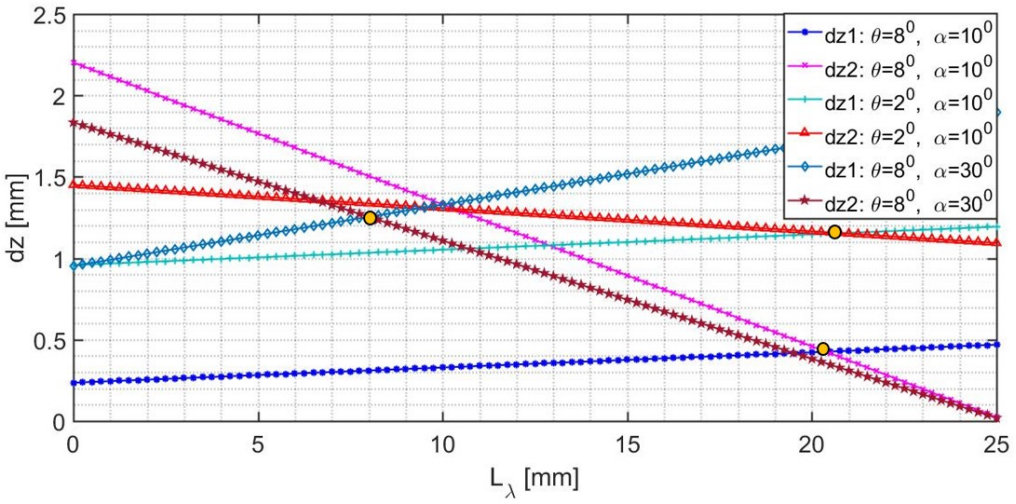

Figure 5.19: dz_a and dz_b pseudo vectors are plotted versus the interface width of L_λ for the interfaces representing the crest and trough respectively. The results are plotted for combinations of two interface slopes, $\theta = 2^0$ and $\theta = 8^0$ and two camera angles $\alpha = 10^0$ and $\alpha = 30^0$. The plot shows a limiting value of L_λ below which there is an amplitude reversal. This reversal point is not impacted much by a change in θ but has a significant impact for a change in α. There is no amplitude reversal seen at L_λ=25 mm which was also observed for the two lens experiments.

Chapter 6

Conclusions and Recommendations

6.1 Conclusions

This research has been conducted with a goal to develop a novel experimental technique for measuring the interface of an air cavity. Although there is still some ground to cover, several crucial conclusions can be drawn from this work which are as follows:

- A comprehensive literature study on visible light based water free surface reconstruction techniques was conducted. The study shows that the existing techniques have limitations when applied to an air cavity in the proposed cavitation tunnel setup.
- Two novel ideas for free surface measurement are proposed: Stereo-PIV-SS and Stereo-FS-SS. The Stereo-PIV-SS technique uses a combination of concepts from synthetic Schlieren imaging and Stereo PIV. The Stereo-FS-SS technique involves the modification of the FS-SS technique by using a stereo camera configuration and the reconstruction is computed without using any still interface reference image. The preliminary analysis with the Stereo-FS-SS technique highlighted several limitations of the technique as mentioned in Chapter 3, Sec. 3.2.1. Therefore, it was decided to proceed with a detailed investigation of the more promising Stereo-PIV-SS technique.
- An analytical framework is set up for further ray tracing studies with the Stereo-PIV-SS technique. The study with a flat interface showed a strong correlation between dz and the interface height. However, a weak correlation is observed for dx. A linear relation is derived by applying approximations for relating dz to the flat interface height. The study with a sloped interface also showed a linear relation of dz with interface slope for a slope value less than 10^0. The dz relation becomes nonlinear and dx is observed to have a strong correlation for higher values of interface slopes. Moreover, it is observed that the correlation found between dz and interface height in Chapter 4, Eq. 4.6 gives an accurate value of interface height from dz for low interface slopes. This result is applied in the experiments chapter for the interface height correlation.
- Experiments for the Stereo-PIV-SS technique were conducted on solid profiles and water waves. The studies show that the Stereo-PIV-SS technique helps in predicting the flat interface height with sub millimeter precision for a known refractive index of the media and camera angle. Hence, a simple non-intrusive method of level measurement is developed. The interface heights were tested in the range of 5 mm to 60 mm. The Stereo-PIV-SS technique helps in detecting uniform changes in the interface height, which is a limitation of the FS-SS technique as also mentioned in [29]. Moreover, dz helps in finding the mean interface height of any wave, independent of the wave direction.

- Solid and water wave profiles having wavelengths of the order of 1 cm and amplitudes of the order of 1 mm were tested. The Stereo-PIV-SS technique is able to capture the wave interface profile with sub millimeter precision for cases with weak slopes, amplitudes and low mean interface height as was observed for both the lens interface reconstruction experiments. For relatively large wave slopes, amplitudes and low wavelengths, the orientation and other pseudo vectors also start impacting the reconstruction. This was observed for the Plexiglas wave profile, where the reconstruction gave accurate results with sub millimeter precision for the OrY direction, however, erroneous amplitudes and an amplitude reversal was observed for the OrX direction. A similar behaviour was seen in both the water wave experiments. For these cases, only dz cannot be used for interface height correlation. Hence, $h = f(dx, dy, dz, orientation)$. This reconstruction behaviour can be characterized only after understanding more about the interplay between different parameters. As a starting point, a simple criteria is found to check for an amplitude reversal for a given setup. This criteria is largely dependent on the mean interface height (h_p) and the wave width (L_λ), which is a function of the wavelength. The criteria shows that the limiting values of h_p and L_λ can be changed by changing the camera angles. For any given setup, this criteria can be used to provide an initial estimate for avoiding amplitude reversal.

- The dy pseudo vector can be used to find the pattern shape for high slope intricate wave patterns as seen from the two source water wave experiments. For the same experiment, dz and dx gave erroneous pattern shapes. Hence, dy is a promising parameter to study the pattern behaviour of air cavities.

- The main limitations for this method are that the technique is highly dependent on wave orientation and is currently applicable only to a small range of wave parameters. Moreover, the technique involves the interplay of several parameters, like the pseudo vectors (dx, dy, dz), mean interface height (h_p), the wave width (L_λ) and orientation. This makes it difficult to find a universal correlation for the interface height.

- An important advantage of the Stereo-PIV-SS technique is that it is easy to use. Moreover, it has a low computational cost and low infrastructure cost such as cost of software licenses or special cameras and equipment. This is because the technique can be implemented by using a standard PIV setting.

- A simple setup was designed and constructed based on an eccentric pulley for generating small amplitude, one and two source waves in a tank.

- The in-house ray tracing code output was tested for the Stereo-PIV-SS and the FS-SS techniques. The code is able to generate accurate data comparable to experiments for a vertical camera configuration as used in the FS-SS technique. However, the code is not able to capture the complete behaviour for a stereo camera configuration as used in the Stereo-PIV-SS technique.

6.2 Recommendations

This study has laid a strong foundation for further research on air cavity interface measurement. The recommendations for future work are as follows:

- Apart from the sloped and flat interface analytical studies, an additional study to understand a triangular interface can be carried out. For this study, the rays coming from a point viewed on the object plane could refract either from the same side like a sloped interface, or from two different sloped sides before reaching the cameras. This needs to be studied by including a mean interface height. A starting point can be to use the findings from the amplitude reversal criteria mentioned in the Chapter 5.

- The Ray tracing code introduced in Chapter 2 was studied and fine tuned only for a few cases, results are shown in Appendix B. Further work can be done with this code to generate more reliable synthetic experimental data with validation, especially with a stereo camera configuration. This can help in testing various configurations and wave shapes that are not possible with a real experiment. It can also help in checking the impact of introducing an error into the system.
- The interface height was reconstructed using the dz pseudo vector in this study. However, it is observed that dx and dy also have a considering influence for changing wave orientations. Moreover, as seen in the analytical solutions Chapter 4, dx has an important influence above a slope of 10^0. Hence, for any wave orientation it is hypothesized that dz plays a role in finding the absolute mean interface height and dx and dy play a role in identifying the pattern shape and wave amplitudes. Moreover, the orientation parameter needs to be defined and included in the correlation as it has a big impact on the reconstruction. The interplay of all these parameters with interface height needs to be determined.
- The dy pseudo vector helps in predicting the pattern shapes with high accuracy for intricate wave patterns such as the two source waves that were studied. Hence, the dy pseudo vector should be computed for actual air cavities to determine the air cavity pattern shapes.
- It is expected that a criteria exists for a limiting mean interface height that can be measured accurately using the Stereo-PIV-SS technique. This could be similar to the one suggested in [29] for the FS-SS technique and requires further investigation.
- After gathering a large source of data from real experiments or from synthetic images, the possibility of using a machine learning approach can be investigated. This can help in finding a correlation between the relevant parameters and the interface height.
- The current analytical study was conducted in 2D. A 3D ray tracing program can be developed to further extend this study for the Stereo-PIV-SS technique. This would give a better idea of the behaviour of different pseudo vectors and other parameters like orientation from an analytical point of view, which in turn can help in finding a more universal correlation factor.

Appendix A

Images to demonstrate Stereopsis

Fig. A.1 and Fig. A.2 show images of the same object taken from two different viewpoints. When viewing cross-eyed, the brain fuses these images to generate a 3D view with depth perception. This generation of depth perception by the brain is referred to as stereopsis. To view cross-eyed, a sufficient distance, of about an arm length, has to be maintained between the image and eye. The left image has to be viewed with the right eye and the right image has to be viewed with the left eye. If properly focused, a third image will appear between that two images that is a virtual 3D view generated by the brain due to stereopsis. Using just these two images, anyone can view in 3D without any special equipment.

Figure A.1: Image of an insect taken from two different viewpoints for cross-eyed viewing. If properly viewed, a virtual 3D view of the insect should be visible to the viewer in between the two images. The image is taken from [40].

Figure A.2: Image is taken from two different viewpoints for cross-eyed viewing. If properly viewed, a virtual 3D view of the object should be visible to the viewer in between the two images. The image is taken from [41].

Appendix B

Synthetic data processing

A free surface reconstruction study was conducted for the Stereo-PIV-SS and FS-SS techniques by using synthetic images generated with the ray tracing code introduced in Chapter 2. The ultimate aim is to generate synthetic images that can be an accurate substitute for experimental images of the techniques. Such synthetic data can help in testing cases where experiments are not viable and also to generate large sets of data if necessary. Hence, the results for reconstructions generated using synthetic images as input are discussed in this Appendix.

B.1 Synthetic data generation

The synthetic images are generated using an in-house ray tracing code. The code takes input of a user defined interface, the camera configuration and also the random dot pattern or calibration pattern image to generate synthetic experimental images, see Fig. 2.5. In simple words, the code tries to capture what the camera would see in an actual experiment. The ray tracing algorithm traces the rays from each point on the reference pattern plane up to the camera image plane taking into account the refraction at the interface. The code generates all the calibration images and the synthetic Schlieren images for the experiment in one run.

B.2 Results

The synthetic images are generated for the same Plexiglas wave interface profile used in Chapter 5 and an additional circular wave profile having a mean interface height of 10 mm, wave amplitude of 0.5 mm and wavelength of 20 mm. The post processing step for each technique using synthetic images is exactly the same as for the experiments as mentioned in Chapter 5. To compensate for the fact that the FS-SS results generated in this study do not have a defined grid in the object plane, the reconstruction is displaced along the x and y directions to match the exact profile center. This does not influence the accuracy in profile capture and helps in proper comparison of profile shape captured by FS-SS. See Chapter 5 for terminology used in the experiments which shall also apply in this Appendix.

B.2.1 FS-SS

First, the Plexiglas wave interface oriented in both OrX and OrY directions are reconstructed using synthetic images. The mean profiles for the two orientations are shown in Fig. B.1. The mean profiles for reconstructions generated by using both experiments and synthetic data are plotted. The figure shows a good agreement of the reconstruction generated using synthetic

data with experiments. Moreover, a sub millimeter precision in amplitude, wavelength and absolute height as compared to the exact profile is observed.

Next the circular wave profile is reconstructed using synthetic images. Fig. B.2 shows a comparison of the reconstruction generated using synthetic images (a) and the exact profile (b). The comparison shows that the reconstruction captures the wave shape very smoothly. Moreover, a sub millimeter precision in amplitude, wavelength and absolute height as compared to the exact profile is observed.

The reconstruction study with synthetic data for the FS-SS technique proves that accurate synthetic images were generated by the ray tracing code. Hence, the code is capable of generating realistic synthetic images for the FS-SS technique.

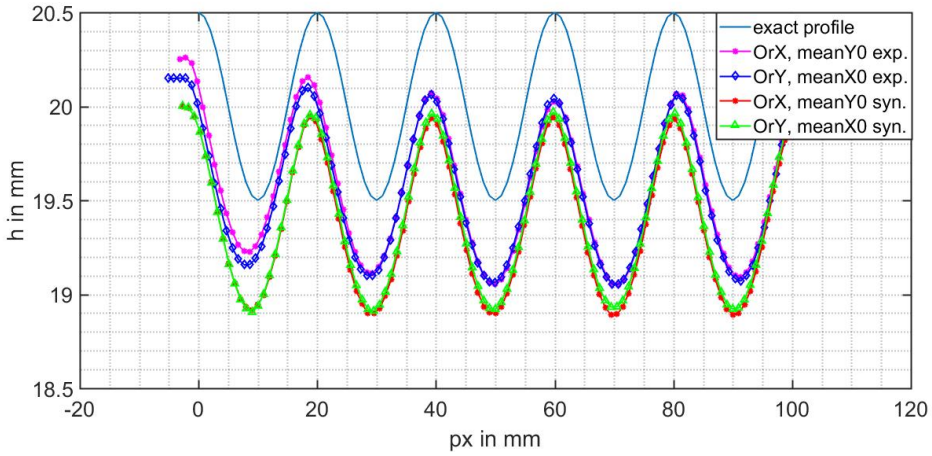

Figure B.1: Mean profiles of the Plexiglas wave profile oriented in two directions, OrX and OrY, reconstructed using the FS-SS technique. The interface height is plotted versus the position on the object plane, px, for experiments and synthetic images generated by the ray tracing code. The exact profile is also plotted for comparison. The figure shows a good accuracy in the absolute height, amplitude and wavelength captured by the FS-SS technique using synthetic images.

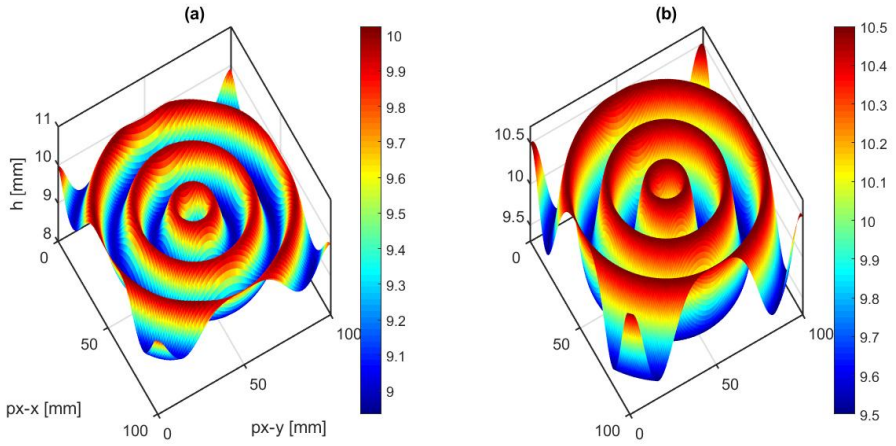

Figure B.2: 3D reconstruction of the circular wave profile reconstructed with the FS-SS technique using synthetic images as input is shown in Fig. (a). The exact profile is shown in Fig. (b). All subplots are for the same parameters and units shown in the first subplot. The interface height is plotted versus the object plane position. The comparison shows that the reconstruction captures the wave shape very smoothly for the FS-SS technique using synthetic images.

B.2.2 Stereo-PIV-SS

Fig. B.3 shows section X0 plotted for the reconstructed profile using both experiments and synthetic images for the Plexiglas wave interface oriented in the OrY direction. The reconstructions using experiments are plotted for different camera angles. A good match is observed for the reconstruction using synthetic data when compared to experiments. Moreover, a sub millimeter precision in amplitude, wavelength and absolute height as compared to the exact profile is observed.

Fig. B.4 shows section Y0 plotted for the reconstructed profile using both experiments and synthetic images for the Plexiglas wave interface oriented in the OrX direction. The reconstructions using experiments are plotted for different camera angles. For the reconstruction using experimental images an amplitude reversal and high erroneous amplitudes are observed, but for the synthetic images no amplitude reversal is seen although the amplitudes are high and erroneous. The amplitude observed was confirmed to be not an atrefact of experiments or processing and a criteria was also found to defined when reversal occurs in 5, Sec. 5.4. The exact reason why the synthetic images are not able to replicate the behaviour from experiments for this case is not clear yet and is an open question for further studies.

Fig. B.5 shows a comparison of the reconstruction generated using synthetic images (a) and the exact profile (b). The reconstructed profile shows a parabolic variation in amplitude along the circumference as also observed for the water droplet impact experiment in Chapter 5, Fig. 5.15, although the amplitudes are not as high as seen from the experiments. Moreover, all crests and troughs follow approximately the circumference as opposed to what was observed in the experiments where the points joining all crests or troughs were not on a circle, see Fig. 5.15. This difference in the reconstruction using synthetic images as compared to experiments for this case is not clear yet and is an open question for further studies.

From the study of synthetic data for the Stereo-PIV-SS technique, it is clear that there is still some modification required in the ray tracing code for it to replicate the exact behaviour as observed in Stereo-PIV-SS experiments. Hence, it can be concluded that the ray tracing code can generate accurate synthetic data for a vertical camera configuration as used in the FS-SS technique but is unable to generate accurate synthetic data for a camera at an angle like for a stereo camera configuration in the Stereo-PIV-SS technique.

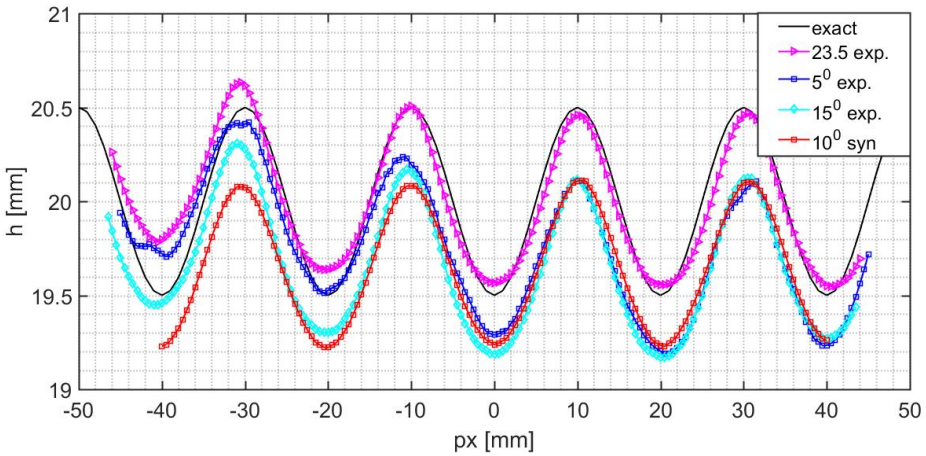

Figure B.3: Section X0 of the Plexiglas wave with orientation OrY, reconstructed using the Stereo-PIV-SS technique. The reconstruction generated using both experimental and synthetic images are plotted and compared to the exact profile. The experimental data is plotted for varying camera angles. The figure shows a good accuracy in the absolute height, amplitude and wavelength captured by the Stereo-PIV-SS technique using synthetic images.

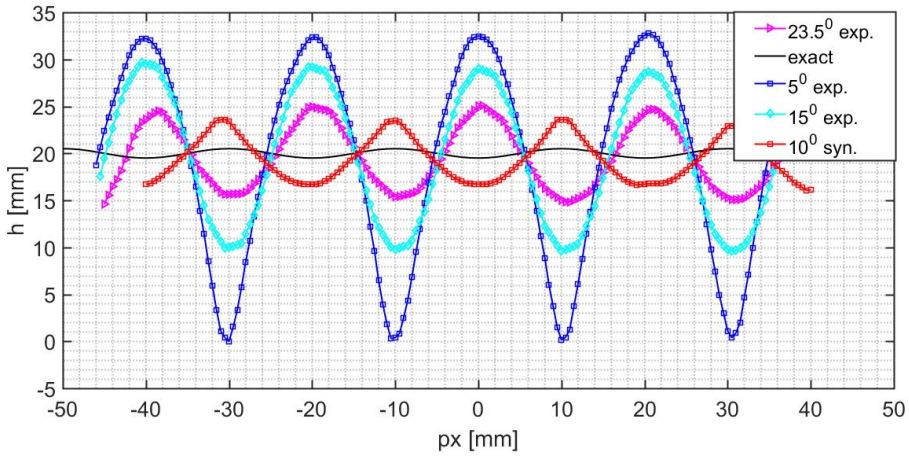

Figure B.4: Section Y0 of the Plexiglas wave with orientation OrX, reconstructed using the Stereo-PIV-SS technique. The reconstruction generated using both experimental and synthetic images are plotted and compared to the exact profile. The experimental results are plotted for varying camera angles. The experimental results show an amplitude reversal as compared to the exact profile but the synthetic data results do not show any amplitude reversal. Erroneous amplitudes are seen for both experiments and synthetic data but the synthetic data amplitude results are not comparable to experiments for similar angles.

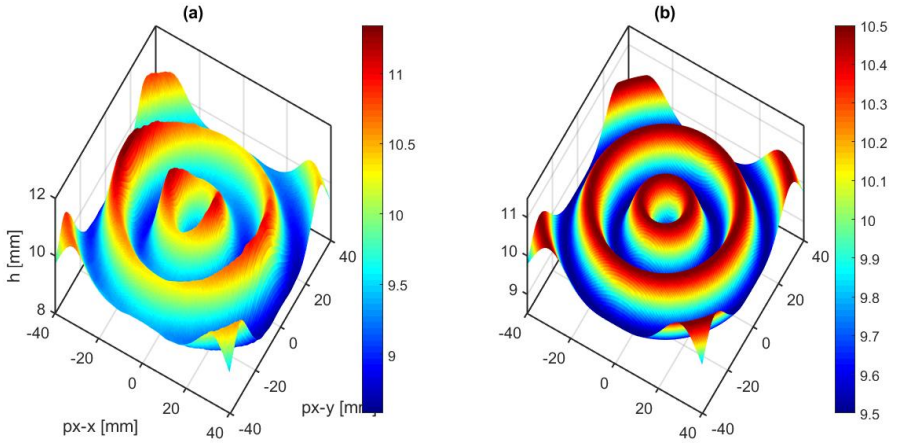

Figure B.5: 3D reconstruction of the circular wave profile reconstructed with the Stereo-PIV-SS technique using synthetic images as input is shown in Fig. (a). The exact profile is shown in Fig. (b). All subplots are for the same parameters and units shown in the first subplot. The interface height is plotted versus the object plane position. The comparison shows that the there is a parabolic variation in wave amplitude along the wave circumference. All points joining troughs or crests fall on a circle.

Appendix C

Experiment Images

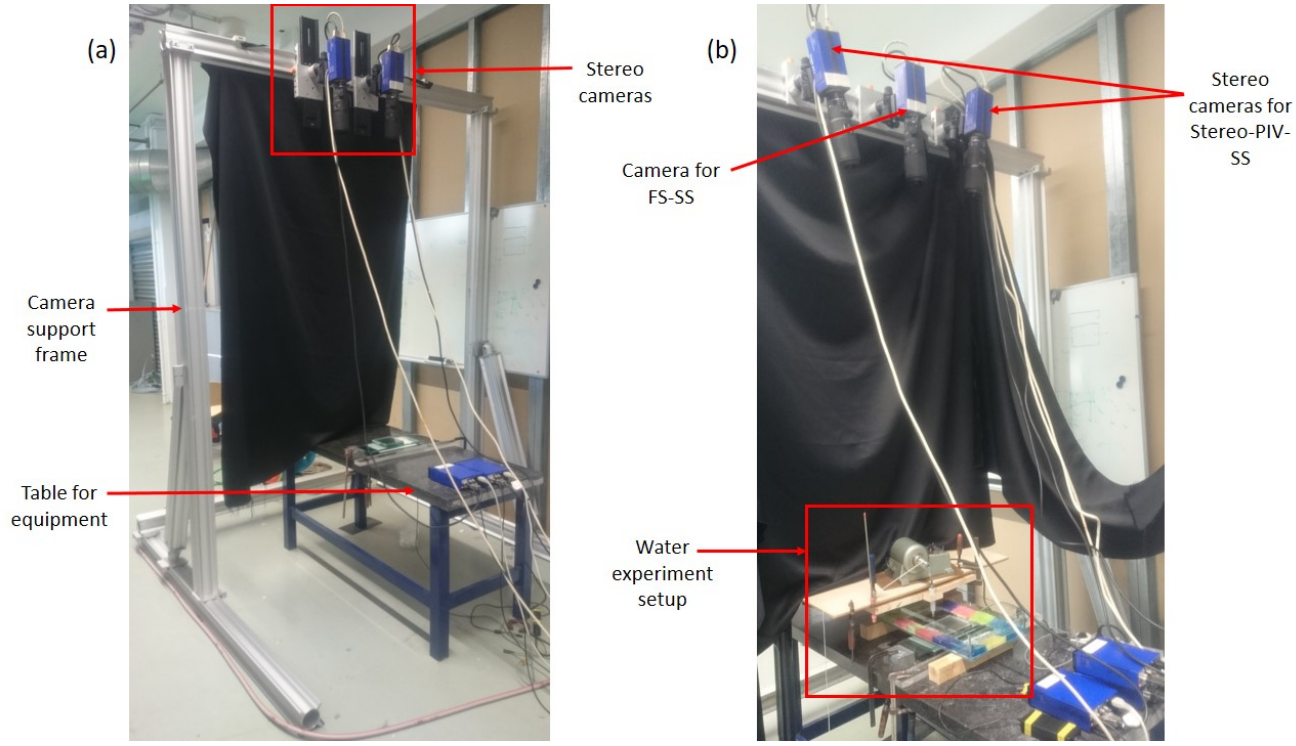

Figure C.1: Fig. (a) shows the setup used to perform Stereo-PIV-SS study experiments. Two cameras are placed in a stereo configuration supported by a frame. All other equipment are placed on the table. (b) shows the setup used to perform the water wave experiments. Three cameras are used, two in stereo configuration for Stereo-PIV-SS and one placed vertically for FS-SS. Other equipment for the water wave setup are paced on the table.

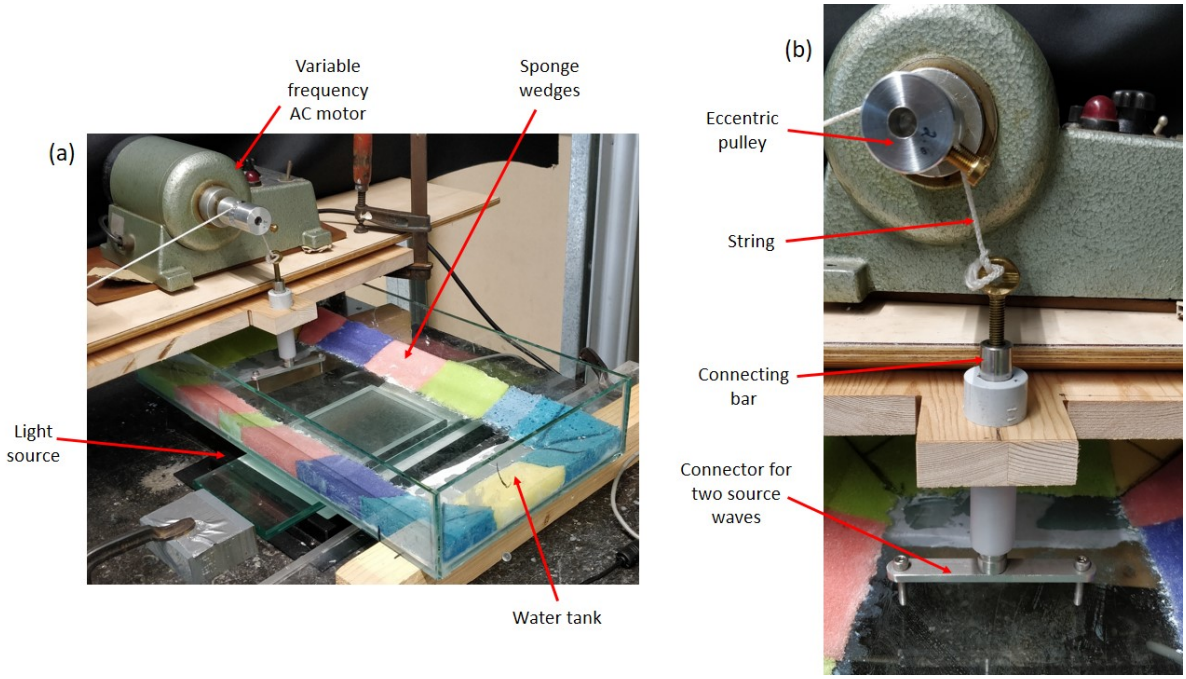

Figure C.2: (a) shows the water tank experimental setup without cameras. The water tank has sponge wedges glued onto the corners for water wave damping to avoid reflections. The light source and the dot pattern are placed below the tank. The wave generation mechanism powered by an AC motor is kept on a different platform to avoid vibrations from the motor transmitting to the water tank. (b) shows the wave generation mechanism. The eccentric pulley is connected to the motor shaft. A string passes through the pulley groove and is tied to the connecting bar. A two source connector is attached to the connecting bar which oscillates with every turn of the motor.

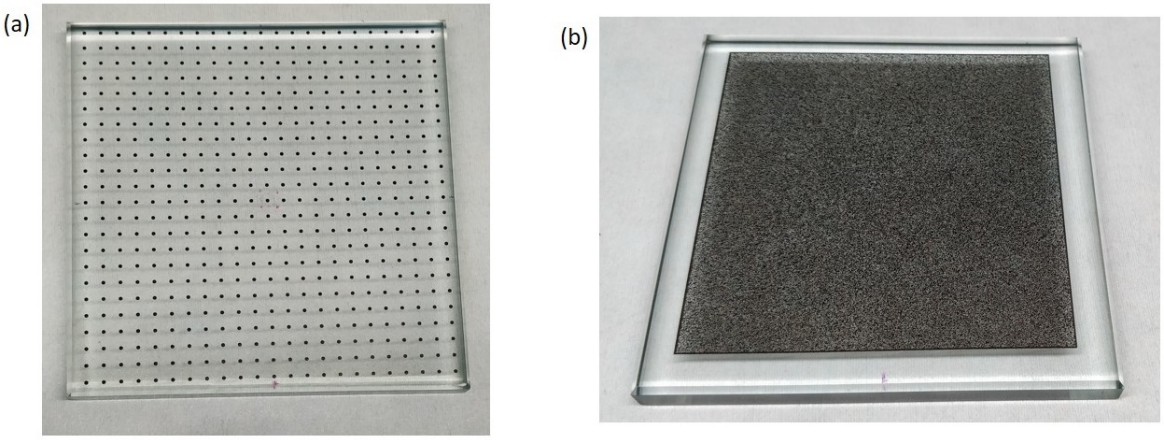

Figure C.3: (a) shows the calibration target. The target consists of 23 x 23 black dots forming a grid with each dot of 1 mm diameter and 5 mm spacing between any two adjacent dots. These are printed in black ink on a transparent glass plate of size 120 x 120 x 20 mm. (b) shows the random dot pattern. It has a specification of, dot density: 40 %, dot diameter: 0.2 mm and a minimum dot spacing in percentage of dot diameter: 3 %. The random dot pattern is printed on a 120 x 120 x 20 mm transparent glass plate. These are transparent dots with a black background printed around.

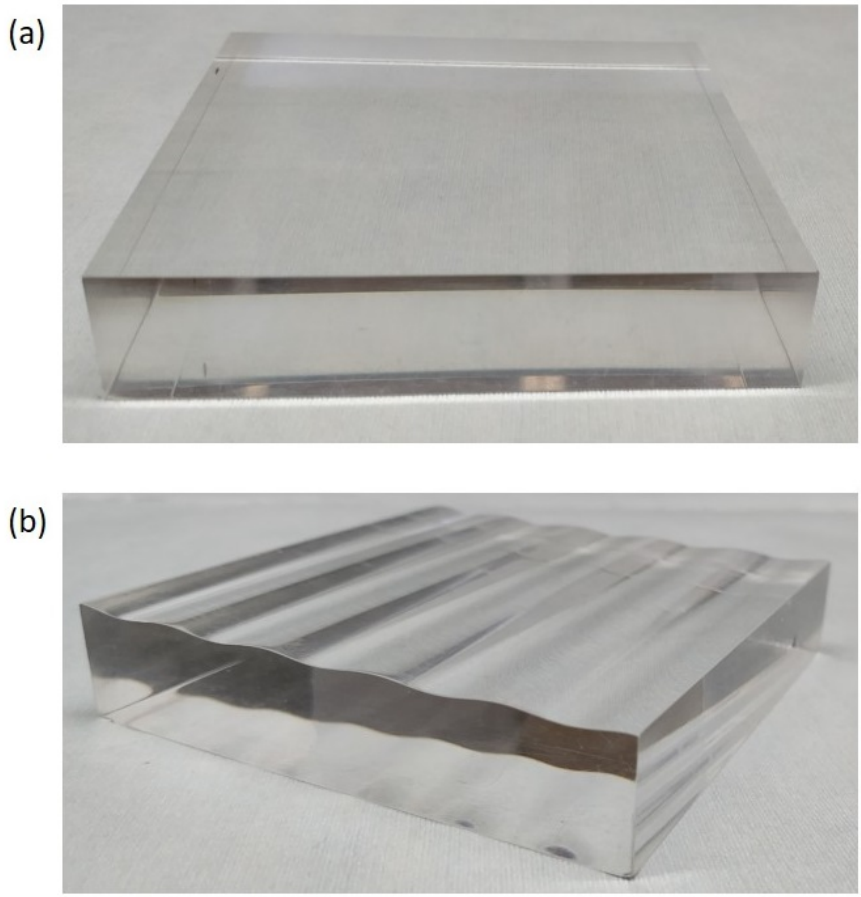

Figure C.4: (a) shows the flat interface Plexiglas profile used for the study experiments which has dimensions of 20 x 100 x 100 mm. (b) shows the wave interface Plexiglas profile used for the study experiments which has a block dimension of 20 x 100 x 100 mm. Around the mean height of 20 mm, a cosine wave profile is machined in one direction. The profile wave amplitude is 0.5 mm and the wavelength is 20 mm.

Figure C.5: (a) is an image of the convex lens interface used for the study experiments of focal length 300 mm. (b) is an image of the concave lens interface used for the study experiments of focal length 300 mm. The concave lens has a curvature only in one direction.

Bibliography

[1] R. L. R.P. Feynman and M. Sands, *The feynman lectures on physics.addison-wesley. volume i, chapter 51-4,* California Institute of Technology (1963).

[2] *Review of Maritime Transport 2017,* United Nations Conference on Trade and Development (UNCTAD) (2017).

[3] S. A. Makiharju, *The Dynamics of Ventilated Partial Cavities over a Wide Range of Reynolds Numbers and Quantitative 2D X-ray Densitometry for Multiphase Flow*, Ph.D. thesis, University of Michigan (2012).

[4] H. Schlichting, *Boundary Layer Theory* (Springer, 9th edn, 1979).

[5] O. Zverkhovskyi, *Ship Drag Reduction by Air Cavities*, Ph.D. thesis, TU Delft (2014).

[6] M. Callenaere, J.-P. Franc, J.-M. Mechel, and M. Riondet, *The cavitation instability induced by the development of a re-entrant jet,* Journal of Fluid Mechanics **444**, 223–256 (2001).

[7] K. V. Horoshenkov, A. Nichols, S. J. Tait, and G. A. Maximov, *The pattern of surface waves in a shallow free surface flow,* Journal of Geophysical Research: Earth Surface **118**, 1864 (2013).

[8] D. Mouaze, F. Murzyn, and J. Chaplin, *Free surface length scale estimation in hydraulic jumps,* Journal of Fluids Engineering-Transactions of the ASME (2005), 10.1115/1.2060736.

[9] J. E. Antonio-Lopez, J. J. Sanchez-Mondragon, P. LiKamWa, and D. A. May-Arrioja, *Fiber-optic sensor for liquid level measurement,* Opt. Lett. **36**, 3425 (2011).

[10] A. Felici, F. Di Felice, and F. J. A. Pereira, *Measurement of the cavitation pattern by two non-intrusive techniques: Laser imaging and ultrasound pulsed echography, Experiments in Fluids*, **54** (2013).

[11] B. Barshan and D. Baskent, *Comparison of two methods of surface profile extraction from multiple ultrasonic range measurements,* Measurement Science and Technology **11**, 833 (2000).

[12] A. B. Tayler, D. J. Holland, A. J. Sederman, and L. F. Gladden, *Exploring the origins of turbulence in multiphase flow using compressed sensing MRI,* Phys. Rev. Lett. **108**, 264505 (2012).

[13] R. F. Mudde, *Bubbles in a fluidized bed: A fast X-ray scanner,* AIChE Journal **57**, 2684 (2010), https://onlinelibrary.wiley.com/doi/pdf/10.1002/aic.12469 .

[14] R. Banasiak, R. Wajman, T. Jaworski, P. Fiderek, H. Fidos, J. Nowakowski, and D. Sankowski, *Study on two-phase flow regime visualization and identification using 3d electrical capacitance tomography and fuzzy-logic classification,* International Journal of Multiphase Flow **58**, 1 (2014).

[15] S. M. Kharlamov, V. V. Guzanov, A. V. Bobylev, S. V. Alekseenko, and D. M. Markovich, *The transition from two-dimensional to three-dimensional waves in falling liquid films: Wave patterns and transverse redistribution of local flow rates,* Physics of Fluids **27** (2015), 10.1063/1.4935958.

[16] E. A. Demekhin, E. N. Kalaidin, and A. S. Selin, *Three-dimensional localized coherent structures of surface turbulence. III. Experiment and model validation,* Physics of Fluids **22** (2010), 10.1063/1.3478839.

[17] C. E. Blenkinsopp, I. L. Turner, M. J. Allis, W. L. Peirson, and L. E. Garden, *Application of LiDAR technology for measurement of time-varying free-surface profiles in a laboratory wave flume,* Coastal Engineering **68**, 1 (2012).

[18] B. Jahne, J. Klinke, and S. Waas, *Imaging of short Ocean Wind-Waves - A critical theoretical review,* Journal of The Optical Society of America A-Optics Image Science and Vision (1994).

[19] C. COX, *Statistics of the sea surface derived from sun glitter,* J. Mar. Res. (1954).

[20] S. S. Gorthi and P. Rastogi, *Fringe projection techniques: Whither we are?* Optics and Lasers in Engineering (2010).

[21] A. Przadka, B. Cabane, V. Pagneux, A. Maurel, and P. Petitjeans, *Fourier transform profilometry for water waves: how to achieve clean water attenuation with diffusive reflection at the water surface?* Experiments in Fluids (2012).

[22] P. J. Cobelli, A. Maurel, V. Pagneux, and P. Petitjeans, *Global measurement of water waves by fourier transform profilometry,* Experiments in Fluids (2009).

[23] X. Zhang and C. S. Cox, *Measuring the two-dimensional structure of a wavy water surface optically: A surface gradient detector,* Experiments in Fluids (1994).

[24] C. S. COX, *Measurements of slopes of high-frequency wind waves,* J. Mar. Res. **16**, 199 (1958).

[25] D. Dabiri and M. Gharib, *Simultaneous free-surface deformation and near-surface velocity measurements,* Experiments in Fluids **30**, 381 (2001).

[26] G. Meier, *Computerized background-oriented schlieren,* Experiments in Fluids **33**, 181 (2002).

[27] S. B. Dalziel, G. O. Hughes, and B. R. Sutherland, *Whole-field density measurements by 'synthetic schlieren',* Experiments in Fluids **28**, 322 (2000).

[28] J. Kurata, K. T. V. Grattan, H. Uchiyama, and T. Tanaka, *Water surface measurement in a shallow channel using the transmitted image of a grating,* Review of Scientific Instruments **61**, 736 (1990).

[29] F. Moisy, M. Rabaud, and K. Salsac, *A synthetic schlieren method for the measurement of the topography of a liquid interface,* Experiments in Fluids **46**, 1021 (2009).

[30] G. Gomit, L. Chatellier, D. Calluaud, and L. David, *Free surface measurement by stereo-refraction,* Experiments in Fluids **54**, 1540 (2013).

[31] N. J. W. Morris, *Image-based Water Surface Reconstruction with Refractive Stereo*, Master's thesis, University of Toronto (2004).

[32] K. N. K. Nigel Morris, *Dynamic refraction stereo,* IEEE Transactions on Pattern Analysis and Machine Intelligence, VOL. 33, NO. 8 (2011).

[33] S. M. Soloff, R. J. Adrian, and Z.-C. Liu, *Distortion compensation for generalized stereoscopic particle image velocimetry,* Measurement Science and Technology **8**, 1441 (1997).

[34] R. Adrian and J. Westerweel, *Particle Image Velocimetry*, Cambridge Aerospace Series (Cambridge University Press, 2011).

[35] A. Prasad, *Stereoscopic particle image velocimetry, Experiments in Fluids 29(2), 103-116*, **29** (2000).

[36] A. Eddi, E. Fort, F. Moisy, and Y. Couder, *Unpredictable tunneling of a classical wave-particle association,* Phys. Rev. Lett. **102**, 240401 (2009).

[37] A. Eddi, E. Sultan, J. Moukhtar, E. Fort, M. Rossi, and Y. Couder, *Information stored in faraday waves: the origin of a path memory,* Journal of Fluid Mechanics **674**, 433–463 (2011).

[38] R. Dangla, F. Gallaire, and C. N. Baroud, *Microchannel deformations due to solvent-induced PDMS swelling,* Lab on a Chip **10**, 2972 (2010).

[39] A. Paquier, F. Moisy, and M. Rabaud, *Surface deformations and wave generation by wind blowing over a viscous liquid,* Physics of Fluids **27**, 122103 (2015).

[40] B. Valentine, *Photo taken by brian valentine posted on flickr.com,* https://www.flickr.com/photos/lordv/65835354/in/album-1571779/ (), accessed: 2018-11-08.

[41] B. Valentine, *Photo taken by brian valentine posted on flickr.com,* https://www.flickr.com/photos/lordv/416735827/in/album-1571779/ (), accessed: 2018-11-08.